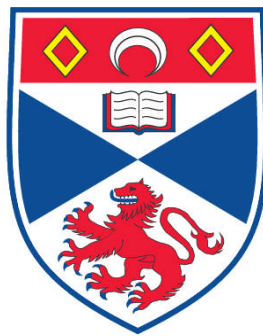# CONTINUOUS WAVE AND MODELOCKED FEMTOSECOND NOVEL BULK GLASS LASERS OPERATING AROUND 2000 NM

Flavio Fusari

A Thesis Submitted for the Degree of PhD
at the
University of St. Andrews

2011

Continuous wave and modelocked femtosecond novel bulk glass lasers operating around 2000 nm

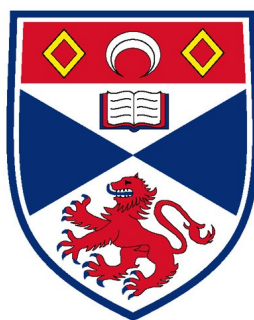*Thesis presented for the degree of*

Doctor of Philosophy

to the University of St Andrews

by

Flavio Fusari

October 2010

The J. F. Allen Physics Research Laboratories
School of Physics and Astronomy
University of St Andrews
North Haugh
St Andrews, KY16 9SS
Scotland

Declarations

I, Flavio Fusari, hereby certify that this thesis, which is approximately thirty-four thousand words in length, has been written by me, that it is the record of work carried out by me and that it has not been submitted in any previous application for a higher degree.

I was admitted as a research student in January 2007 and as a candidate for the degree of Doctor of Philosophy in January 2007; the higher study for which this is a record was carried out in the University of St Andrews between 2007 and 2010.

Date: **Signature of candidate:**

I hereby certify that the candidate has fulfilled the conditions of the Resolution and Regulations appropriate for the degree of Doctor of Philosophy in the University of St Andrews and that the candidate is qualified to submit this thesis in application for that degree.

Date: **Signature of supervisor:**

Copyright Declarations

In submitting this thesis to the University of St Andrews I understand that I am giving permission for it to be made available for use in accordance with the regulations of the University Library for the time being in force, subject to any copyright vested in the work not being affected thereby. I also understand that the title and the abstract will be published, and that a copy of the work may be made and supplied to any bona fide library or research worker, that my thesis will be electronically accessible for personal or research use unless exempt by award of an embargo as requested below, and that the library has the right to migrate my thesis into new electronic forms as required to ensure continued access to the thesis. I have obtained any third-party copyright permissions that may be required in order to allow such access and migration, or have requested the appropriate embargo below.

The following is an agreed request by candidate and supervisor regarding the electronic publication of this thesis:

Access to Printed copy and electronic publication of thesis through the University of St Andrews.

Date: **Signature of candidate:**

                                   Signature of supervisor:

Abstract

This thesis reports on the development of glass-based femtosecond laser sources around 2 µm wavelength. In order to be able to produce 2 µm radiation the dopants used were trivalent Thulium (Tm^{3+}) and trivalent Holmium (Ho^{3+}) that could be optically pumped with Ti:Sapphire radiation at 0.8 µm and semiconductor disk lasers (SDL) at 1.2 µm. The samples were produced at Leeds University and polished in house in bulk form and deployed in free space laser cavities.

Tellurite compounds doped with Tm^{3+} produced stable continuous wave 1.94 µm radiation when pumped at 800 nm with a maximum efficiency of 28.4% with respect to the absorbed power and maximum output power around 120 mW when pumped using a Ti:Sapphire operating around 0.8 µm. The radiation was broadly tunable across 130 nm. Tm^{3+}-Ho^{3+} doubly doped tellurite samples lased around 2.02 µm with maximum efficiency of 25.9% and with P_{OUT}=75 mW and a smooth tunability of 125 nm.

The fluorogermanate glass doped with Tm^{3+} gave an absorbed to output power efficiency of 50%. The maximum continuous wave output powers obtained were around 190 mW and limited by the available pump power at 0.8 µm. These results together with a very low threshold of 60 mW of incident power were comparable to the crystalline counterparts to this gain medium

The Tm^{3+} tellurite and the Tm^{3+}-Ho^{3+} tellurite compounds were also pumped by an SDL operating at 1215 nm to obtain an indication of the viability of such pump scheme. The results were a maximum internal slope efficiency of 22.4% with a highest output power of 60 mW. The comparison demonstrated that 1.2 µm pumping was competitive with using 0.8 µm wavelength.

The use of semiconductor saturable absorbing mirror (SESAM) technology was used for the modelocking of these lasers. The SESAM was produced in Canada and implanted with As^+ ions in order to reduce the relaxation time.

Trains of transform-limited laser pulses at 222 MHz as short as 410 fs centred at 1.99 µm were produced for the first time with a bulk Tm^{3+}:Fluorogermanate glass. The maximum average output power obtained was of 84 mW. The same SESAM deployed

on the Tm^{3+}-Ho^{3+} Tellurite compounds gave trains of transform-limited pulses as short as 630 fs at 2.01 µm with a repetition rate of 143 MHz and a maximum averaged output power of 43 mW. The regime of propagation obtained was soliton-like and the modelocking was self-starting. The results obtained with bulk glass were very promising and open interesting research pathways within the realm of amorphous bulk gain media.

Acknowledgments

May Vishnu bring the best for your life and your future endeavours. Super thanks go to everybody in the department, outside the department and in Chemistry that have made my PhD in St Andrews a truly unique journey!

A truck load worth of thanks also go to all my Italian friends in St Andrews! We organized, we laughed, we cried and we did it all together. The carrasau at Medda's, the kitchens at Bonaccorso's Restaurant, Annachiara's melanzane and Lucia's breasaola wraps… mouth watering! Thank you all! Un camion da cava pieno di ringraziamenti lo dono a tutte le persone che per me ci sono sempre state a Vicenza, che mi stanno vicino indipendentemente da dove sono e da cosa faccio insomma che mi vogliono bene. Grazie Romi, Mazzo, Fendi, Fabius!

On a completely different emotional level and at the roots of my being, my most grateful and sincere thanks goes to my family and Elena, your unconditional constant support and guidance has made me the person I am today. I could write a book of thanks for you but no words can describe how much I love you. Thank you Mom, Dad, Silvia. Thank you Elena for bearing me when I am nervous and for understanding me as none else does. Thank you as you understood the need I had to do this and because you came in beautiful Scotland so that we could stay close together. I love you scioppola colorata. Ad un livello emozionale completamente differente e alle radici del mio essere, i miei più sinceri ringraziamenti vanno alla mia famiglia e ad Elena, il vostro supporto costante e incondizionato e la vostra guida hanno fatto di me la persona che sono oggi. Potrei scrivere un libro di ringraziamenti per voi ma non ci sono parole che descrivono quanto vi ami. Grazie Mamma, Papà, Silvia, Elena. Grazie Elena per essere in grado di sopportarmi quando sono nervoso e per comprendermi come nessun altro fa. Grazie perché hai capito il bisogno che avevo di fare questa esperienza e perchè sei venuta in Scozia cosicchè potessimo stare vicini insieme. Ti Amo scioppola colorata.

This thesis closes yet another chapter of my life and I love being able to do it with this work, it sums up many long hours in the lab, many lows and many highs. It concentrates my love for science and discovery and my love for learning and self-improving. It stays with me and I hope I will be able to pass it onto others in the future. So as I like to repeat to the guys at the Cambridge Enterprisers in front of the coat of arms: What is the next challenge? Bring it on!

to Agnese, Bruno, Silvia, Elena

…goods and properties, qualifications and decorations are just accessories here placed so that we can cherish smiles and laughter, life is made of people and experiences and this is that lays within me. Thank you.

…beni e proprietà, titoli ed onorificenze sono solo accessori posizionati qui così che si possa gioire di sorrisi e risate, la vita è fatta di persone ed esperienze ed è questo che resta sempre dentro di me. Grazie.

Publication List

Regular journal contributions

1)   **F. Fusari**, A. A. Lagatsky, G. Jose, S.Calvez, A. Jha, M.D. Dawson, W. Sibbett, and C. T. A. Brown, "*Femtosecond mode-locked Tm^{3+} and Tm^{3+}-Ho^{3+} doped 2 µm bulk glass lasers*", Optics Express, **18**(21), 22090 (2010)

2)   **F. Fusari**, A. A. Lagatsky, B. Richards, A. Jha, W. Sibbett and C. T. A. Brown, "*Spectroscopic and lasing performance of Tm^{3+}-doped bulk TZN and TZNG tellurite glasses operating around 1.9 µm*", Optics Express, **16**(23), 19146 (2008)

3)   **F. Fusari**, S. Vetter, A. A. Lagatsky, B. Richards, S. Calvez, A. Jha, M. D. Dawson, W. Sibbett, and C. T. A. Brown , "*Tunable laser operation of a Tm^{3+}-doped tellurite glass laser near 2 µm pumped by a 1211 nm semiconductor disk laser*", Optical Materials, **32**(9), 1007-1010 (2010)

4)   **F. Fusari**, R. R. Thomson, G. Jose, F. M. Bain, A. A. Lagatsky, N. D. Psaila, A. K. Kar, A. Jha, W. Sibbett and C. T. A. Brown, "*Guiding characterization and 1.9 µm laser performances of ultrafast laser inscribed glass channel waveguides*", Submitted to Optics Letters (2010)

5)   A. A. Lagatsky, **F. Fusari**, S. Calvez, J. A. Gupta, V. E. Kisel, N. V. Kuleshov, C. T. A. Brown, M. D. Dawson, and W. Sibbett, "*Passive mode locking of a $Tm,Ho:KY(WO_4)_2$ laser around 2 µm*", Optics Letters, **34**(17), 2587 (2009)

6)   A.A. Lagatsky, **F. Fusari**, S.V. Kurilchik, V.E. Kisel, A.S. Yasukevich, N.V. Kuleshov, A.A. Pavlyuk, C.T.A. Brown, W. Sibbett, "*Optical spectroscopy and efficient continuous-wave operation near 2 µm for a Tm,Ho:KYW laser crystal*", Applied Physics B, **97** 321-326 (2009)

7) B. Richards, A. Jha, Y. Tsang, D. Binks, J. Lousteau, **F. Fusari**, A. Lagatsky, C. Brown and W. Sibbett, "*Tellurite glass lasers operating close to 2 μm*", Laser Physics Letters, 1–17 (2010)

8) X. Han, **F. Fusari**, M. D. Serrano, A. A. Lagatsky, J. M. Cano-Torres, C. T. A. Brown, C. Zaldo and W. Sibbett, "*Continuous-wave laser operation of Tm and Ho co-doped NaY(WO$_4$)$_2$ and NaLu(WO$_4$)$_2$ crystals*", Optics Express, **18**(6), 5413-5419 (2010)

9) A. A. Lagatsky, **F. Fusari**, S. Calvez, S. V. Kurilchik, V. E. Kisel, N. V. Kuleshov, M. D. Dawson, C. T. A. Brown, and W. Sibbett, "*Femtosecond pulse operation of a Tm,Ho-codoped crystalline laser near 2 μm*", Optics Letters, **35**(2), 172-174 (2010)

Invited conference contributions

10) **F. Fusari**, A. A. Lagatsky, Gin Jose, Xin Jiang, A. Jha, W. Sibbett and C. T. A. Brown, "*Laser operation of a bulk Tm^{3+}:Germanate glass laser around 2 μm with 50 % internal slope efficiency*", IEEE Photonics Society Annual Meeting 2009, Antalya Turkey, ThQ 1

11) **F. Fusari**, B. Richards, A. A. Lagatsky, S. Vetter, S. Calvez, M. Dawson, A. Jha, W. Sibbett and C. T. A. Brown, "*Spectroscopic and lasing performance of Tm-doped Tellurite and Germanate glasses operating around 1.9-μm wavelength*", LPHYS'09, ICFO Barcelona

12) A. Jha, X. Jiang, B.D.O. Richards, G. Jose, **F. Fusari**, A. A. Lagatsky, C.T.A. Brown, W. Sibbett, R. R. Thomson, N. S. Psaila, A. K. Kar, Q. Jiang, Z. Zhang, R. A. Hogg, S. Vetter, S. Calvez, M. D. Dawson "*Tm^{3+} and Ho^{3+} ions doped heavy metal oxide glasses for bulk fiber and waveguide lasers*", ISNOG 17th International Symposium on Non-Oxide and New Optical Glasses

13)   A. Jha, B.D.O. Richards, J. Lousteau, X. Jiang, Y. Tsang, **F. Fusari**, A.A. Lagatsky, D. Binks, C.T.A. Brown, and W. Sibbett, "*$Tm^{3+}/Ho^{3+}/Yb^{3+}$ co-doped Tellurite and Heavy-Metal Oxide Glass lasers*", LPHYS'09, ICFO Barcelona

Regular conference contributions

14)   **F. Fusari**, A.A Lagatsky, B. Richards, G. Jose, A. Jha, W. Sibbett and C.T.A. Brown, "*Spectroscopic and continuous wave laser properties of Tm^{3+} doped tellurite glasses around 2 µm*", EuroPhoton 2008 Paris, Paper WEoD.4

15)   **F. Fusari**, A. A. Lagatsky, Gin Jose, Xin Jiang, A. Jha, W. Sibbett and C. T. A. Brown, "*Continuous-wave laser operation of a bulk Tm:Germanate glass laser around 2 µm with 40 % internal slope efficiency*", MICS 2009, Trouville, Poster PO5

16)   **F. Fusari**, R. R. Thomson, G. Jose, F. M. Bain, A. A. Lagatsky, N. D. Psaila, A. K. Kar, A. Jha, W. Sibbett and C. T. A. Brown, "*Ultrafast Laser Inscribed Tm^{3+}:Germanate Glass Waveguide Laser at 1.9 µm*", Conference on Lasers and Electro-Optics (CLEO/QELS) San Jose, California 2010 paper: CTuU5

17)   S. Vetter, S. Calvez, M.D. Dawson, **F. Fusari**, A.A. Lagatsky, W. Sibbett, C.T.A. Brown, V.-M. Korpijärvi, M. Guina, B. Richards, G. Jose, A. Jha, "*1213nm Semiconductor Disk Laser pumping of a Tm^{3+}-doped tellurite glass laser*", LEOS Annual Meeting 2008, Paper 145828

18)   S. .Vetter, L. J. McKnight, S. Calvez, M. D. Dawson, **F. Fusari**, A. A. Lagatsky, W. Sibbett, C.T.A. Brown, V. M. Korpijärvi, M. Guina, B. Richards, G. Jose and A. Jha, "*GaInNAs semiconductor disk lasers as pump sources for Tm^{3+}(,Ho^{3+})-doped glass, crystal and fibre lasers*", SPIE Photonic West, 719317 (2009)

19)   A.A. Lagatsky, **F. Fusari**, C.T.A. Brown, W. Sibbett, S.V. Kurilchik, V.E. Kisel, A.S. Yasukevich, and N.V. Kuleshov, A.A. Pavlyuk, "*Efficient continuous-wave,*

2-μm Tm,Ho:KY(WO$_4$)$_2$ laser", Advanced Solid-State Photonics (ASSP) 2009 paper: WB7

20)   A.A. Lagatsky, **F. Fusari**, S.V. Kurilchik, V.E. Kisel, A.S. Yasukevich, A.A. Pavlyuk, C.T.A. Brown, N.V. Kuleshov, and W. Sibbett, "*Spectroscopy and efficient room-temperature laser operation of Tm,Ho:KY(WO$_4$)$_2$ around 2 μm*", The European Conference on Lasers and Electro-Optics (CLEO_E) 2009 paper: CA10_4

21)   A.A. Lagatsky, **F. Fusari**, C.T.A. Brown, W. Sibbett, S. Calvez, M.D. Dawson, J.A. Gupta, "*Passively mode-locked Tm,Ho:KY(WO$_4$)$_2$ laser around 2 μm*" The European Conference on Lasers and Electro-Optics (CLEO_E) 2009 paper: CA10_2

22)   A.A. Lagatsky, **F. Fusari**, C.T.A. Brown, and W. Sibbett, S. Calvez, M.D. Dawson, V.E. Kisel, S.V. Kurilchik, N.V. Kuleshov, J.A. Gupta, "*Femtosecond mode locking of a Tm,Ho:KYW laser near 2 μm*", Advanced Solid-State Photonics (ASSP) 2010 paper: ATuA1

Prizes and Awards

F. Fusari, IEEE Photonics Society 2009 *Best Student Paper Award, second prize recipient*, IEEE Photonics Society Annual Meeting 2009, Antalya, Turkey.
http://www.ieee.org/organizations/pubs/newsletters/leos/dec09/Best_Student_Paper_Award.html

List of Symbols and Acronyms

$\phi(\omega)$ Frequency-dependent phase change

$\phi(t,\omega)$ Phase spectrum

ϕ_{th} Fluence at threshold

$|E(t)|^2$ Square of electric field

A_0 Pulse amplitude

A_{eff} the laser mode cross sectional area

BRF   Birefringent filter

c   Speed of light in vacuum

CARS   Coherent anti-stokes Raman spectroscopy

CR   Cross relaxation

CW   Continuous wave

CWML   Continuous wave modelocking

d   Averaged path length

D   Total second order dispersion in the cavity

DBR   Distributed Bragg reflector

DOP   Dopants ions

d_{PI} Prism insertion length

DTA   Differential thermal analysis

d_{TTT} Tip-to-tip separation between prisms

$E(t,\omega)$ Electric field distribution

EM   Electromagnetic field

$E_M(t)$ Pulse envelope

EM	Energy migration
E_P	Pulse energy
ESA	Excited state absorption
ETU	Energy transfer upconversion
f_K	Focal length of the equivalent Kerr lens
FL	Füchtbauer-Ladenburg approach
FOM	Figure of merit
FWHM	Full width at half maximum
g	Saturated gain coefficient
GSA	Ground state absorption
GVD	Group velocity dispersion, second order dispersion
h	Planck constant
H	Enthalpy
HoLREP	Holmium laser prostate resection
$h\upsilon_P$	Energy of the pump photons
$\hbar\omega$	Phonon energy
IAC	Intensity autocorrelation
IOP	Institute of Photonics
k_B	Boltzmann constant
k_{In}	Thermal conductivity
KLM	Kerr lens modelocking
L	Length of the active element
LIDAR	Light detection and ranging
LS	Russel-Saunders coupling or LS coupling
n	Refractive index

$n(\lambda)$	Wavelength-dependent linear refractive index
n_0	Linear refractive index
n_2	Nonlinear refractive index
NA	Numerical aperture
NET	Nonresonant energy transfer
n_{TOT}	Total equivalent refractive index
NWF	Network forming ions
NWM	Network modifiers ions
OC	Output couplers
OCT	Optical coherence tomography
OPA	Optical parametric amplifiers
OPO	Optical parametric oscillators
P	induced dipole moment per unit volume
P_{ITH}	Incident power at threshold
P_M	Intracavity peak power
P_M	Peak power
P_M	Peak power of the incident radiation
QSML	Q-switched modelocking
RE	Rare Earths
ROC	Radius of curvature
SAM	Saturable absorber modelocking
SDL	Semiconductor Disk Laser
SESAM	Semiconductor saturable absorber modelocking
S_i	S Sellmeier coefficient
SPM	Self-phase modulation

T	Transmission of the output couplers
TBP	Time-bandwidth product
TEC	Thermo Electric Cooler
T_G	Temperature of glass transition
TmLREP	Thulium laser prostate resection
T_X	Melting temperature and Crystal Growth temperature
UC	Upconversion
VECSEL	Vertical-external-cavity surface-emitting lasers
$w(z)$	Spot size as a function of z
w_L	Beam waist radius of the laser
w_P	Beam waist radius of the pump
Z_L/Z_U	Ratio of the partition functions of the lower and upper manifolds
z_R	Rayleigh range
α	Constant relative to the pulse duration or the hyperbolic secant profile
β	Divergence of the beam
δ	Roundtrip scattering loss
δ_R	One-pass reabsorption losses in the laser element
$\Delta\lambda$	Optical bandwidth
ε_0	Dielectric permittivity
η	Slope efficiency
η_0	Maximum attainable slope efficiency
η_B	Mode matching efficiency
η_{CR}	Cross-relaxation efficiency
η_{ESA}	Excited state absorption efficiency
η_{NR}	Non-radiative transition efficiency

η_Q	Quantum efficiency or quantum yield
ϑ_2	Chirp rate
λ_i	λ Sellmeier coefficient
λ_L	Lasing wavelength
λ_P	Pump wavelength
λ_P/λ_L	Maximum theoretical efficiency, also called Stokes' limit
λ_{ZL}	Zero-phonon line
ρ_{KERR}	Kerr coefficient
σ_A	Absorption cross section
σ_E	Emission cross section
σ_G	Gain cross section
τ	$\text{Sech}^2(t)$ time constant
τ_F	Lifetime of the lasing level
τ_P	Pulse Duration
τ_R	Radiative time
υ_E	Abbe number
υ_{REP}	Repetition frequency
$\varphi(t)$	Time-dependent phase change
χ_1	Linear susceptibility
χ_n	n-order second rank dielectric susceptibility tensor of the medium
ω_0	Centre angular frequency

Table of Contents

Chapter 1

NIR solid-state femtosecond laser systems 1

Chapter 2

Chapter 3

Chapter 4

Chapter 5

Chapter 6

1. NIR SOLID-STATE FEMTOSECOND LASER SYSTEMS

1.1 Introduction

1.1.1 The 50th anniversary of laser radiation

The laser, as we find it in some of its applications nowadays, has undergone huge transformations and is now exploited in endless and ever growing sectors. Outstanding scientific and technological advances have been achieved over a very short time span since its first demonstration[1]: exactly 50 years ago in 2010. The anniversary has been greatly celebrated by all players of an industry that has massively grown over the last decades. Why has so much interest and development flourished around such discovery?

Since its very first demonstration[1] the light produced by a laser has showed its fundamental properties that makes it unique and particular: the highly monochromatic emission of continuous wave lasers, the spatial and temporal coherence and the capability to reach very high pulse energies and focused intensities. It is in the latter properties that the laser became an exceptional scientific tool, light-peak powers as high as giga Watts could be accessed for the first time revealing a whole family of non linear processes that had never been seen before.

Laser light owes its conception mainly to four great scientists: A. Einstein, who pre-

-dicted the likelihood of the stimulated emission of radiation 1917[2], A.L. Shawlow and C.H.Townes who described its working principles in 1958[3] and Theodore Maiman in 1960[1] who showed that the mechanisms behind microwave oscillators could be applied to light oscillators. In the sixties the maser, Microwave Amplification by Stimulated Emission of Radiation, was the scientific mainstream. The journal Physical Review Letters was overwhelmed by paper submissions relating to the maser and rejected T. Maiman's work on the first operational laser as it was deemed too similar to one of his previous works. His work was finally published in Nature Journal. While the ruby as an active material was widely used in microwave amplifiers Maiman's clever step was to excite the material via a flash lamp thus achieving the population inversion. The first solid-state flashlamp-pumped laser ever was created.

The laser began a revolution in applied and quantum physics. Its applications nowadays are countless, they span from simple ones like the laser pointer, to the more exotic ones like plasma confinement and cooling to temperatures of few nK in the creation of the Bose-Einstein condensate[4]. From our perspective, before delving into the motivations that underpin this work, it is interesting to introduce another very important discovery that made the laser radiation so useful and unique: ultrafast pulse generation.

1.1.2 Femtosecond pulses: applications

Pulsed laser systems have been studied since the inception of the laser and Q-switching is routinely used nowadays to produce extremely high energy pulses. Q-switched systems usually produce pulses on a nanosecond scale duration which, in nature, is still a relatively long time compared for instance with chemical reactions that happen on a femtosecond scale. Generation of femtosecond (fs) pulse durations has been established over the last few decades in research labs and industrial settings and its applications are today countless.

The unique properties of fs-light pulses are exploited in chemistry for the monitoring of chemical reactions. The use of fs lasers has resulted in the award of the Nobel prize for Chemistry to A. Zewail in 1999[5]. Indeed, a whole new branch of Chemistry has been born: *femtochemistry,* where real-time probing of chemical reactions could be achieved[6].

After the discovery of the optical fibers the use of lasers for optical communications became paramount and today's internet network is relying on multi GHz repetition rate systems to support the Tbit/sec speed required[7]. Ultrafast laser pulses are used in photonic switches[8], high-speed AD converters[9-10] and in the measurements of the relaxation processes of excitons carriers in semiconductors[11]. The high intensities that can be reached by the pulses are exploited in micro-machining[12]. In medicine the use of ultrafast laser systems has grown across disparate branches and they all take advantage of the *cold ablation* effect. For fs systems, as it will be demonstrated in chapter 5, while average powers are quite low, peak powers reach the kW or the MW range allowing the instantaneous sublimation of the molecules without depositing much heat in the tissue[13]. Examples of medical techniques are the LASIK that can be used to correct sight defects[14] and successful brain tumour removal[15]. The selective killing of viruses with a fs system in infected cells has also been demonstrated[16]. In medical imaging femtosecond systems can be used in Optical Coherence Tomography (OCT) systems[17] and coherent anti-stokes Raman spectroscopy (CARS) that allows label-free tissue analysis[18]. Furthermore, the forefront of today's advanced laser research has expanded to the study of *attosecond* pulses which are nine orders of magnitude shorter than those from typical Q-switched systems[19].

In this research project we focus on the production of femtosecond pulses at wavelengths around 2µm with amorphous bulk glasses. In section 1.2, the motivations underpinning the work carried out in this project are presented while in section 1.3 and 1.4 the basics of ultrafast systems and propagation are covered.

1.2 Motivation

1.2.1 Solid-state amorphous dielectric gain media

This project is based on the development of solid-state amorphous gain media lasers, they are typically based on two components: the host matrix and a small concentration of active impurities called *dopants*. Adapting the host composition and impurity type and concentrations allow a wide variation of the lasing characteristics, as the atomic transitions and lifetimes of the dopant energies states can be carefully tailored. Research in this field has led to the discovery of hundreds of different hosts and dopants among

countless crystals[20], some of which have been successfully transferred to industrial or medical applications. Large research and development efforts are nowadays channelled on solid-state laser systems as they need relatively little engineering from laboratories to market compared to other systems. They can reach ultra-intense pulse energies in bulk crystalline media and produce kW continuous wave high power systems in fiber lasers[21].

The laser systems demonstrated during the course of this thesis were based on glasses. Glasses belong to the family of materials that lack long range ordered periodic structure, *amorphous materials*, as will be explained in-depth in chapter 2. There are many amorphous materials which are used for light generation and some examples are: colloidal solutions of nanocrystals and polymers[22], glasses[23], and glass-ceramics[24]. The key advantages of amorphous materials that make them highly suitable for a broad range of applications are countless and an incomplete list is reported here. They can be made inexpensively with almost perfect optical quality, they can be easily shaped in any form and dimension and easily fabricated with a well established industrial technology. Furthermore they can scale to high energy applications and have relatively low development costs. The fact that they can be shaped in any form is a unique property of the amorphous materials, so for example glasses can be used in both bulk and fiber forms as they can be drawn with relative ease. Another advantage is their broad and smooth emission spectra, compared to the crystalline counterparts, for their inherent inhomogeneous broadening mechanism, as will be explained in detail in chapter 2.

1.2.2 The applications for CW and ultrafast pulsed systems at 2 µm

The development of 2 µm solid state laser systems is of great interest nowadays for a wide range of applications and in this respect many authors have recently published interesting reviews, for example I. Sorokina[25], B. M. Walsh[26], and A. Godard[27]. Owing to the high absorption of H_2O molecule in the 2 µm band, continuous wave lasers define some of the cutting edge surgery applications in neuroendoscopy[28], brain surgery[29] and urology[30] where the Thulium and Holmium laser prostate resection (TmLREP) and (HoLREP) are becoming surgery standards[31]. Atmospheric LIDAR[32] and pollutant probing exploit the resonance bands of NO_2 and CO_2

molecules over the 2 μm region[33]. LIDAR setup sources comprise mid-infrared optical parametric oscillators (OPO) and optical parametric amplifiers (OPA) and they are efficiently pumped with quasi-CW high energy 2 μm lasers[23]. Solid state high power sources at 2 μm have been successfully proven in several gain media, bulk crystals and fibers[27], in bulk ZBLAN glass[23], in semiconductor disk lasers[34] and in micro-sphere lasers[35].

The generation of ultrafast lasers around the 2 μm region is of course interesting for time-resolved spectroscopy and the nonlinear frequency upconversion to the mid and far-IR spectral regions[36]. The molecular fingerprint region from 2 to 5 µm can be accessed with supercontinuum generation[37] and the broad emission bands of ultrafast pulses. Ultrafast 2 µm lasers can be used for micromachining of semiconductor and transparent materials[38] when the common sources cannot be used. There are earlier demonstrations of femtosecond laser sources at 2 µm but they had low average output powers in the orders of few mW[39]. Remarkably, the record to date is 108 fs pulses at 1980 nm with an average power of 3.1 W but they were produced with a quite complex systems of amplification of Raman-shifted Er-doped fiber laser radiation in a Tm-doped fiber[40]. The need of compact and reliable systems for ultrafast pulses generation at around 2 µm is very high and Tm^{3+}-doped and Tm^{3+}-Ho^{3+}-doped amorphous media offer very interesting possibilities. In chapter 5 the generation of 410 fs pulses with an average output power of 84 mW by a bulk glass based laser is reported, but before then in the next section, some of the fundamental concepts that underpin ultrafast laser pulse generation are briefly explained.

1.3 Basics of ultrafast pulsed systems

1.3.1 Definitions

Ultrafast pulsed lasers are lasers that generate single or trains of coherent light with pulse durations in the range of *picoseconds (10^{-12}s) to attoseconds (10^{-18}s)*, these physical events are extremely short and in order to give an idea of how short these pulses are, let us compare a femtosecond with a measurement of distance. If we set one femtosecond equivalent to a meter then one second worth of femtoseconds is equivalent to 25 million around-the-world trips! The main parameters that characterise ultrafast

laser pulses can be listed as follows: duration, shape, energy, peak power, repetition rate, centre wavelength and bandwidth. Such properties are linked to each other so that the improvement of one could worsen another, and a compromise has to be found to guarantee sustainable generation. The electric field of a pulse can be mathematically described in space and time by the following notation[41-42]:

$$E(t) = \Re\{E_M(t)\exp[i(\omega_0 t + \varphi(t))]\} \tag{1.1}$$

Where $E_M(t)$ is the pulse's envelope, $\varphi(t)$ is a time-dependent phase change, and ω_0 the centre angular frequency. The pulse envelope $E_M(t)$ that can be generated in pulsed laser system are usually characterised as either the Gaussian profile $E_0\exp(-\alpha t^2)$, with α being the constant relative to the pulse duration, or the hyperbolic secant profile $E_0\mathrm{sech}(t/\tau_P)$ where τ_P is the pulse duration. If we take $\varphi(t)=\vartheta_2 t^2$ which corresponds to a linear variation of the phase the Gaussian pulse the temporal description (1.1) becomes:

$$E_G(t) = \Re\{E_0 \exp(-\alpha t^2)\exp[i(\omega_0 t + \vartheta_2 t^2)]\} \tag{1.2}$$

Formula (1.2) describes the temporal evolution of the pulse and its Fourier transform is:

$$E_G(\omega) \cong \Re\left\{E_0 \exp\left(-\frac{\alpha/4}{\alpha^2+\vartheta_2^2}(\omega-\omega_0)^2\right)\exp\left(-i\frac{\vartheta_2/4}{\alpha^2+\vartheta_2^2}(\omega-\omega_0)^2\right)\right\} \tag{1.3}$$

If we then calculate the full width at half maximum, FWHM of the pulse in the time domain and the FWHM of its transformed version in the frequency domain we obtain:

$$\Delta t_{FWHM} = \left(\frac{2\ln 2}{\alpha}\right)^{1/2} \tag{1.4}$$

$$\Delta v_{FWHM} = \frac{1}{\pi}\left(\frac{2\ln 2}{\alpha}(\alpha^2+\vartheta_2^2)\right)^{1/2} \tag{1.5}$$

The product of these two quantities is called *time bandwidth product*, TBP. It is defined by the bandwidth theorem and it sets the ultimate lower limit for the pulse duration given the spectrum of the pulse. In our case, for a Gaussian (G) and a hyperbolic secant (hs) pulses, the time bandwidth product can be written:

$$TBP = \Delta t_{FWHM} \Delta \nu_{FWHM} = \frac{2\ln 2}{\pi}\left(1+\left(\frac{\vartheta_2}{\alpha}\right)^2\right)^{1/2} \tag{1.6}$$

$$\Delta t_G \Delta \nu_G = 0.441 \tag{1.7}$$

$$\Delta t_{HS} \Delta \nu_{HS} = 0.315 \tag{1.8}$$

The presence of periodic instabilities in the time domain, due to Q-switching effects, or *chirping* of the pulses can generate spectral features that ultimately act to degenerate the quality of the pulses produced and increase the TBP value.

1.3.2 Linear pulse propagation in dielectric media

The study of pulse propagation and the effect of such pulses on transparent media is an extremely important issue in ultrafast laser physics. The propagation of the pulse, as for any other kind of EM field, through a dielectric medium induces a polarization of the medium and the following formula holds[43] for the induced dipole moment per unit volume, **P**:

$$\mathbf{P} = \varepsilon_0\boldsymbol{\chi}_1 \cdot \mathbf{E} + \varepsilon_0\boldsymbol{\chi}_2 \cdot \mathbf{E} \cdot \mathbf{E} + \varepsilon_0\boldsymbol{\chi}_3 \cdot \mathbf{E} \cdot \mathbf{E} \cdot \mathbf{E} + ... \tag{1.9}$$

Where $\boldsymbol{\chi}_n$ is the n-order second rank dielectric susceptibility tensor of the medium and ε_0 the dielectric permittivity. Depending on the strength of the EM field the polarization is affected in different ways. The linear susceptibility $\boldsymbol{\chi}_1$ is the one that usually plays the major role and is connected to well known effects like, angular dispersion, phase dispersion, interference, absorption and birefringence. Higher-order susceptibilities can only be accessed by very intense EM fields, such as those within an ultrafast light pulse, and cause the non-linear effects explored briefly in section 1.3.3.

The light pulse traversing the gain medium is, in general, made up of electric fields at different frequencies. In chapter 2 it is shown that the refractive index depends on the wavelength and therefore the pulse's spectral components encounter different refractive indexes depending on their respective frequency. This, in turn, causes different light components to travel at different speeds in the medium and the phase of such light fields, $\phi(\omega)$ becomes frequency dependent[44]:

$$\phi(\omega) = \frac{\omega L}{c} n(\omega) = \frac{2\pi L}{\lambda} n(\lambda) \qquad (1.10)$$

where L is the length of the material transversed by the EM wave in normal incidence and c the speed of light in vacuum. The mathematical empirical relation that connects the refractive index, n(λ), with the wavelength was proposed by Sellmeier[45]:

$$n^2(\lambda) - 1 = \sum_{i \in N} \frac{S_i \lambda^2}{\lambda^2 - \lambda_i} \qquad (1.11)$$

Where i=1,2,3 and the coefficients S_i and λ_i are called the Sellmeier coefficients. These coefficients are empirically derived and provided in tables for the different materials, or fitted from the refractive index measured at different wavelengths as is shown in chapter 2. In order to highlight the various terms in $\frac{\partial \phi(\omega)}{\partial \omega}$ that are relevant for the propagation of the pulse it is useful to locally express equation (1.10) with (1.11) as a Taylor series calculated around the frequency of interest ω_0:

$$\frac{\partial \phi(\omega)}{\partial \omega} = \phi(\omega_0) + \frac{\partial \phi(\omega_0)}{\partial \omega} \frac{(\omega - \omega_0)}{1!} + \frac{\partial^2 \phi(\omega_0)}{\partial \omega^2} \frac{(\omega - \omega_0)^2}{2!} + \frac{\partial^3 \phi(\omega_0)}{\partial \omega^3} \frac{(\omega - \omega_0)^3}{3!} + k \quad (1.12)$$

where k accounts for higher order terms. The first four terms of the Taylor expansion can be associated with particular physical effects and are reported in table 1.1:

Term in frequency domain	Related to	Effect on the pulse	Term in time domain
$\phi(\omega_0)$	Phase velocity $v_g = L(\omega_0/\vartheta_0)$	Brings an absolute delay	$\phi(t) = \vartheta_0$
$\frac{\partial \phi(\omega_0)}{\partial \omega}$	Group velocity $v_g = L(\partial \omega/\partial \phi)$	Brings a group delay	$\phi(t) = \vartheta_1 t$
$\frac{\partial^2 \phi(\omega_0)}{\partial \omega^2}$	GVD, 2nd order dispersion, group velocity dispersion	Brings a linear variation on the phase of different frequencies (linear chirp)	$\phi(t) = \vartheta_2 t^2$ (1.2) is the formula of a linearly chirped pulse
$\frac{\partial^3 \phi(\omega_0)}{\partial \omega^3}$	TOD, third order dispersion	Brings a quadratic chirp	$\phi(t) = \vartheta_3 t^3$

Tab 1.1 The various dispersive effects on the phase of the pulse's components when it transverses the active material. The first column is the representation in frequency and the final column is an equivalent representation in time.

Table 1.1 above highlights the different dispersive effects brought about by the linear susceptibility tensor in a dielectric media. The *group velocity dispersion (GVD)* acts to spread the leading edge or the trailing edge of the pulse depending on its sign. For instance, equation (1.2) describes, in the time domain, a Gaussian linearly chirped pulse affected by positive GVD. In fig 1.1 two pulses affected by positive and negative chirp are shown. Equation (1.6) clearly links the increase of TBP of a chirped pulse to the chirp rate ϑ_2.
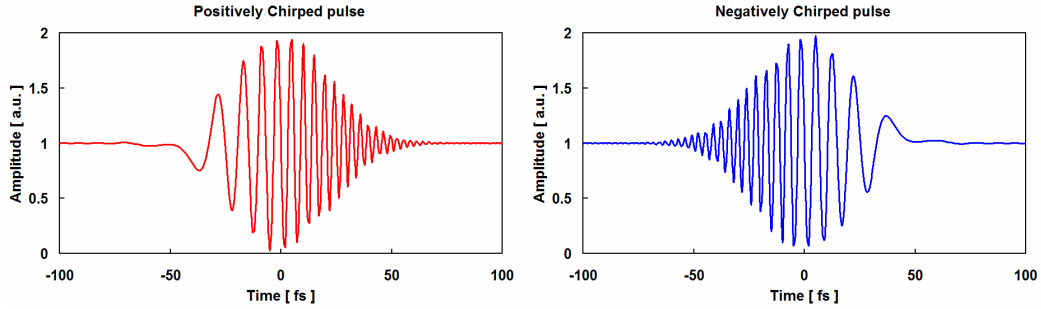
Fig 1.1 The two examples of the intensity envelopes of positive chirped and negative chirped pulses on the left and on the right hand sides of the picture.

Several techniques to actively control and compensate for GVD in the laser system are in use and these include diffraction grating compressors, chirped Bragg stack mirrors and Gires Tournois interferometers. However the technique that has settled over the years to be the most used in experimental setups is the combined use of two prisms pairs[31], because of their low cost, simple deployment, high flexibility and low scattering losses. This compensation technique was used throughout the course of this PhD and it is therefore briefly presented here.

The technique exploits the angular dispersion of a pair of prisms to provide wavelength path separation:
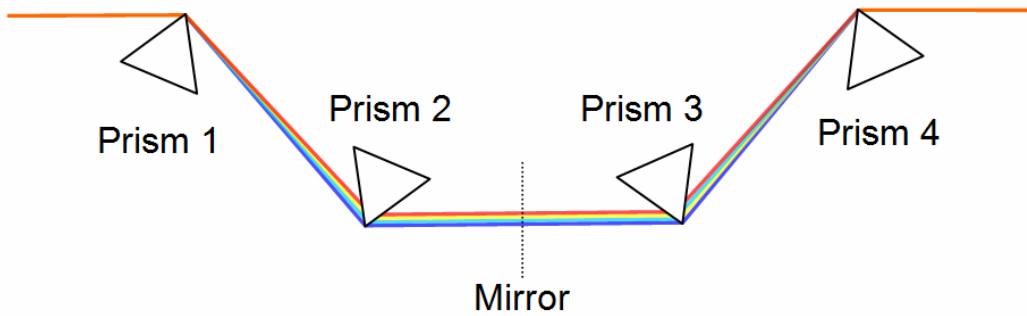
Fig 1.2 The prism pair technique as used to compensate for second order dispersion in the laser cavities. The picture shows the double pass path and the position of the mirror of the laser cavity.

In this way, longer wavelengths will have shorter paths through the system and reduced passing time, thus compensating positively chirped pulses as shown in Fig 1.2. The prisms are inserted at their minimum deviation angle and are designed for such angle to be Brewster's angle for the prisms material ensuring near-to-zero insertion losses. There are two pairs of prisms in Fig 1.2, but in actual laser system one single pair is often used within the cavity so to exploit the double pass offered by the mirror at the end of the resonator, represented by the dashed line. For a particular distance between prisms 1 and 2 a certain amount of negative GVD can be generated. The GVD of the prisms series can be calculated as[46]:

$$GVD = \left(\frac{\lambda}{cd}\right)\frac{\partial^2}{\partial\lambda^2}\left\{4d_{TTT}\left\{\left[\frac{\partial^2 n}{\partial\lambda^2}+\left(2n-\frac{1}{n^3}\right)\left(\frac{\partial n}{\partial\lambda}\right)^2\right]\sin(\beta)-2\left(\frac{\partial n}{\partial\lambda}\right)^2\cos(\beta)\right\}\right\} \quad (1.13)$$

Where d is the averaged path length, n the refractive index of the material used in the prisms, β the divergence of the beam at the prisms exit, and d_{TTT} the tip-to-tip separation between prisms 1 and 2. This formula has been extensively used in the designing of the laser cavities of chapter 5.

1.3.3 Nonlinear pulse propagation in dielectric media: the Kerr effect

The high intensity of the laser pulses can provide access to the higher order non-linear susceptibility terms of equation (1.9). Under high intensity fields a plethora of non-linear effects can be observed including second and third harmonic generation, frequency mixing, sum and difference frequency generation, and Raman effects. In our laser systems the prevalent nonlinear effects experienced are *self-focusing* and *self-phase modulation (SPM)*. Both effects are fundamental in the generation of ultrashort pulses[47] and are due to the *optical Kerr effect*.

In a dielectric medium the changes in refractive index are linked to **χ₃** and the EM field by equation[48]:

$$n_{TOT} = n_0 + \frac{3\chi_3}{8n_0}|E(t)|^2 \quad (1.14)$$

Where n_{TOT} is the total equivalent refractive index and n_0 is the linear refractive index. As the light intensity is proportional to $|E(t)|^2$ it can be seen that changes of the total re-

-fractive index can take place for large enough intensities. The quantity:

$$n_2 = \frac{3\chi_3}{8n_0}$$

(1.15)

is known as the *nonlinear refractive index*, and is usually quoted in cm^2/W. This allows us to write $n = n_0 + n_2 I$ that shows that n_2 is an *intensity dependent refractive index*.

The *self-focusing* phenomenon[41] can be compared to the effect of a graded index lens. The laser beam transversing the gain medium has a Gaussian intensity profile cross section and will have higher intensities at the core of the beam. The Kerr effect will be stronger in such volume and the total refractive index n_{TOT} in the medium will gradually decrease from the maximum at the centre creating an instantaneous graded index lens leading to the focusing of the beam. The effect can be quantified and f_K is the focal length of the equivalent Kerr lens for Gaussian pulses when considering only the phase changes near the beam axis in a parabolic approximation[49]:

$$f_k = \frac{\pi \cdot w_L{}^4}{4n_2 \cdot L \cdot P_M}$$

(1.16)

Where L is the length of the Kerr medium and P_M the peak power of the incident radiation. This effect can be detrimental in laser rods causing focused intensities sufficient to overcome the damage threshold of the medium, but can also be used in modelocking[50] as will be explained in the next section.

Self-phase modulation[41] is a temporal effect in comparison with the geometric nature of the self-focusing. While the pulses traverse the medium the instantaneous total refractive index n_{TOT} will increase with the leading edge of the pulse, slowing the EM field. Conversely n_{TOT} will decrease with the trailing edge thus accelerating the EM field. The total action will result in a self-chirping of the pulse that can act as a compressing mechanism thus counteracting the pulses' dispersion but also as a mechanism to expand the range of frequencies available in the pulse. The SPM is a parameter which strength is dictated, once again, by the strength of the Kerr effect and therefore is also material dependent.

1.3.4 Quasi-soliton propagation: the Haus model

In some cases the SPM can balance the dispersive effects in the cavity therefore *shaping* a transform limited pulse which propagates in the cavity as a fundamental *soliton*[51]. The theory of such propagation, which involves the nonlinear Schrödinger equation, is not explored in this report, but the effect is found in our laser system and causes *soliton-like* propagation as described by Haus[47]. The pulses are continuously shaped by the SPM and the GVD but they always obey the *Area theorem*[47]:

$$|A_0|\tau = \sqrt{\frac{2|D|}{\rho_{KERR}}} \tag{1.17}$$

Where A_0 is the pulse's amplitude, τ is the $sech^2(t)$ time constant, D the total cavity GVD and ρ_{KERR} a so-called Kerr coefficient. If we recall that the energy of the pulses is $E_P = 2A_0^2\tau_P$ then from (1.17) we can write:

$$\tau_P = 1.7627 \frac{4|D|}{\rho_{KERR}} \cdot \frac{1}{E_P} \tag{1.18}$$

Where 1.7627 converts τ from its FWHM value. Under this propagation mode the pulse duration is inversely proportional to their energy by a factor dependent on the dispersion and ρ_{KERR}. By measuring the pulse duration at different intracavity powers, the value of ρ_{KERR} can be found. A useful formula for ρ_{KERR} is[47]:

$$\rho_{KERR} = \frac{2\pi}{\lambda_L} n_2 \frac{2 \cdot L}{A_{eff}} \tag{1.19}$$

Where λ is the lasing wavelength, L the length of the active element and A_{eff} the laser mode cross sectional area. Once ρ_{KERR} is known it is easy to estimate the nonlinear refractive index:

$$n_2 = \frac{\rho_{KERR} \cdot \lambda_L \cdot w_L^2}{4 \cdot L} \tag{1.20}$$

Such propagation mode is verified in our experiments and (1.20) is used in sections 5.3 and 5.4 to calculate the value of the nonlinear refractive index n_2.

1.4 Generation and measurement of ultrafast laser pulses

1.4.1 Modelocking principles

Femtosecond laser pulses are extremely short events and their generation has posed significant challenges for many years. The use of saturable absorbers was excluded, at first, as it was thought that their recovery time was physically limited[52]. Another technique called *modelocking* was postulated in the 1970s[53] and it was demonstrated in 1991 that *Kerr lens modelocking* was one of the simplest way of generating fs pulses[50]. The advent of semiconductor technology has allowed the engineering of saturable absorbers with highly customised characteristics that has enabled their use as initiation and stabilisation technique for the modelocking as is presented in chapter 5.

The term *modelocking* describes an effect that is at the heart of ultrafast laser pulse generation. As is well-known, in a standing wave laser cavity many longitudinal modes are able to propagate within the cavity, their frequency separation $\Delta\upsilon$ is dependent on the length of the cavity L : $\Delta\upsilon = c/2L$. The modes that will successfully propagate will, of course, be the ones that have positive net gain. Let us say, for instance, that in the cavity 20 longitudinal modes propagate, they will have generic phases and the laser radiation will have an averaged noisy CW emission. If the phase relationship of such modes is somehow locked they will interfere to each other as shown in figure 1.3.
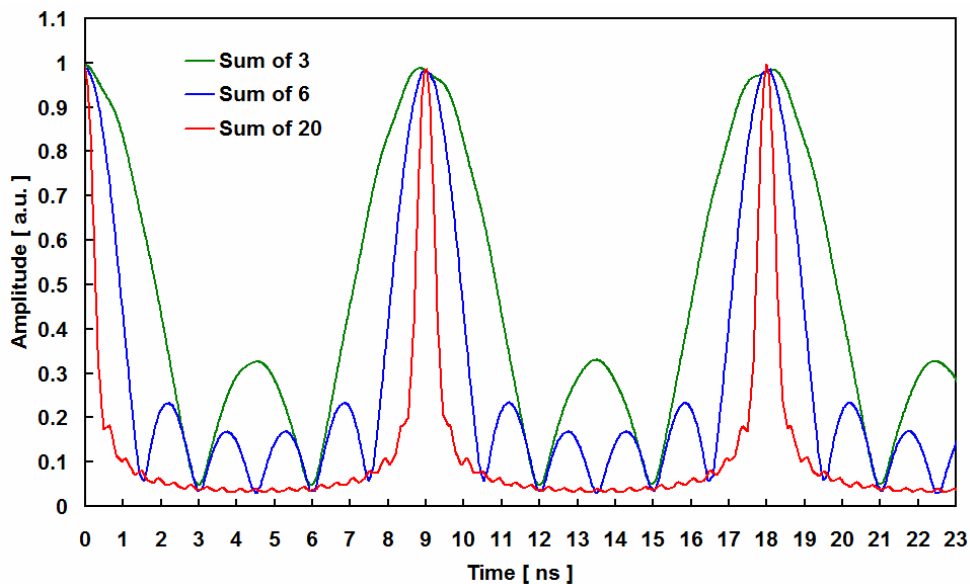

Fig 1.3 The superposition of 3, 6, and 20 longitudinal propagation modes locked in phase within the laser cavity. The resulting envelope is a pulse which duration depends on the number of locked mode. The graph has been normalised to the peak's maximum.

The interference is constructive with a period that is equal to the roundtrip cavity flight time, where the modes have fixed phase relations and a single pulse is produced. The whole of the radiation in the cavity is then temporally and spatially concentrated in the pulse. This, of course, places technology limits on the elements of the cavity which have to withstand extremely high powers. The number of modes that are locked in phase at a given time depends on a broad range of factors but especially on the gain bandwidth of the active material that has to support their propagation. It was therefore very useful to work with glass compounds where the emission tends to be smooth and broad.

1.4.2 Modelocking techniques

In the previous section it was shown that laser pulses can be generated by imposing a fixed phase relationship among the longitudinal propagation modes of the laser system. In order to generate and maintain such phase relationships, the laser cavity must contain a mechanism that favours the propagation of a single high-intensity pulse per roundtrip, namely, the single pulse experiences lowest losses. In this case, the longitudinal modes will naturally tend to lock their respective phases and produce a single pulse. Modelocking is thus a resonant effect and producing a slight modulation of the intracavity power timed with the cavity round trip time introduces a low-loss time slot that favours radiation propagating in this fashion. This modulation can be actively or passively obtained. *Active modelocking* with the use of acousto-optic modulators and other systems produces a very reliable train of pulses that can be easily synchronised with external systems. *Passive modelocking*, exploiting the Kerr effect in the *Kerr lens modelocking*, KLM or a saturable absorption in the *saturable absorber modelocking*, SAM are techniques capable of achieving much shorter pulses.

   Kerr lens modelocking was first demonstrated by Spence et al.[50], it exploits the self-focusing arising from the optical Kerr effect. Due to the high intensity present, the train of ultrafast pulses in the laser cavity experience a shorter focal length Kerr lens and cause the laser mode to propagate in the cavity with slightly smaller beam waists. KLM can be considered a fast type of saturable absorption, under the classification of Fig 1.4 below, as the polarization of the gain material is almost instantaneous. This allows the generation of very short pulses of the order of few optical EM cycles but lacks of a self-starting mechanism. There are in fact many orders of magnitude between

the noise background of the CW emission and the peaks normally found in the very short pulses. Building those pulses from the noise background can be very difficult indeed. In order to facilitate the starting of the KLM some cavities were tried in our glass systems with the aid of the Magni-Cerullo plots[54-55], but no appreciable pulsing behaviours could be observed.

Saturable absorber modelocking is based on a *saturable absorber*, SA, which is a device that exhibits absorbance dependent on intensity. In our case, the absorbance decreases with increasing intensity before eventually saturating. In this way, an intensity dependent component is inserted into the cavity and provides an amplitude modulation, where the loss decreases with increasing input intensity. A very important parameter of any SA is the recovery time, which is the time needed for the system regain its absorbance following the propagation of a pulse. In figure 1.4 the well known gain-loss time dynamics that describe the pulse formation in our glass based systems[51] are shown. The loss and gain curves are relative to slight perturbations of average values while the pulses are plotted in full swing from zero emission to maximum emission. The intensity envelopes of the pulses are all $\text{sech}^2(t)$ as they represent the steady state solution of the Haus master equation[47] in presence of dispersion and Kerr effect.
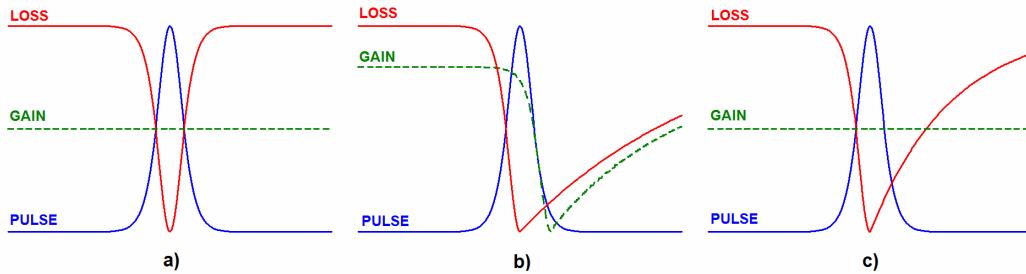
Fig 1.4 The time dynamics of gain, losses and pulse formation in the presence of a a) fast SA, b) slow SA c) slow SA and soliton formation.

In the case of fig 1.4a the saturable absorption recovery time is in the order of magnitude of the pulse duration and it is therefore termed *fast* and in such cases the gain is not perturbed. In case 1.4b the saturable absorber is *slow* under the same definition but the interplay with gain saturation creates a window in time where the pulse can successfully be generated. This is mostly the case of dye lasers and is not relevant to our solid state systems. In case 1.4c the net gain window closes in time slower than in the *fast* case, the pulse formation is entirely shaped by the interplay of SPM and dispersion

effects and the slow absorber acts as stabiliser operating in the so-called *solitonic regime*[51].

1.4.3 Continuous wave and Q-switching modelocking regimes

The SAM modelocking concept dates back to the early years of the laser[56] and its use is often in combination with the end mirror of a laser cavity which provide the substrate. Different substrate combinations have different acronyms for example A-FPSA antiresonant Fabry-Pérot saturable absorber, D-SAM dispersion compensated saturable absorber mirror, and so on[57]. However the SESAM technology, pioneered by Knox[58] and Keller[57], due to the relative easy control on the manufacturing parameters and development of semiconductor planar technologies, brought the device to mass use in the solid state laser industry. The structures of such mirrors vary depending on the desired characteristics and the fact that it can be optimised almost independently from the gain material made the SESAM a particularly useful device. Other than the recovery time, as previously discussed, other parameters that characterise a SESAM are: the modulation depth, ΔR, that is the maximum nonlinear change in reflectivity of the device due to the pulse formation, the non-saturable losses, δ_{NS} as the static losses due to the mirror used as a substrate, the saturation fluence, ϕ_{sat}, that is the minimum fluence that is required to bleach the absorber and reach transparency, and ultimately the spectral bandwidth, $\Delta\lambda$ that is the range of wavelengths where the SESAM can act as a saturable absorber.

All five parameters have to be carefully tailored to ensure a stable modelocking regime.
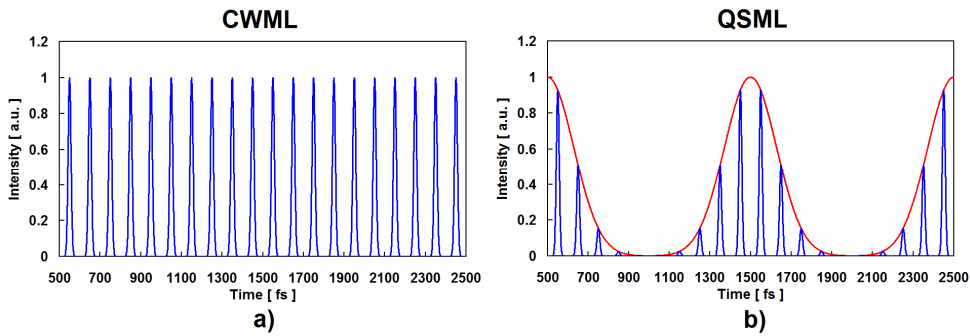

Fig 1.5 The two types of modelocking, a) continuous wave modelocking, (CWML) and b) Q-switched modelocking (QSML).

The major cause of instability in SESAM modelocked systems is due to Q-switching[57], indeed the saturable absorber is *de facto* a shutter inserted in the cavity and that makes of it a very good passive Q-switch. There are many situations that could turn a SESAM into a passive Q-switch, the most important one is an excessive modulation depth ΔR. In such a case, the train of pulses is superposed on a slower Q-switch pulse as shown in fig 1.5b. Other causes are often found in the long lifetimes of the lasing level that glass based lasers have and the operation near modelocking threshold condition[57]. It is therefore useful to define the following two modelocked regimes: *continuous wave modelocking (CWML)*, represented in fig 1.5a and the *Q-switched modelocking* QSML represented in fig 1.5b. It is very easy to identify the QSML: in the RF spectrum of the signal probed with a fast detector the AM modulation sidebands can be detected. During QSML operations the fluence of the pulses can become very high indeed and overcome the damage threshold of the saturable absorber. Figure 1.6 shows the damage recorded in some of our SESAMS.
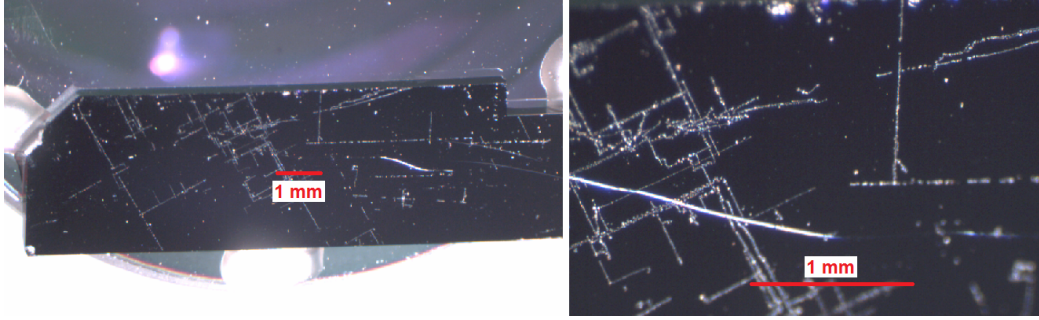
Fig 1.6 The damage due to Q-switching instabilities that were sustained by some of the SESAM used in this research.

1.4.4 Measurements of laser pulses

The characterisation of an ultrafast pulse is very important and to that end it needs to be defined which properties are most relevant to our research. The parameters that fully characterise an ultrafast pulse are: repetition rate υ_{REP}, energy E_P, peak power P_M, duration τ_P, optical bandwidth $\Delta\lambda$, time-bandwidth product TBP, electric field distribution $E(t,\omega)$, phase spectrum $\phi(t,\omega)$. Many techniques have been developed and refined over the years to provide details on the measured pulses to different degrees of accuracy. Most of the measurement systems available in the market are unfortunately

optimised for wavelengths from 0.8 to 1.5 μm due to the emission wavelengths of the Ti:Sapphire and to the extensive telecom applications. There is therefore a lack, to date, of commercially available measurement technologies for the emission wavelengths of our femtosecond laser systems around the 2 μm region.

In this project to get an initial characterisation, it was necessary to provide a measurement of ν_{REP}, τ_P, and TBP. The use of an InGaAs PIN photodiode (Hamamatsu G8422-03) reversely biased could provide a fast enough response to be able to detect ν_{REP} and any Q-switching instabilities, while an Intensity Autocorrelation system, IAC[59] was built to measure τ_P. In order to speed up the process and guarantee the same degree of accuracy for all measurements a simple LabVIEW^{TM} program was created. Fig 1.7 shows the screenshot of the program.
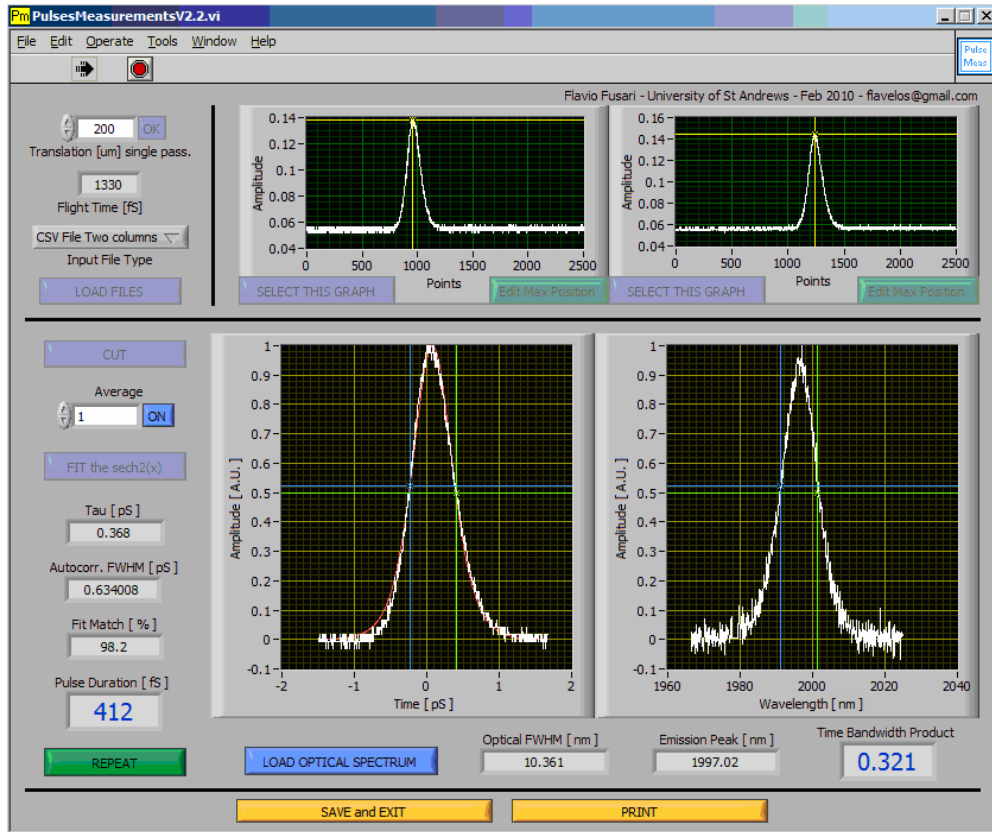
Fig 1.7 The LabVIEW^{TM} screenshot of the program that was created to automatically retrieve the pulses' duration and TBP from the autocorrelation traces.

Two autocorrelation traces were loaded into the program and the space distance imposed by moving the reference reflector of the IAC system for the calibration. The program could then automatically produce a measure of τ_P and once the optical spectrum was loaded also a measure of TBP.

1.5 Conclusions and Synopsis

In this introductory chapter the 50th anniversary of the invention of the laser was remembered in section 1.1 while an overview of the applications of femtosecond lasers was also given. The motivations supporting this research were reported in section 1.2 with the description of the applications of 2 µm CW and pulsed laser systems. In section 1.3 and 1.4 some of the basic concepts needed to introduce the work were explained.. This chapter has served as the introduction for this work, in Chapter 2 the detailed spectroscopical characterisations of the laser systems are introduced and Chapter 3 and 4 report the CW characterisations of glass based bulk lasers. Chapter 5 describes the successful modelock characterisations and the creation, for the first time, of femtosecond glass based 2 µm bulk lasers.

1.6 References

[1]   T. H. Maiman, "*Stimulated Optical Radiation in Ruby*", Nature, **187**, pp. 493-494, (1960).

[2]   A. Einstein, "*Zur quantentheorie der Strahlung*", Physikalische Zeitschrift, **18**, p. 121, (1917).

[3]   A. L. Schawlow and C. H. Townes, "*Infrared and Optical Masers*", Physical Review Letters, **112**, p. 1940, (1958).

[4]   M. H. Anderson*, et al.*, "*Observation of Bose-Einstein Condensation in a Dilute Atomic Vapor*", Science, **269**, pp. 198-201, (1995).

[5]   URL: http://nobelprize.org/nobel_prizes/chemistry/laureates/1999/index.html

[6]   A. H. Zewail, "*Femtochemistry: Atomic-Scale Dynamics of the Chemical Bond Using Ultrafast Lasers (Nobel Lecture)*", Angewandte Chemie International Edition, **39**, pp. 2586-2631, (2000).

[7]   W. H. Knox, "*Ultrafast technology in telecommunications*", Selected Topics in Quantum Electronics, IEEE Journal of, **6**, pp. 1273-1278, (2000).

[8]   R. P. Schreieck*, et al.*, "*All-optical switching at multi-100-Gb/s data rates with Mach-Zehnder interferometer switches*", Quantum Electronics, IEEE Journal of, **38**, pp. 1053-1061, (2002).

[9]   P. W. Juodawlkis, *et al.*, "*Optically sampled analog-to-digital converters*", Microwave Theory and Techniques, IEEE Transactions on, **49**, pp. 1840-1853, (2001).

[10]   P. J. Delfyett, *et al.*, "*Signal processing at the speed of lightwaves [photonic ADCs]*", Circuits and Devices Magazine, IEEE, **18**, pp. 28-35, (2002).

[11]   S. Link and et al., "*Femtosecond spectroscopy*", Journal of Physics: Condensed Matter, **13**, p. 7873, (2001).

[12]   X. Liu, *et al.*, "*Laser ablation and micromachining with ultrashort laser pulses*", IEEE Journal of Quantum Electronics, **33**, pp. 1706-1716, (1997).

[13]   M. Niemz, *Laser-Tissue Interactions: Fundamentals and Applications*. Berlin: Springer-Verlag, 1996, Isbn: 3540721916.

[14]   I. G. Pallikaris and D. S. Siganos, "*Excimer Laser In Situ Keratomileusis and Photorefractive Keratectomy for correction of high myopia*", Journal of Refractive and Corneal Surgery, **10**, pp. 498-510, (1994).

[15]   D. X. Hammer, *et al.*, "*Experimental investigation of ultrashort pulse laser-induced breakdown thresholds in aqueous media*", Quantum Electronics, IEEE Journal of, **32**, pp. 670-678, (1996).

[16]   K. T. Tsen and et al., "*Inactivation of viruses with a very low power visible femtosecond laser*", Journal of Physics: Condensed Matter, **19**, p. 322102, (2007).

[17]   D. Huang, *et al.*, "*Optical Coherence Tomography*", Science, **254**, pp. 1178-1181, (1991).

[18]   R. F. Begley, *et al.*, "*Coherent anti-Stokes Raman spectroscopy*", Applied Physics Letters, **25**, pp. 387-390, (1974).

[19]   M. Hentschel, *et al.*, "*Attosecond metrology*", Nature, **414**, pp. 509-513, (2001).

[20]   A. A. Kaminski, *Crystalline Lasers: Physical Processes and Operating Schemes*: CRC Press, 1996, Isbn: 0-8493-3720-8.

[21]   J. Limpert, *et al.*, "*The rising power of fiber lasers and amplifiers*", IEEE Journal of Selected Topics in Quantum Electronics, **13**, pp. 537-545, (2007).

[22]   C. Kallinger, *et al.*, "*A flexible conjugated polymer laser*", Advanced Materials, **10**, pp. 920-+, (1998).

[23]   J. L. Doualan, *et al.*, "*Spectroscopic properties and laser emission of Tm doped ZBLAN glass at 1.8 μm*", Optical Materials, **24**, pp. 563-574, (2003).

[24] V. K. Tikhomirov, *et al.*, "*Gain cross-sections of transparent oxyfluoride glass-ceramics single-doped with Ho^{3+} (at 2.0 μm) and with Tm^{3+} (at 1.8 μm)*", Journal of Alloys and Compounds, **436**, pp. 216-220, (2007).

[25] I. T. Sorokina and K. L. Vodopyanov, *Solid-state mid-infrared laser sources*. Berlin ; New York: Springer, 2003, Isbn: 3540006214.

[26] B. M. Walsh, "*Review of Tm and Ho materials; spectroscopy and lasers*", Laser Physics, **19**, pp. 855-866, (2009).

[27] A. Godard, "*Infrared (2-12 μm) solid-state laser sources: a review*", Comptes Rendus Physique, **8**, pp. 1100-1128, (2007).

[28] H. Ludwig, *et al.*, "*First experiences with a 2.0-μm near infrared laser system for neuroendoscopy*", Neurosurgical Review, **30**, pp. 195-201, (2007).

[29] H. C. Ludwig, *et al.*, "Endoscopic cystoventriculostomy and ventriculocysternostomy using a recently developed 2.0-micron fiber-guided high-power diode-pumped solid state laser in children with hydrocephalus," in *Proceedings SPIE*, San Jose, CA, USA, 2005, pp. 558-565.

[30] A. Marks and J. Teichman, "*Lasers in clinical urology: state of the art and new horizons*", World Journal of Urology, **25**, pp. 227-233, (2007).

[31] X. Shu-Jie, *et al.*, "*Thulium Laser versus Standard Transurethral Resection of the Prostate: A Randomized Prospective Trial*", European urology, **53**, pp. 382-390, (2007).

[32] K. Scholle, *et al.*, "*Single mode tm and Tm,Ho : LuAG lasers for LIDAR applications*", Laser Physics Letters, **1**, pp. 285-290, (2004).

[33] N. Coluccelli, *et al.*, "*Tm-doped LiLuF4 crystal for efficient laser action in the wavelength range from 1.82 to 2.06 ?m*", Optics Letters, **32**, pp. 2040-2042, (2007).

[34] N. Schulz, *et al.*, "*High-brightness long-wavelength semiconductor disk lasers*", Laser & Photonics Reviews, **2**, pp. 160-181, (2008).

[35] J. Wu, *et al.*, "*2 μm lasing from highly thulium doped tellurite glass microsphere*", Applied Physics Letters, **87**, p. 211118, (2005).

[36] M. A. Watson, *et al.*, "*Synchronously pumped CdSe optical parametric oscillator in the 9?10 ?m region*", Optics Letters, **28**, pp. 1957-1959, (2003).

[37]   J. H. V. Price, *et al.*, "*Mid-IR Supercontinuum Generation From Nonsilica Microstructured Optical Fibers*", Selected Topics in Quantum Electronics, IEEE Journal of, **13**, pp. 738-749, (2007).

[38]   R. R. Gattass and E. Mazur, "*Femtosecond laser micromachining in transparent materials*", Nature Photonics, **2**, pp. 219-225, (2008).

[39]   R. C. Sharp, *et al.*, "*190-fs passively mode-locked thulium fiber laser with a low threshold*", Optics Letters, **21**, pp. 881-883, (1996).

[40]   G. Imeshev and M. Fermann, "*230-kW peak power femtosecond pulses from a high power tunable source based on amplification in Tm-doped fiber*", Optics Express, **13**, pp. 7424-7431, (2005).

[41]   C. Rullière, *Femtosecond Laser Pulses*, 2nd XVI ed., 2005, Isbn: 978-0-387-01769-3.

[42]   A. E. Siegman, *Lasers*. Mill Valley, Calif. ; Sausalitio, CA: Science Books, 1986, Isbn: 0935702113.

[43]   W. Koechner, *Solid-state laser engineering*, 6th rev. and updated ed. New York: Springer, 2006, Isbn: 9780387290942.

[44]   I. Walmsley, *et al.*, "*The role of dispersion in ultrafast optics*", Review of Scientific Instruments, **72**, pp. 1-29, (2001).

[45]   W. Sellmeier, "*Zur Erklärung der abnormen Farbenfolge in Spectrum einiger Substanzen*", Annalen Physic Chemie, **143**, p. 271, (1871).

[46]   R. L. Fork, *et al.*, "*Negative dispersion using pairs of prisms*", Optics Letters, **9**, pp. 150-152, (1984).

[47]   H. A. Haus, "*Mode-locking of lasers*", Ieee Journal of Selected Topics in Quantum Electronics, **6**, pp. 1173-1185, (2000).

[48]   M. Yamane and Y. Asahara, *Glasses For Photonics*: Cambridge University Press, 2007, Isbn: 0-521-58053-6.

[49]   R. Paschotta, *Encyclopedia of Laser Physics and Technology*. Berlin: Wiley-VCH, 2008, Isbn: 978-3-527-40828-3.

[50]   D. E. Spence, *et al.*, "*60-Fsec Pulse Generation from a Self-Mode-Locked Ti-Sapphire Laser*", Optics Letters, **16**, pp. 42-44, (1991).

[51]   F. X. Kartner, *et al.*, "*Soliton mode-locking with saturable absorbers*", IEEE Journal of Selected Topics in Quantum Electronics, **2**, pp. 540-556, (1996).

[52] H. Haus, "*Parameter ranges for CW passive mode locking*", Quantum Electronics, IEEE Journal of, **12**, pp. 169-176, (1976).

[53] A. Siegman and D. Kuizenga, "*Modulator frequency detuning effects in the FM mode-locked laser*", Quantum Electronics, IEEE Journal of, **6**, pp. 803-808, (1970).

[54] V. Magni*, et al.*, "*Closed form gaussian beam analysis of resonators containing a Kerr medium for femtosecond lasers*", Optics Communications, **101**, pp. 365-370, (1993).

[55] V. Magni*, et al.*, "*Astigmatism in Gaussian-beam self-focusing and in resonators for Kerr-lens mode locking*", Journal of the Optical Society of America B-Optical Physics, **12**, pp. 476-485, (1995).

[56] H. W. Mocker and R. J. Collins, "*Mode competition and self-locking effects in a q-switched ruby laser*", Applied Physics Letters, **7**, pp. 270-273, (1965).

[57] U. Keller*, et al.*, "*Semiconductor saturable absorber mirrors (SESAM's) for femtosecond to nanosecond pulse generation in solid-state lasers*", IEEE Journal of Selected Topics in Quantum Electronics, **2**, pp. 435-453, (1996).

[58] W. H. Knox*, et al.*, "*Femtosecond Excitation of Nonthermal Carrier Populations in GaAs Quantum Wells*", Physical Review Letters, **56**, p. 1191, (1986).

[59] L. P. Barry*, et al.*, "*Autocorrelation of ultrashort pulses at 1.5 μm based on nonlinear response of silicon photodiodes*", Electronics Letters, **32**, pp. 1922-1923, (1996).

2. STRUCTURE AND SPECTROSCOPY OF GAIN MEDIA AND ACTIVE IONS

2.1 Chapter Synopsis

In this chapter the materials characterisations of the different samples used throughout this thesis are presented. The introductory part treats the basic nature of glass as it is important to know how glass forms and is created in order to be able to control and design the laser elements.

Active materials for laser generation which are a combination of glass hosts and *triply ionized rare earth ions* Tm^{3+} and Tm^{3+}-Ho^{3+} were used in this research. The chemical and physical characteristics of glasses are investigated in section 2.2. The mechanical and the electronic interaction of such active ions with the host are treated fully in Section 2.3. In section 2.4 the manufacturing technique and the Raman spectra for the different glasses studied are reported and analysed. Their spectroscopic investigations are presented in section 2.5, in preparation for the laser experiments that are discussed in chapters 3 and 4. Finally, a comparison between all of the Tm^{3+} samples is shown in section 2.6.

2.2 Chemical and physical characteristics of glasses

2.2.1 Basic structure of optical glasses

We all are familiar with glass as it is used throughout our lives. Its properties of transparency and brittleness are easily appreciated. Its versatility on fabrication, shaping and workability have pushed glass into many sectors of industry, from high precision bearings to the latest consumer electronic gadgets. Furthermore the characteristics of chemical stability that glass possesses are appreciated in medicine and food processing[1].

The nature of glass can be explained from mainly two different perspectives both equally valid. In the first, the glass is in a state between a liquid and a solid, namely a highly viscous liquid. In fact one of the peculiarities of the glass materials is the lack of a defined transition between states of the matter, heating glass results in a continuous decrease of the viscosity, going through annealing, softening and finally melting points. Shelby defines glass as "an amorphous solid […] exhibiting a region of glass transformation behavior" [2], such glass transition diagram is described in the next section and is at the basis of the fabrication technique we use in this PhD. On the other hand the American Society for Testing Materials defines glass as "an inorganic product of fusion which has been cooled to a rigid condition without crystallization" [3]. The second approach, introduced by Zachariasen on a fundamental paper written in 1932[4], defines glass as a solid that lacks of long range crystalline structure. Crystals are present but their periodicity is somehow distorted generating the glassy form, this in turn brings forth the peculiar characteristics that are described in the next section. The most common example can be given in the case of SiO_2 based compounds, the Silica glass.
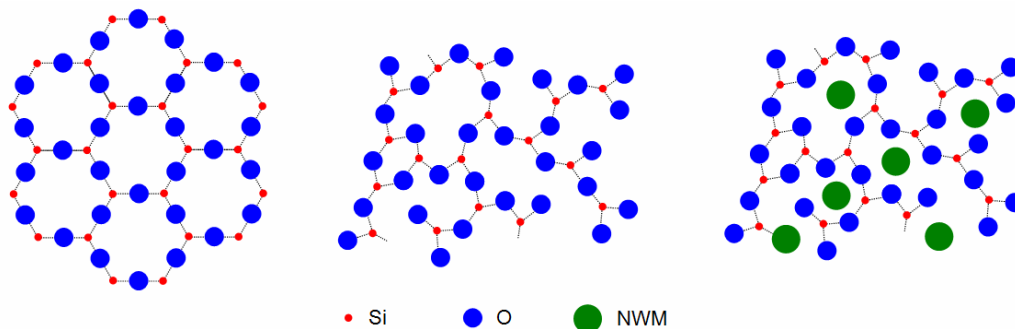

Fig 2.1 From the left the cristobalite crystal structure, the basic structure of Silica glass and the structure of the Silica glass in presence of network modifiers.

In its ordered state, SiO_2 forms the cristobalite crystal which is a polymorphic state of the quartz crystal[5], in disordered structure it represents the base of the Silica glasses. In Fig 2.1 the various structures are represented[4]. Glasses could then, in principle, be formed by a single SiO_2 network but other components are usually added to decrease the melting point or give the desired properties. The amount of disorder in the network is caused by cations included in the composition and from a general point of view three different types of ions can be distinguished[5]: network forming ions (*NWF)* which act as formers of the glass network and are present in highest proportion in the composition, network modifiers ions (NWM), which modify the network and aid in the glass formation, and dopants ions (DOP), which are used as active ions. Usually DOP take the same places of the NWM in the network.

2.2.2 Formation of optical glasses

The immediate question is: is any inorganic compound able to form glass structures? The answer is no, however predications can be made with the Stanworth[6] *glass formation model*. In this model, four different classes of anions can be identified: O for *Oxides*, F and Cl for *Halide*s, Br for *Bromides* glasses and S, Se, Te forming the *Chalcogenide* families. Any cation, combined with such anions will make a good NWF if the bonds formed are ionic and covalent in equal proportions, but also cations that tend to form more ionic bonds than covalent in percentage make good NWMs. The chemical composition can be changed widely, the requirements of rigid stoichiometric ratios found in crystals are relaxed and electrical neutrality is the only property that has to be preserved in the glassy structure, this is an enormous advantage that glasses have over the crystalline counterparts. The SciGlass database logs and contains over 320000 different compositions to date[7]. The thermodynamic phase transition graph presented in Fig 2.2 shows the formation of the glass according to the definitions and the experimental evidence[2]. In materials that form crystalline compounds the enthalpy, H, decreases abruptly down the red path and at the melting temperature T_X they instantaneously form long periodic range crystals. In the case of compounds that form glassy structures crystallization does not happen at T_X and a supercooled liquid is generated on the blue path.
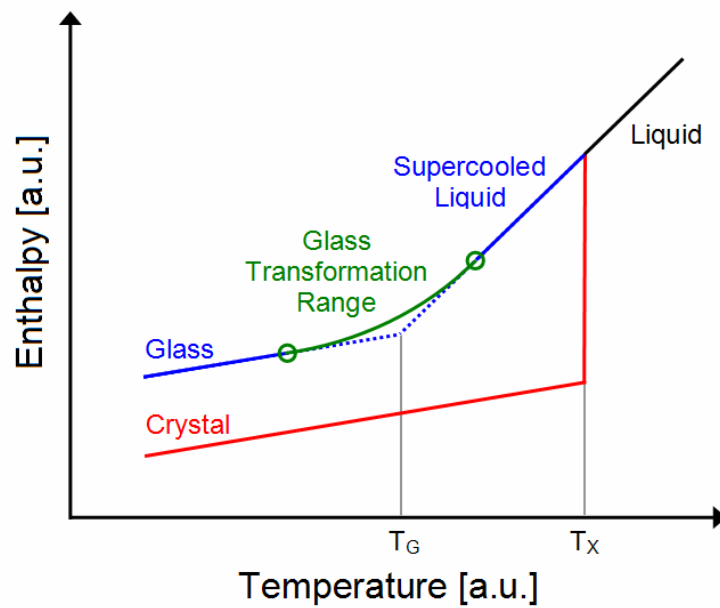
Fig 2.2 The enthalpy graph of glass and crystals formation. The red line highlights the crystalline phase while the blue line the path followed by the glassy compounds.

Reducing the temperature gradually increases the viscosity of the melt and glass starts to form arranging ions in the typical glassy disorder. The process is gradual and at some point the viscosity is so elevated that ions cannot move and the liquid is *frozen* becoming a glass. The temperature range over which this takes place is called the *glass transformation range*, and T_G is by convention dubbed temperature of glass transition. Heating dynamics have also to be tailored to the composition as the enthalpy graph is strongly composition dependent. The quenching has to be rapid enough to avoid the crystallization of the composition and slow enough not to generate strains and internal stresses in the glass compound. Crystals, in fact, form in a glass with a two step process during the supercooled liquid phase, the *growth* process and the *nucleation* process. Decreasing the temperature from T_X the material passes the grow process first and then the nucleation one, if the passage is quick, nucleation happens when very little crystals have formed thereby favouring the glassy state. The higher the difference T_X -T_G the more stable the glass is against crystallization[8]. The principal techniques used for the forming of glass and the consequent doping of it with active ions are the *melt and quenching* method and the *sol-gel* method, the latter provides great results for the dopant distribution but the process is long and difficult to repeat. All our research glasses were produced by melt and quenching and we will focus on it throughout this chapter.

2.2.3 Nature of optical glasses for laser applications

The report of the first laser action in glass-based active media dates back to 1961[9] and the research field has become well established over the years. The glass NWF is in fact chosen depending on the particular application and final shape of the material. For instance, if a short bulk glass is used as an optical amplifier and gain is necessary its composition has to be able to support a high concentration of active ions, chalcogenide glasses are thus perfect for the task, conversely if optical fibers have to be drawn from it the oxides glass are the chosen ones for their viscosity properties.

Most of the commercial optical glasses produced today are oxide based glasses, silicates and phosphates. The kind of glasses used for laser operations is not limited to the oxide types however, but stretches over the other three classes, the halides, the oxyhalides and the chalcogenides. In this respect, a large literature review has been carried out focusing on the 2 μm and the infrared part of the spectrum and it is therefore useful to report some of the previous work done classified by glass families.

The oxides, mostly used in conjunction with two or three network modifiers, include phosphates [10], silicates [11], germanates [12-13], tellurites [14-15] and borates [16]. Halide network formers, namely fluorides[17] and chlorides[18] are extensively used for their transparency stretching over the infrared region[19]. Obtained via a mixture of oxides and halides elements, the main representative of the oxyhalide glasses are the fluorophosphates and chlorophosphates glass. They have low melting temperatures and high ionic conductivity. Finally chalcogenide glasses are made with Selenium[20], Sulphur and Tellurium as NWF and Arsenic, Antimony and Germanium[21] as examples for NWM. Chalcogenide glasses are usually expressed using the atomic percentage of the forming elements i.e. $Ge_3P_3Te_{14}$. They show great transparency in the infrared region up to 20μm, have high refractive indexes and the lowest peak phonon energies among glasses.

2.2.4 Mechanical and optical properties of glasses for laser applications

From a pure material point of view there are quite a few properties that can be identified and that are important for the use of glass. However, in the context of this thesis, a range of key properties can be identified which depend on glass composition. *Fracture*

toughness which addresses the brittleness of the material. *Hygroscopicity*, that is the property of absorption of water molecules from the surrounding atmosphere. *Thermal conductivity* ~1 W/m·K for glasses compared to 40 W/ m·K of Sapphire. *Thermal Expansion Coefficient* that needs to be controlled in bonds with other substrates. *Chemical stability and toxicity* which determines the glass formation phases, the tendency of crystallize and the environmental impact of the compound. *Dopant solubility,* which is the property of the glass of allowing a homogeneous distribution of the active ions over the entire batch volume.

For laser active elements, the interaction of light with the glass is very important and *optical quality*, *linear* and *nonlinear refractive indices*, *dispersion*, and *transparency* play a central role. The phenomenon that most affects the optical quality is the scattering loss. Scattering by small impurities and scattering by particles much smaller than the light wavelength is known as Rayleigh scattering. This has a λ^{-4} dependency and cannot be avoided. The baseline of the Rayleigh scattering is often used to roughly assess the optical quality[22]. The refractive index is generated by and depends on the *polarizability* of the structure and it is higher for highly polarizable systems (e.g. chalcogenide glasses). It interferes with the luminescent emission of the active ions as will be described later in the chapter. The transparency range of glass samples is determined by two cut off regions, the UV cut off and the IR cut off. These depend strongly on the E_G energy gap of the glass and on the phonon vibration and an extensive treatment can be found here[2]. It is sufficient to highlight in this context that low phonon energies glasses tends to transmit longer in the IR and less in the UV region[23] and vice versa. The nonlinear refractive index of glasses, was introduced in section 1.3.3 and plays a fundamental role in Kerr lens modelocking. Its value depends on the composition and is reported in the relevant sections below.

2.3 Rare Earths ions in glasses

2.3.1 Rare earths as active ions in glassy networks

Dopants suitable for laser operations must adhere to several properties and characteristics. They have to have strong absorption bands for efficient excitation and they have to demonstrate high quantum efficiency for good energy transfer between

pump and laser. The composition of the host matrix should, in principle, have only a limited effect on the lasing behaviour of the dopant. All of these characteristics can be found in elements that have inner incomplete electron shells.

The chosen active ions for our research belong to the lanthanide family and are commonly called *Rare Earth*s (RE)[24]. RE have atomic numbers from 57 to 70 and their electrical core is the one of Xenon, their preferred ionisation state in condensed matter is the third: M^{3+} [25]. Their electrons in *5s* and *5p* shell shield the electrons in the *4f* shell almost completely, the result is that the UV through the IR spectra are determined by *4f* electrons[5, 26]. From all of the possible RE dopants we necessarily exclude the radioactive Pm^{3+}, and consider the ones with lowest energy emitting transition around the 2 μm region: Ho^{3+} and Tm^{3+}.

The transition processes involved in RE ions *4f* energy levels were extensively studied by G.H. Dieke *et al* in the 1960's [27]. Fig 2.3 below depicts the energy levels of the *4f* electrons of Ho^{3+} and Tm^{3+} up to 22000 cm^{-1}, and the major radiative transitions.
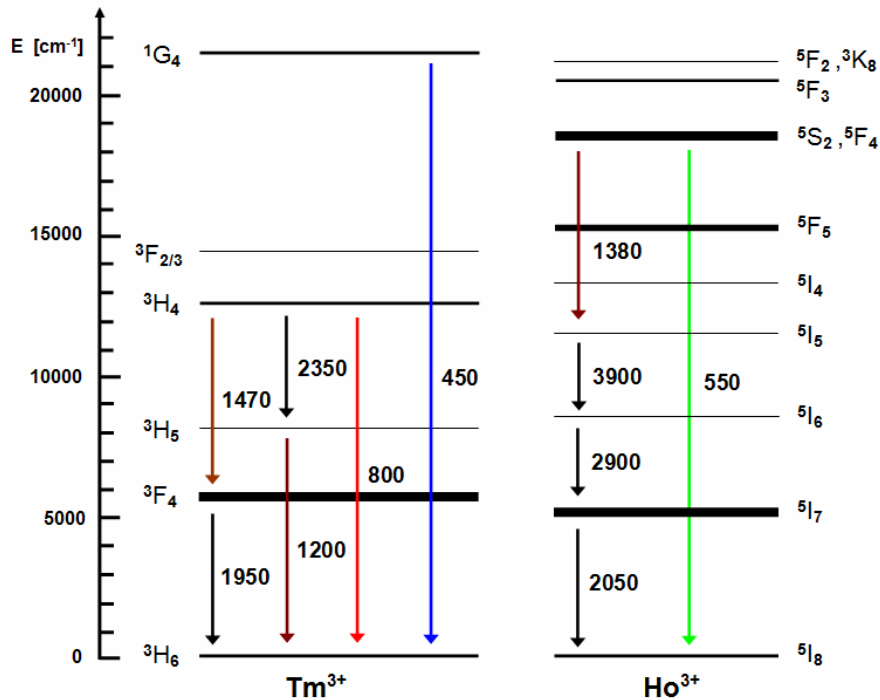

Fig 2.3 The Tm^{3+} and the Ho^{3+} ions energy levels up to 22000 cm^{-1}. The lowest emitting transition is $^3F_4$ for Tm^{3+} and $^5I_7$ for Ho^{3+}. Arrows highlight the main radiative transitions and numbers are reported in nm. Levels are weighed with their respective lifetime.

The levels in Fig 2.3 are labelled following the usual quantum-mechanical notions of Russel-Saunders coupling or LS coupling. Levels take the form of $^{2S+1}L_J$ where J is the total angular momentum resulting from the vectorial sum of L the total orbital angular momentum and S the spin angular momentum[5].

The energy level diagram of Fig 2.3 of a rare earth ion included as an impurity is slightly influenced by the host matrix. If the matrix is strongly covalent, i.e. germanate compounds, the shielding effect on levels is stronger and the energy levels slightly shift down[27], conversely on fluoride compounds where bonds tends to be ionic in nature the shielding effect is weaker and energy levels tend to be shifted to slightly higher energies. In regard to VIS/IR absorption spectra we tend then to see absorption peaks to longer wavelengths on germanate based compounds rather than fluoride based ones.

Furthermore, in crystalline materials Stark line splitting brings forth well defined and resolved energy sublevels the so called *homogeneous broadening*. In glass counterparts, the disorder in the local ionic structure results in a wide range of local electric fields which creates poorly resolved Stark sublevels the so called *inhomogeneous broadening*. This actually affects the optical transitions creating many available sub-transitions, therefore in glasses the emission spectra is usually smoother and broader and the excited state lifetimes are longer than in crystals, generally in the ms order magnitude[28].

2.3.2 Mechanical Interactions

Phonons are the quantum-mechanical description of the vibrations of the lattice in host glasses. Their behaviour is described in classical mechanics as waves and vibrational modes that propagates through the glass structure, however when quantized they can also be seen as quasi-particles and they can be treated by integer numbers. Phonons are strictly connected to the nature of the glass and they interact with the photons that are emitted and absorbed by the RE ions in the material. Phonons are responsible for macroscopic effects like thermal conductivity but also take part in well known scattering processes like Brillouin scattering and Raman scattering. The phonon energy can be written as $\hbar\omega$. Lattice phonons generate and annihilate on a much faster timescale than the electronic energy levels' lifetimes and thus can be responsible for

assisting absorption transitions[29] and supply energy in quasi-resonant energy transfers[30]. On the other hand, the process of relaxation of excited ions happens in two fundamental ways, the *radiative* emission which will be extensively treated in the next section and the *nonradiative* emission whereby phonons bridge the gap to the lower level and conserve the energy. Phonon energies range on the order of 300-1000 cm^{-1} and this means that more than one phonon must be emitted to bridge large gap in nonradiative transitions, the process is called *multi-phonon relaxation*. It obviously is a loss mechanism, decreasing the lifetime of ions in all energy lines and dumping heat in the gain material. The Raman spectrum provides further understanding of the phonon energy in the structure and is discussed in section 2.4 below.

2.3.3 Electronic Interactions

The rare earth ions suspended in the host definitely interact with the host but also, and importantly, between one another. In this research, the need of reducing the length of active materials for best pump-mode beam matching leads to the requirement for high concentrations of dopants for effective absorption of the pump beam. The mean distance between active ions is then reduced and the probability of formation of clusters and of greater energy exchanges increases. This in turn quenches the fluorescence and the lifetime of the energy levels. A very good example of fluorescence quenching of the 1.8 µm Tm^{3+} : $^3F_4 \rightarrow {}^3H_6$ transition for different dopant concentrations in different glasses was studied by Zou et al.[31]. Lifetime normally decreases with concentration and an example is reported by R. Balda et al.[32] in Tellurite glasses for Tm^{3+}. In the case of single doped Tm^{3+} materials an empirical model of the quenching effect can be obtained by simple equations[33].

In the presence of other active ions, *sensitizers*, various energy transfers take place and the modelling can further increase in complexity. The pump energy is transferred to the active ions through two main self-explanatory processes: the most important *ground state absorption (GSA)* and the parasitic *excited state absorption (ESA)*, once the energy is injected into the material volume it is redistributed via many different processes, briefly depicted in Fig 2.4. The *Nonresonant energy transfers (NET)* that happens between ions of different nature is aided by phonons likewise in the $Tm^{3+} \rightarrow$

Ho^{3+} system of Fig 2.4 and the two ions take the name of *donor* and *acceptor*. This type of energy transfer is very important as the mechanism allows the use of a greater number of pump sources. Resonant energy transfers happen instead between same levels of ions of the same nature they take the name of *energy migrations (EM)* and they are ideally lossless.

Upconversion (UC) and *Energy Transfer Upconversion (ETU)*. The UC phenomenon is clearly visible in glasses doped with Tm^{3+} that glow blue when pumped with infrared radiation. In a UC process an active ion is raised to a high energy state by virtue of another ion relaxing to a lower energy state. The ETU happens when an excited ion relaxes to a lower energy state promoting another ion from ground to a higher energy state, it can be thought as the "inverse" of the cross-relaxation.

Cross relaxation (CR). In CR, fundamental in Tm^{3+} systems pumped in $^3H_4$, an ion that relaxes from a high energy state promotes another ion from the ground state. The CR mechanism is a gain mechanism as it can act to populate the lasing level.
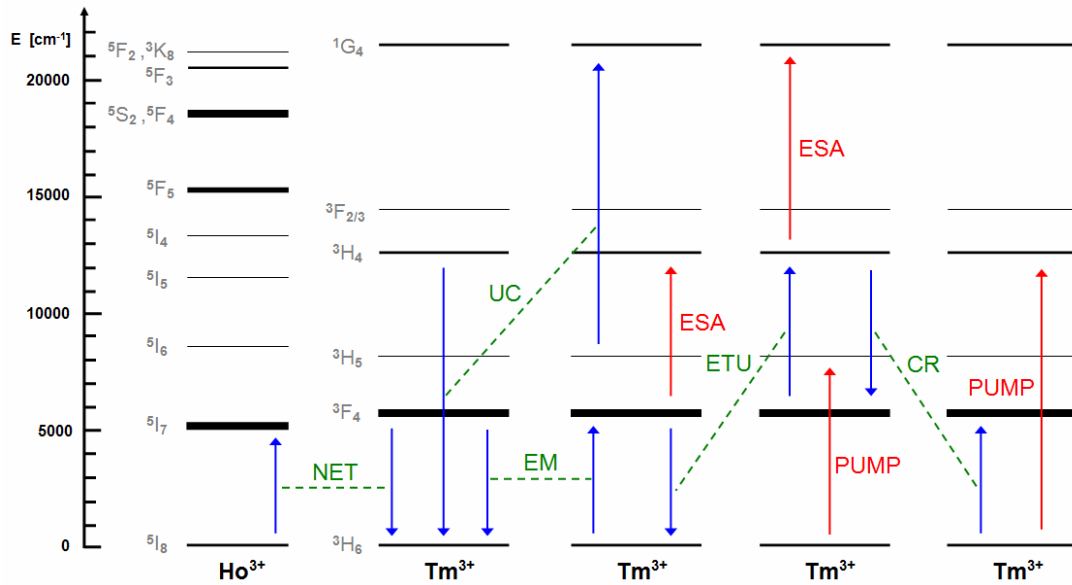

Fig 2.4 Main energy transfers in Tm^{3+} and Tm^{3+}-Ho^{3+} systems. Solid arrows highlight the transitions while dashed ones the phonon-assisted transitions. Nonresonant Energy Transfer, NET, Upconversion UC, Energy Migration EM, Energy Transfer Upconversion ETU, Cross Relaxation CR, Excited State Absorption ESA.

Many models have been developed over the years on the energy transfer mechanisms introduced, the most used ones are: Yokota-Tanimoto[34], Burshtein[35], Inokuti-Hirayama[36] and the Forster-Dexter[37].

2.3.4 Emission cross section

The emission cross section is one of the most important spectroscopic parameters for a laser material and it is directly connected to the gain of the material. It expresses the probability of photon emission from a particular level and it is inversely proportional to the value of lasing threshold as was shown in formula (3.5). In order to estimate the emission cross sections two main methods are commonly used: the Füchtbauer-Ladenburg approach (FL)[38] and McCumber theory[39] which is also known as the *reciprocity method*. The FL approach is cumbersome as it needs the radiative lifetimes and the branching ratios that have to be calculated through the Judd-Ofelt model[40-41]. Conversely under McCumber theory, the emission cross section and the absorption cross section are scaled to one another by the energy difference between the lowest Stark components of the upper and lower level manifolds. Formula (2.1) uses the value λ_{ZL} as an estimation of such energy and it is usually referred as the zero-phonon line. λ_{ZL} was taken from the work of Payne et al.[38] its value is 1784 nm for Tm^{3+} and 1941 nm for Ho^{3+} systems.

$$\sigma_E(\lambda) = \sigma_A(\lambda) \cdot \frac{Z_L}{Z_U} \cdot \exp\left[\frac{hc}{k_B T} \left(\frac{1}{\lambda_{ZL}} - \frac{1}{\lambda} \right) \right] \tag{2.1}$$

σ_A is the absorption cross section, h is the Planck constant, c is the speed of light in vacuum, k_B is the Boltzmann constant, T is the temperature in K. The ratio Z_L/Z_U is the ratio of the two partition functions of the lower and upper manifolds. Partition functions are defined in statistical mechanics[42] as the functions that map the probabilities of occupancy of the thermally created microstates that exist around the Stark levels. The value of the ratio of the partition functions is usually measured at low temperatures and it is a pure number. In the case of our glasses the value was taken of 1.512 for Tm^{3+} and 0.81 for Ho^{3+} systems[38].

$$\sigma_G(\lambda) = \beta \cdot \sigma_E(\lambda) - (1 - \beta) \cdot \sigma_A(\lambda) \tag{2.2}$$

Once the emission cross section is known, an estimation of the gain in the material can be given introducing the inversion factor β parameter, used in formula (2.2) that ranges from 0 to 1. Assuming a completely inverted population and the absence of reabsorption losses the maximum gain, also referred as the saturated gain coefficient *g* can be calculated in dB/cm by[43]:

$$g[dB/cm] = 10\log_{10}(\exp(\sigma_E \cdot n))\qquad(2.3)$$

where n is the concentration of ions in ions/cm^3 present in the material.

2.4 Manufacturing and nano-crystalline structure of active glasses

2.4.1 Tellurium Oxide glasses

Tellurium oxide TeO$_2$ glasses have been studied for over 150 years[44] and extensively used for their particular characteristics. Their unique glass structure and their formation seemed, at first, to defeat the Zachariasen glass formation rules and broad research has been carried out on the material to fully understand it[45].

Tellurite glasses were selected for use in this work because of their very good properties for infrared laser generation. Their peak phonon energy is low ~750 cm^{-1} compared to the silicate compositions, their IR cut off is therefore shifted to longer wavelengths and they have a transparency window from 0.35 to 5 μm. TeO$_2$ Glasses are chemically and physically stable with high corrosion resistance and high linear refractive index ~2 which in turn enhances the radiative rates and the emission cross sections[46]. Rare earth solubility is very high and the non linear refractive index in these glasses is higher than other species[47]. Table 2.1, compares some average values of properties found for Tellurite glasses against Silica and Fluoride materials.

Property	Tellurite	Silicate	Fluoride
Refractive index	2	1.46	1.5
Abbe Number	10-20	80	60-110
Nonlinear refractive index [cm^2/W]	2.5 x 10^{-15}	10^{-16}	10^{-17}
Peak phonon energy [cm^{-1}]	800	950	500
Transmission range [nm]	350-5000	200-2500	200-7000
Fractional ionic bonding character	covalent-ionic	ionic-covalent	ionic

Tab 2.1 Some of the physical characteristics of Tellurite glasses in comparison with Silica and Fluorides from[47].

TeO$_2$ does not form in the glass state by itself and there is a requirement for one or more NWM's. They are usually picked from the alkali metals and earlier work has confirmed the reliability of Zinc, Sodium and Germanium oxides.

In our case, glasses were formed by the *melt and quenching* technique. As the name suggests, a mixture of highly pure raw materials is prepared and thoroughly mixed, then melted in gold or platinum crucibles, and rapidly quenched in metal casts to room temperature. Samples were prepared from high purity (>99.99%) starting chemicals of TeO_2, ZnO, Na_2CO_3, GeO_2. The host compositions were chosen as $80TeO_2 - 10ZnO - 10 Na_2O$ in mol% and $75 TeO_2 - 10 ZnO - 10 Na_2O - 5 GeO_2$ mol% in batches of 10 to 15 g. Doping was added in the batches with Tm_2O_3 and Ho_2O_3 in the wt% concentration desired. Section 2.5 report the list of samples formed. Each batch was subsequently mixed and thoroughly ground on a mortar before being moved into respective gold crucibles. It was then melted at 800 °C for 2 hours and homogenized for 1 hour at 750 °C in an atmosphere of flowing dry O_2. The sodium carbonate Na_2CO_3 separates in CO_2 that is expelled by the oxygen flow and Na_2O that binds in the melt. The melt was then cast into a preheated 265 °C brass mould and then annealed for 3 hours at 285 °C before being allowed to cool slowly to room temperature in the furnace. Samples were then roughly polished for the structural and spectroscopical assessments.
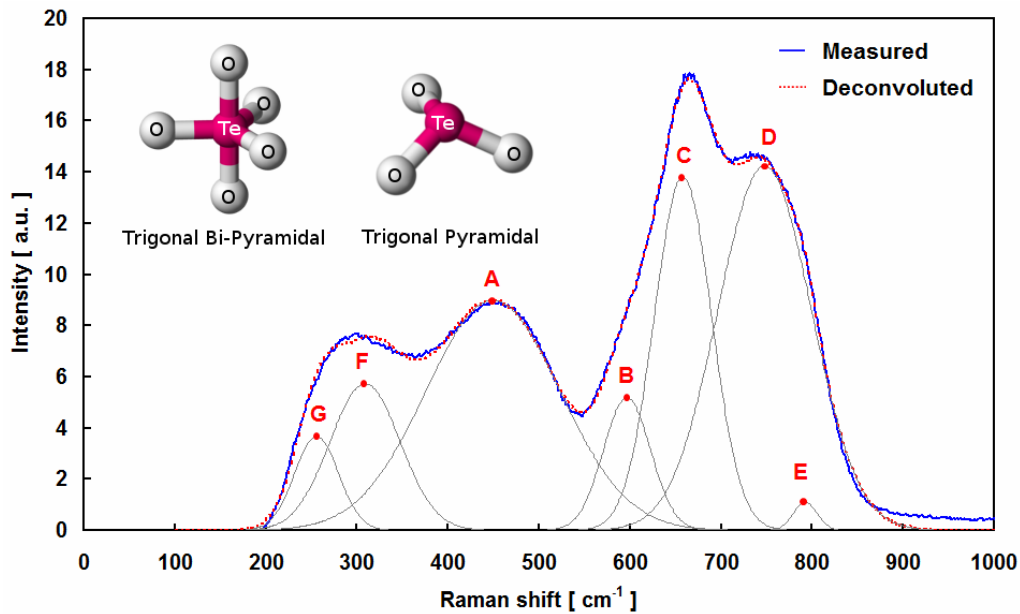

Fig 2.5 The Raman spectra measured for the TZN and its deconvolution in Gaussian vibrations. Peaks are labelled with progressive letters according to the order present in other literature[48]. The inset shows the two most common structural units found in Tellurite glasses.

The values of T_X and T_G in TZN glasses were measured at 425 °C and 290 °C respectively for a T_X-T_G of 135 °C[49] by differential thermal analysis (DTA). The

Raman spectrum of the TZN was measured with a Renishaw system in Leeds University and is depicted in Fig 2.5. Since GeO_2 and the dopants were in very low concentration, the spectra obtained for the TZNG and with different dopants were very similar to the TZN one.

The deconvoluted Gaussian peaks, labelled in line with the literature[48] as A, B, C, D, E have maxima at 449, 596, 657, 747, 792 cm^{-1} respectively. They represent the vibrational modes of the trigonal pyramidal and the trigonal bi-pyramidal structural units of TeO_3, TeO_4 and $TeO_{3+\delta}$ with their binding oxygen. The inset of Fig 2.5 shows such structural units as found in tellurite glasses. The F and G peaks at 308 and 255 cm^{-1} respectively and are due to vibrations in the Zinc and Sodium systems. Extensive explanation of vibrational modes in alkali Tellurite glasses was treated by McLaughlin et al.[50] and Jha et al.[51]. The linear refractive index was measured by the prism coupling technique (Metricon, model 2010) at 532, 633, 1321, 1476, 1500 and 1560 nm and then fitted with the Sellmeier equation (1.11). The resulting curve is plot in Fig 2.6.

$$V_e = \frac{n_e - 1}{n_f - n_c} = 18.3 \tag{2.4}$$

$$n_2 = \frac{2.72\pi \times 10^9 \cdot (n_e - 1)(n_e^2 + 2)^2}{c \cdot n_e \cdot V_e \left[1.517 + \frac{(n_e^2 + 2)(n_e + 1)V_e}{6n_e} \right]^{1/2}} = 5.74 \times 10^{-15} \; [\, cm^2/W] \tag{2.5}$$

From the linear refractive index dispersions two parameters can be extracted, the nonlinear refractive index and the group velocity dispersion or second order dispersion of the glass. The nonlinear refractive index n_2 formula (2.5)[52] can be calculated with the Abbe number V_e (2.4) through the refractive indices at three wavelengths n_f (480 nm) = 2.0635, n_e (546.1 nm) = 2.0946 and n_c (643.8 nm) = 2.0366. The result obtained ($5.74 \cdot 10^{-15}$ cm^2/W) is in reasonable agreement with the value of $4.67 \cdot 10^{-15}$ cm^2/W reported in literature[53] for tellurite network glasses and measured with three wave frequency mixing at 1.06 μm.
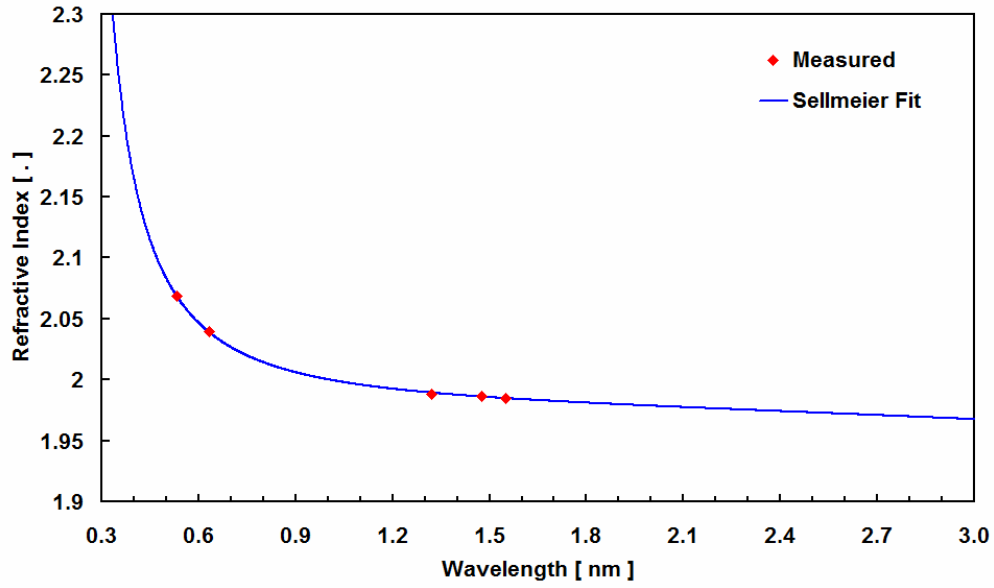
Fig 2.6 The linear refractive index dispersion for TZN glasses. The curve is a Sellmeier fit of values measured at 532, 633, 1321, 1476, 1500 and 1560 nm.
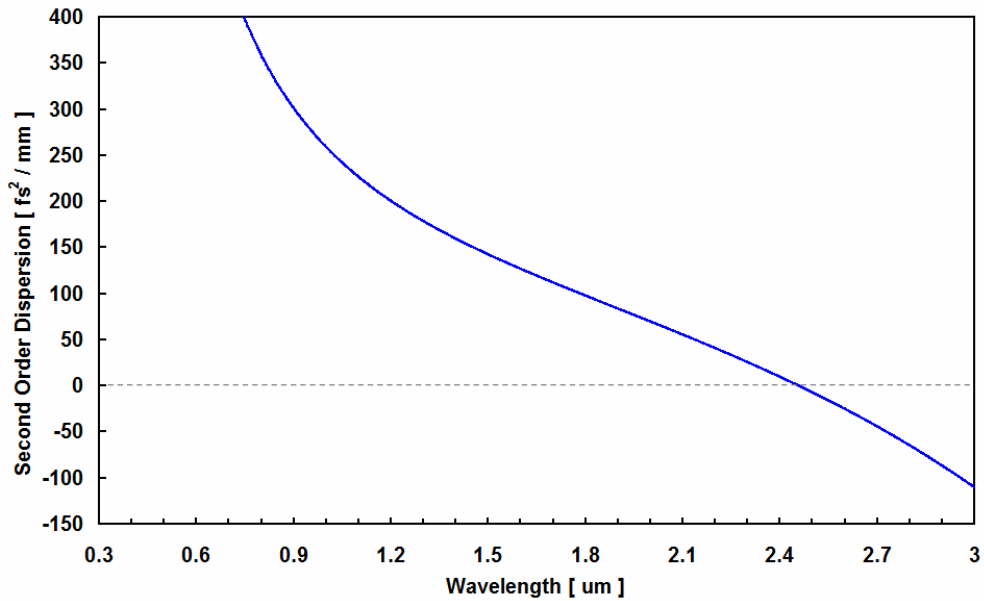

Fig 2.7 The second order dispersion of the TZN compounds as calculated by derivation of the Sellmeier fit. The curve crosses the zero line at 2450 nm.

The second order dispersion of the glass was calculated by derivation of the Sellmeier fit as outlined in section 1 and the result is plotted in Fig 2.7. It can be seen that the curve crosses the zero dispersion line at 2450 nm and that the dispersion at 1950 nm is around 70 fs^2/mm.

2.4.2 Fluorogermanate Oxide glasses

Glasses based on GeO_2 have excellent chemical durability, high values of hardness and very good IR transmittances[54]. Pure germanate glasses would form glasses by themselves but melting temperatures approach 1500 °C. Furthermore GeO_2 glasses tend to have a structure similar to SiO_2 ones and, due to the size of the Ge atoms the interstitial space to include rare earth ions decreases posing crystallization risk to the material[2]. In order to obtain the desired characteristics it is necessary to steer the glass composition to a multi-component one. Alkali elements are then added to the germanate glasses to decrease the melting point, control viscosity[55] and T_G[56] for fiber drawing and increase the rare earth solubility. For increasing concentrations of alkali ions the refractive index and the density of the germanate compounds reaches a maximum and then decreases. This unusual behaviour was termed *the germanate anomaly*[2] and it is believed to be due to changes in the concentration ratios of tetrahedron and octahedron germanium oxide structural units shown in Fig 2.8[57].

The composition that was chosen for our laser active element was derived from an all-oxides one previously studied in Leeds University by Xin Jiang et al[55]: 56 GeO_2 – 31 PbF_2 – 9 Na_2O – 4 Ga_2O_3. Lead oxide was substituted with lead fluoride for one very important reason. It has been shown in fact that Tm^{3+} ions tend to interact with fluorides and experience a lower local peak phonon energy decreasing the multi-phonon relaxation rates[58]. Moreover the use of PbF_2 is heavily involved in the creation of glass-ceramics and in case of successful result it would have opened new and interesting research scenarios. One sample was created with high purity (>99.99%) starting chemical constituents. They were weighed and mixed in a 15 g batch in ambient atmosphere with 2 wt% of Tm_2O_3 that was added as dopant. The mixture was then transferred to a platinum crucible and melted at 1200 °C for 4 hours under the dry oxygen atmosphere. The melt was stirred once after 2 hours and cast on a preheated brass mould and annealed at 360 °C for 2 hours. The annealing furnace was then turned off and the glass was allowed to cool slowly to room temperature. Since fluorines are very volatile and tend to escape from the compound great care had to be taken to control the temperature and the sample manufacturing in order to guarantee repeatability[56]. The quality of the glass obtained was not fully optimized as lines and small casting defects could be seen in the final samples.
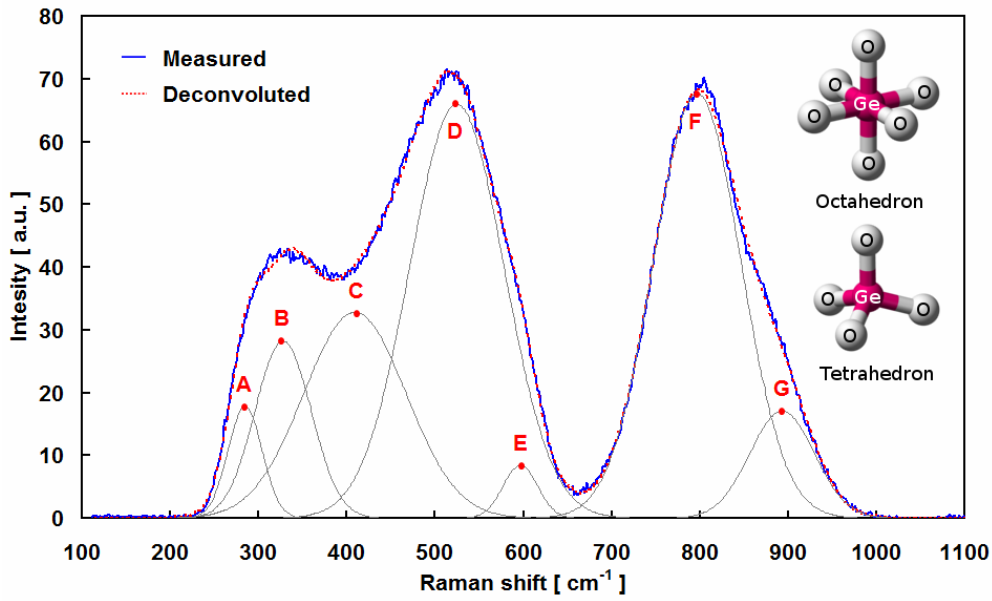
Fig 2.8 The Raman spectrum of the GPNG fluorogermanate glass. Peaks are highlighted with letters and the structural orders are showed on the inset.

Also, analysis of the sample between crossed polarizers showed that some material strains were present. The DTA returned T_X = 575 °C and T_G = 425 °C and a consequent T_X-T_G of 150 °C vouching for the good crystallization stability of the fluorogermanate composition. The deconvoluted peaks of the Raman trace are shown in Fig 2.8. A, B, C peaks at 284, 327 and 409 cm^{-1} respectively are due to the alkali present in the composition[59] while D and E at 524 and 596 cm^{-1} are due to the lead fluorides[60]. Peaks F and G at 796 and 893 cm^{-1} belong to O=Ge=O vibrations[61]. The refractive index was also measured at different wavelengths and was 1.75 around 2 μm. The Abbe number and the nonlinear refractive index calculated by (2.4) and (2.5) were of 42 and 9.5 ·10^{-15} cm^2/W respectively. The second order dispersion was 280 fs^2/mm at 2 μm. The material obtained was yellowish in colour as the UV cut off occurs at longer wavelengths for more covalent glasses.

2.4.3 ZBLAN Fluoride glasses

The fluorozirconate ZrF_4 based ZBLAN glass has been extensively studied and used in the past and was adopted in this project as a comparison for the Tellurite and the Fluorogermanate glass systems[19]. The sample was supplied by Dr David Hollis from the University of West Scotland[62]. ZBLAN belongs to the heavy metal halide glasses

and it is the most chemically stable and durable of the family. Their most widely appreciated characteristics are, exceptionally low losses in the IR due to their ionic bond character, a low peak phonon energy that is around 500 cm^{-1} and the ease of fiber drawing[63]. Unfortunately ZBLAN glasses, being based on fluorine, are inherently hygroscopic and their manufacture has to be carried out carefully in inert atmosphere as reported below. Water is in fact detrimental in all IR glass lasers as it binds to the network in the form of the hydroxyl ion OH$^-$ which has a fundamental absorption peaks around 2.7 µm[2]. Crystran grade materials, which had been packed under dry argon were purchased in the form of small off-cuts of crystal or powder and stored in desiccators. Preparation of the glasses was carried out in a glove box through which dry nitrogen was circulated. Part of the circulation system consisted of two towers filled with a copper/copper oxide catalyst, which, when heated, removed oxygen. Moisture and carbon dioxide were removed with a liquid nitrogen trap. The melting and annealing furnaces were accessible through two ports in the flat part of the preparation area, they both had nitrogen circulation separate from that of the working area. The electric heating elements were wound onto boron nitride, which also formed the inner surfaces of the furnaces. The required materials were weighed in 15 g batch and ground with an agate mortar in the following molar proportions $53.7ZrF_4+ 19BaF_2+ 5LaF_3+ 3AlF_3+ 19NaF$ with 2.0 mol% of TmF_3. They were then mixed together in plastic jars before being placed in platinum crucibles in the melting furnace. The batches of powder were melted at 750 ^{o}C for 1 hour before being poured into brass moulds. They were annealed at 270 ^{o}C for 20 minutes, and then cooled at 2 °C per minute to ambient temperature. The resulted glass had very good optical quality. The Abbe number and the nonlinear refractive index of typical ZBLAN glasses are ~70 and ~$2.4 \cdot 10^{-16}$ cm^2/W[64] respectively. The second order dispersion calculated with data from[65] is of -15 fs^2/mm at 2 µm and has a zero at ~1700 nm.

2.5 Spectroscopy of active materials

2.5.1 Tm^{3+} doped tellurite materials

Many tellurite samples were doped with Tm^{3+} for the laser experiments out of which only three reached lasing threshold and it is interesting in this context to present their

spectroscopic characterisation. The three samples were doped with 1.0, 1.5 and 2.0 wt% Tm^{3+} and were named $Tm_{1.0}$:TZN, $Tm_{1.5}$:TZN and $Tm_{2.0}$:TZNG respectively. Their laser characterisation is reported in section 3.2.

The first measurement that is usually taken is the material density. This was estimated by the Archimede's Principle in methanol. Comparing the result obtained with an undoped sample allows a quick measurement of the actual dopant concentration in the sample. Glasses formed with melt and quenching do not suffer from segregation, as crystalline materials do but there is the chance of sedimentation on the melted glass. As an example the density for $Tm_{1.5}$:TZN was 5.4685 g/cm^3.

The active ions concentrations are 1.67·10^{20}, 2.51·10^{20} and 3.35·10^{20} ions/cm^3 for 1.0, 1.5 and 2 wt% increasing concentrations respectively, they are also reported in comparison table 2.2. The room temperature absorption spectra were measured with a Perkin Elmer Lamba 950 UV/VIS spectrophotometer for the three samples and can be seen in Fig 2.9. All graphs have been corrected for Rayleigh and impurities scattering and their baseline is therefore zero.
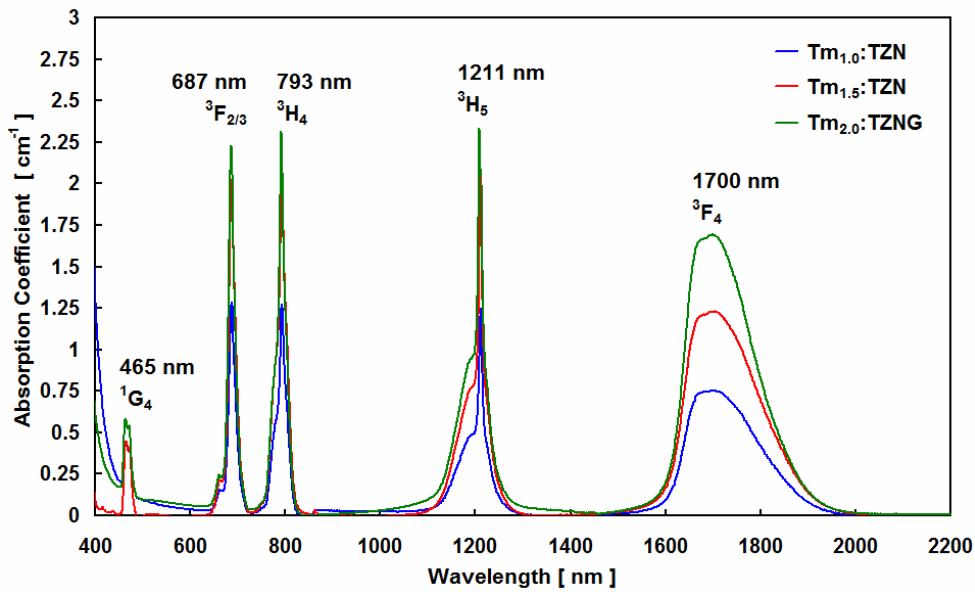

Fig 2.9 The absorption coefficient spectra for the three Tm^{3+} doped tellurite glass samples. Peaks are labeled with the respective transition from ground.

The absorption coefficient spectra are labelled with the respective transition level from ground $^3H_6$ and transition wavelength. Due to inhomogeneous broadening, all spectra are very smooth compared to their crystalline counterparts. Dividing the absorption coefficients spectra by the concentration of Tm^{3+} in ions/cm^3 returns the value for the

absorption cross section σ_A. This is independent of concentration as it is a dopant-host parameter. The absorption cross section is mainly used in the calculation of the emission cross section σ_E for the $^3F_4 \rightarrow {}^3H_6$ transition through the McCumber formula (2.1) and the peak values are reported in table 2.2 at 1700 nm. The luminescence spectra were measured for all samples with an Edinburgh Instruments FLS920 Steady State and Time Resolved Fluorescence Spectrophotometer and an InGaAs detector from 1300 nm to 2200 nm. The excitation source was a laser diode at 808 nm. The luminescence spectra for the $Tm_{1.5}$:TZN and $Tm_{2.0}$:TZNG are shown in Fig 2.10 and they are overlaid on the emission cross section curve for the $Tm_{1.5}$:TZN calculated with the λ_{ZL} and Z_L/Z_U parameters introduced in section 2.3.4. The peak values of the emission cross sections at 1850 nm are shown in table 2.2. The slight disparity (~50 nm) between the calculated and the measured data in Fig 2.10 is most likely due to the choice of parameters Z_L/Z_U and λ_{ZL}.
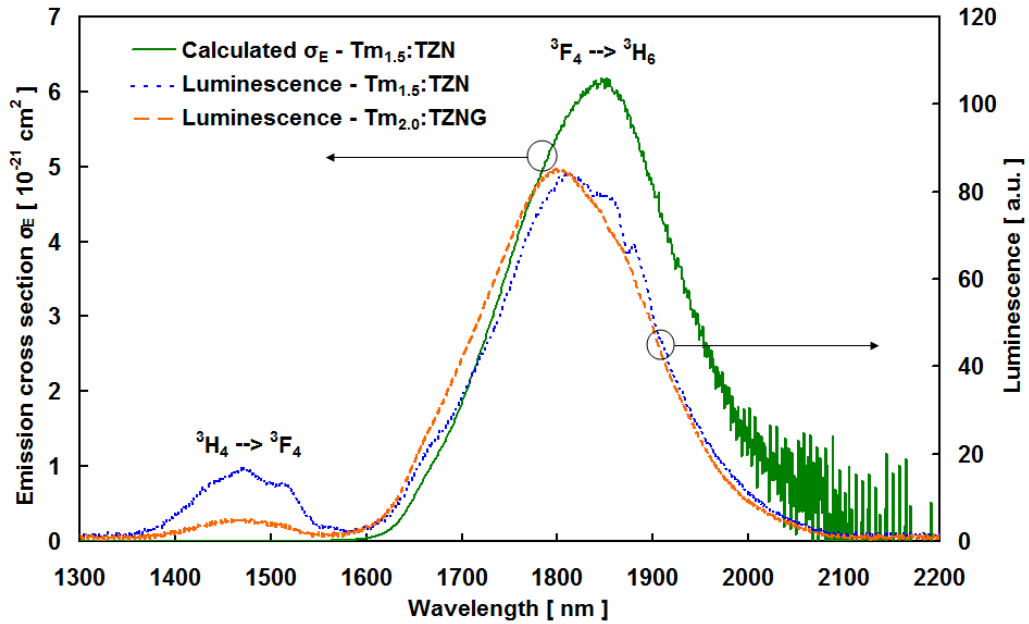

Fig 2.10 The calculated emission cross section for the $Tm_{1.5}$:TZN combination and the luminescence spectra for $Tm_{1.5}$:TZN and $Tm_{2.0}$:TZNG overlaid. Peaks are labelled with the respective transition.

The peak of the $^3H_4 \rightarrow {}^3F_4$ transition in proportion to the peak of the $^3F_4 \rightarrow {}^3H_6$ transition is decreasing with increasing concentration and this effect is due to a more efficient cross-relaxation mechanism[48]. The saturated gain coefficient could be calculated with formula (2.3) and is shown in table 2.2.

The lifetimes τ_F of the $Tm_{1.0}$:TZN for the $^3F_4$ level and for all samples of the $^3H_4$ level were measured at 1800 nm using the Edinburgh Instruments FLS920 spectrometer in time-resolved mode with excitation by a laser diode at 808 nm. All curves obtained had a single exponential decay and that guaranteed a low energy transfer upconversion (ETU), see fig 2.4, and the result are reported in Tab 2.2. Great care was taken in the geometry of the experiments to avoid reabsorption and re-emission effects, however incongruence was found in the data recorded for the $Tm_{1.5}$:TZN and $Tm_{2.0}$:TZNG. In order to analyse in-depth the problem the $^3F_4$ lifetime, measurements were also carried out using the following experimental set-up. Built in collaboration with Dr Robert Thomson at Heriot Watt University, an 808 nm modulated (45 Hz, 50% duty cycle, 10 μs decay time) laser diode output was launched in a multimode silica fiber which was brought into contact with the sample and a small portion of the induced fluorescence from the sample was then collected using the same fiber. The collected signal was then filtered and analysed by a 2 μm detector (New Focus Model 2034). The measured lifetime values were found to be 1.14±0.07 ms for the $Tm_{1.5}$:TZN and 1.30±0.07 ms for the $Tm_{2.0}$:TZNG. Using this experimental configuration ensured that fluorescence was collected directly from the sample region where it was generated by the pump beam thereby reducing the susceptibility of the measurements to reabsorption and re-emission errors. Although increasing dopant concentration might be expected to shorten the upper state lifetimes due to concentration quenching effects, in fact we observed a longer lifetime for the 2 wt% $Tm_{2.0}$:TZNG compared to the 1.5 wt% $Tm_{1.5}$:TZN. We believe that this behaviour was accounted for by the lifetime lengthening effects due to the relative OH^- concentration difference between the TZN and TZNG glasses[51].

Sample codes	Tm^{3+} conc. [wt%]	Tm^{3+} conc. [10^{20} ions/cm^3]	Peak σ_A (1700 nm) [10^{-21} cm^2]	Peak σ_E (1850 nm) [10^{-21} cm^2]	g Saturated Peak Gain per cm [dB/cm]	τ_F ($^3F_4$) [ms]	τ_F ($^3H_4$) [ms]	FOM [10^{-24} s·cm^2]
$Tm_{2.0}$:TZNG	2.0	3.35	5.3	5.3	7.7	1.3	-	6.9
$Tm_{1.5}$:TZN	1.5	2.51	4.9	6.2	6.8	1.14	0.32	7.1
$Tm_{1.0}$:TZN	1.0	1.67	4.5	5.5	4.0	2.85	0.27	15.7

Tab 2.2 The main spectroscopic parameters for the three Tm^{3+} doped samples used in combination with the tellurite networks.

Finally, it is useful to introduce the spectroscopic figure of merit, FOM of the sample as an indication of the likelihood of low threshold operations:

$$FOM = \sigma_E \cdot \tau_F \qquad (2.6)$$

The absorption cross section of the three samples was around $\sim 5 \cdot 10^{-21}$ cm^2 for the three samples and it is interesting to notice how the emission cross section did not change much when adding GeO_2 in the composition as it was found to be around $\sim 5.5 \cdot 10^{-21}$ cm^2 for all Tm^{3+} tellurite samples. The values are similar to the ones reported in literature[48]. Conversely the saturated peak gain is increasing with concentration and has a maximum at 7.7 dB/cm for the 2 wt% doped sample. The lifetime of $^3F_4$, due to concentration quenching decreases from $Tm_{1.0}$:TZN to $Tm_{1.5}$:TZN. Finally the FOM is very high for the $Tm_{1.0}$:TZN and this is due to the long lifetime in the sample and is around $\sim 7 \cdot 10^{-24}$ s·cm^2 for higher Tm^{3+} concentrations.

2.5.2 Tm^{3+}-Ho^{3+} doped tellurite materials

Three doubly doped Tm^{3+}-Ho^{3+} tellurite TZN samples were fabricated and the concentration of Tm^{3+} was independently set from the Ho^{3+} and chosen by two main parameters. Firstly, the successful laser characteristics that were obtained with the 2 wt% Tm^{3+} singly doped $Tm_{2.0}$:TZNG sample described in section 3.2. Secondly the necessary requirement of keeping a short interaction length between pump beam and laser mode beam to obtain maximum mode matching and yet absorbing enough energy to generate gain to overcome the losses in the cavity. On the other hand the Tm^{3+}/Ho^{3+} ratios were specifically chosen in the range of $20 \rightarrow 5$ for two distinct reasons. Firstly because of the lasing characteristics reported by many other authors on crystalline gain media with Tm^{3+} sensitizing of Ho^{3+} ions[66-67]. Secondly because Ho^{3+} ions tend to exhibit high emission cross sections in dielectric laser materials and the concentration needs to be kept necessary low to avoid the green Ho^{3+} upconversion losses[68]. The three samples therefore had a fixed Tm^{3+} concentration of 2 wt% and increasing Ho^{3+} concentrations of 0.1, 0.2 and 0.4 wt% they were named $Tm_{2.0}$-$Ho_{0.1}$:TZN, $Tm_{2.0}$-$Ho_{0.2}$:TZN and $Tm_{2.0}$-$Ho_{0.4}$:TZN respectively. The laser characterisations for these materials are in section 3.3. The absorption coefficient spectra are shown in Fig 2.11, corrected for Rayleigh and impurity scattering.
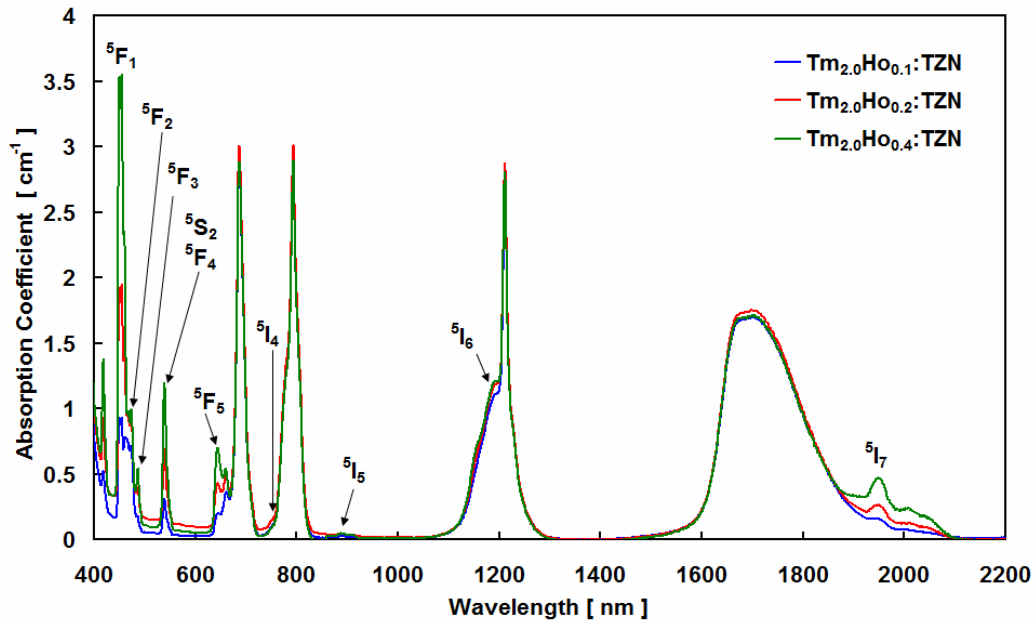
Fig 2.11 The absorption coefficient spectra for the three Tm^{3+}-Ho^{3+} doped tellurite glass samples. Peaks are labelled with the respective Ho^{3+} transitions from ground $^5I_8$.

In the absorption coefficient spectra reported in Fig 2.11 only the Ho^{3+} absorption peaks from ground were highlighted to show their position with respect to the Tm^{3+} ones. Density measurements returned Ho^{3+} dopants concentrations of $0.17 \cdot 10^{20}$, $0.34 \cdot 10^{20}$ and $0.68 \cdot 10^{20}$ ions/cm^3 for 0.1, 0.2 and 0.4 wt% respectively.
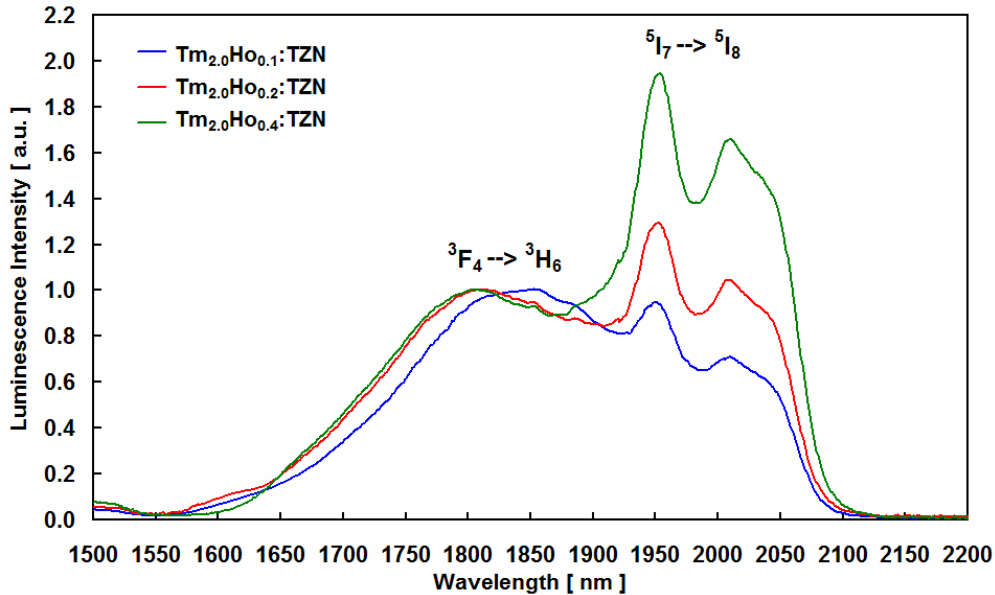

Fig 2.12 The luminescence spectra for the three Tm^{3+}-Ho^{3+} doped tellurite glass samples excited by a laser diode at 808 nm. Peaks are labelled with the respective Tm^{3+} and Ho^{3+} transitions to ground. Graphs are normalized to the Tm^{3+} peak emission around 1800 nm.

The peak absorption cross section at 1945 nm could then be calculated and the values are reported in table 2.3. The absorption coefficient at 1700 nm for the Tm^{3+} is similar to the one obtained for the singly Tm^{3+} doped samples presented in the previous section. The luminescence spectra are shown in fig 2.12 and were measured for the three samples with the same excitation and settings used for the Tm^{3+} doped elements. The values obtained were then normalized to the emission intensity of the Tm^{3+} $^3F_4 \rightarrow {}^3H_6$ transition. It is evident the increase of the relative intensity of Ho^{3+} peaking at 1950 nm and 2010 nm with increasing Ho^{3+} concentration. Higher luminescence does not necessarily implies better laser performance characteristics. In fact many other energy transfer factors contribute to the population inversion of a lasing level. From the absorption cross section and the McCumber theory the emission cross section could be calculated with the parameters relative to the Ho^{3+} ion introduced in section 2.3.4. The emission cross section peaked at 2010 nm and its values are reported in table 2.3 for the three samples. Fig 2.13 reports the absorption and emission cross sections graphs calculated for the $Tm_{2.0}$-$Ho_{0.1}$:TZN.
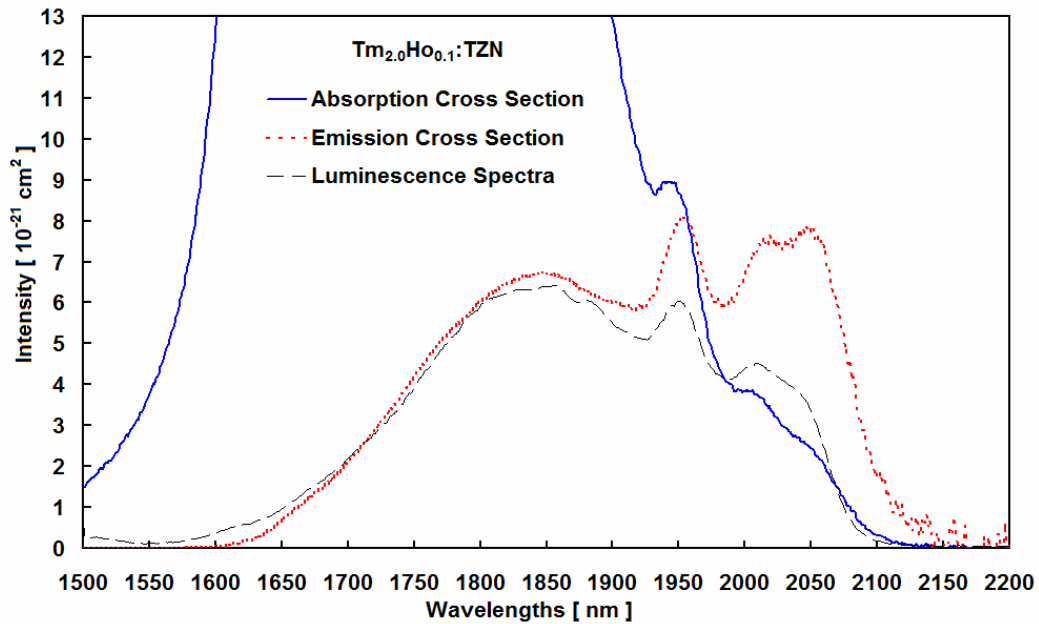

Fig 2.13 The absorption and emission cross sections graphs for the $Tm_{2.0}$-$Ho_{0.1}$:TZN sample. The luminescence spectrum is also overlapped (dashed thin line).

It can be immediately noticed that the calculated emission cross section and the luminescence spectra, from fig 2.12, overlap well. The absorption cross section is calculated for the Ho^{3+} ion with its ions concentration value and of course it overshoots

for typical Tm^{3+} wavelengths below 1950 nm. The saturated peak gain g could then be calculated and it can also be found table 2.3.

The lifetimes of the $^5I_7$ level of Ho^{3+} at 2010 nm and of the $^3F_4$ level of Tm^{3+} at 1800 nm for the three samples were obtained as described above. The curves for the Tm^{3+} had a single exponential decay with t_1 time constants, conversely in the case of the Ho^{3+} all curves showed a doubly exponential decay with time constants t_1 and t_2, all results are summed up in table 2.3. In all samples, there is energy transfer via non-radiative cross relaxation from Tm^{3+} to Ho^{3+} and this is reflected in the observed doubly exponential decays with fast and slow components, where the fast component correspond to the $Tm^{3+} \rightarrow Ho^{3+}$ transfer. On the other hand the probability of back transfer from $Ho^{3+} \rightarrow Tm^{3+}$ increases with decreasing of the mean distances between the two ions. This explains the case of the $Tm_{2.0}$-$Ho_{0.4}$:TZN where a longer lifetime for Tm^{3+} at 1800 nm and Ho^{3+} at 2010 nm is due to intensified forward and backward transfers.

Sample codes	Dopants conc. [wt%]		Tm^{3+}/Ho^{3+} ratio	Ho^{3+} conc.	Peak σ_A (1950 nm)	Peak σ_E (2010 nm)	g Saturated Peak Gain per cm	Tm^{3+} τ_F at 1800 nm [ms]		Ho^{3+} τ_F at 2010 nm [ms]	FOM
	Tm^{3+}	Ho^{3+}	[.]	[10^{20} cm^{-3}]	[10^{-21} cm^2]	[10^{-21} cm^2]	[dB/cm]	t_1	t_2	t_1	[10^{-24} $s \cdot cm^2$]
$Tm_{2.0}$-$Ho_{0.4}$:TZN	2.0	0.4	5	0.68	7.9	7.8	2.3	3.08	0.61	3.2	25.0
$Tm_{2.0}$-$Ho_{0.2}$:TZN	2.0	0.2	10	0.34	7.6	7.4	1.1	2.09	0.66	2.35	17.4
$Tm_{2.0}$-$Ho_{0.1}$:TZN	2.0	0.1	20	0.17	8.9	7.5	0.6	2.04	0.67	2.57	19.3

Tab 2.3 The main spectroscopic parameters for the three Tm^{3+}-Ho^{3+} doped samples used in TZN tellurite glass.

The peak emission cross section at the lasing level was around $\sim 7.5 \cdot 10^{-21}$ cm^2 for the Tm^{3+}-Ho^{3+} doped glasses and the value is slightly higher in comparison with the Tm^{3+} singly doped ones. Even in presence of an higher emission cross section, the combination with a small inverted population of course generates low gains, as low as 0.6 dB/cm for the $Tm_{2.0}$-$Ho_{0.1}$:TZN sample. In the case of Tm^{3+}-Ho^{3+} excitation gain alone does not fully describe the capabilities of the material since upconversion losses play a great part in them as explained in section 3.3.3. Long lifetimes contribute to bigger FOMs that give for these materials values twice as much the ones obtained for the Tm^{3+} samples.

2.5.3 Tm^{3+} doped fluorogermanate materials

One fluorogermanate Tm^{3+} doped sample was produced and its sample code is Tm^{3+}:GPNG. Laser characterisation was carried out and reported in depth in section 3.4. In this section the spectroscopic investigation is presented. Density measurements returned an ion concentration of $3.1 \cdot 10^{20}$ ions/cm^3. The absorption coefficient spectrum is shown in Fig 2.14, corrected for Rayleigh and impurities scattering. Tm^{3+} ions in this fluorogermanate network have a peak absorption cross section at 1700 nm similar to the one found for the tellurite glasses. Luminescence measurements were also performed in this glass under the usual 808 nm laser diode excitation and the results are reported in Fig 2.15 where the spectrum is overlapped with the emission cross section spectrum calculated with the McCumber theory.
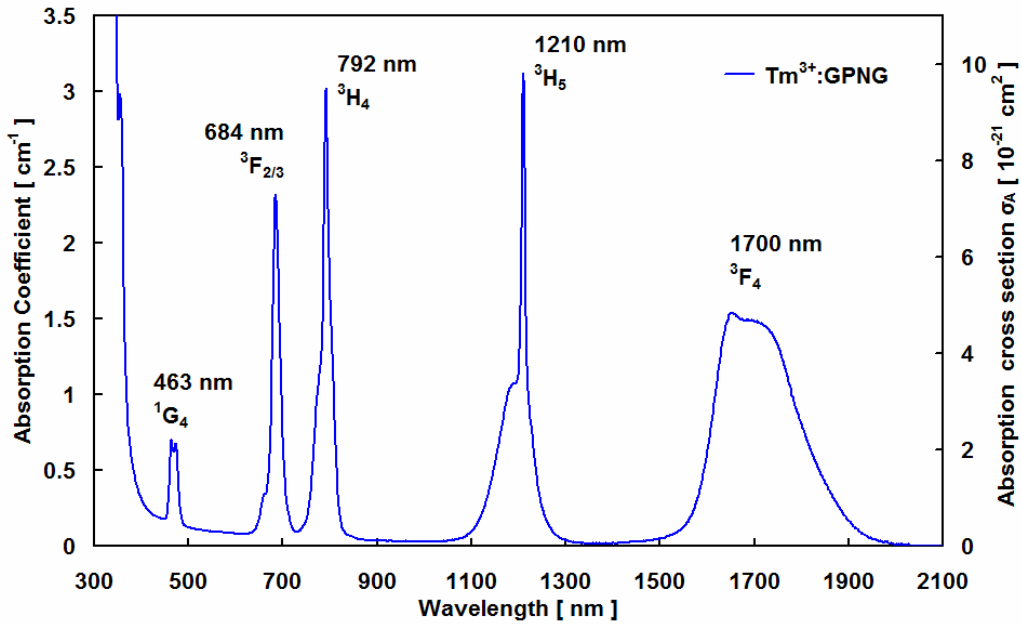

Fig 2.14 The absorption coefficient spectra for the Tm^{3+}:GPNG fluorogermanate glass. The spectrum was corrected for Rayleigh and impurities scattering. Peaks are labelled with the respective transition from ground.

The two spectra in Fig 2.15 overlap very well and it is interesting to notice that there is a significant emission peak at 1470 nm which would suggest that there is still room to increase the concentration of dopants and therefore enjoy a higher cross-relaxation efficiency in this sample. The emission cross section peaks at $5.6 \cdot 10^{-21}$ cm^2 and once again has similar values to the ones previously reported in the TZN samples. The saturated peak gain could then be calculated and was 7.5 dB/cm.
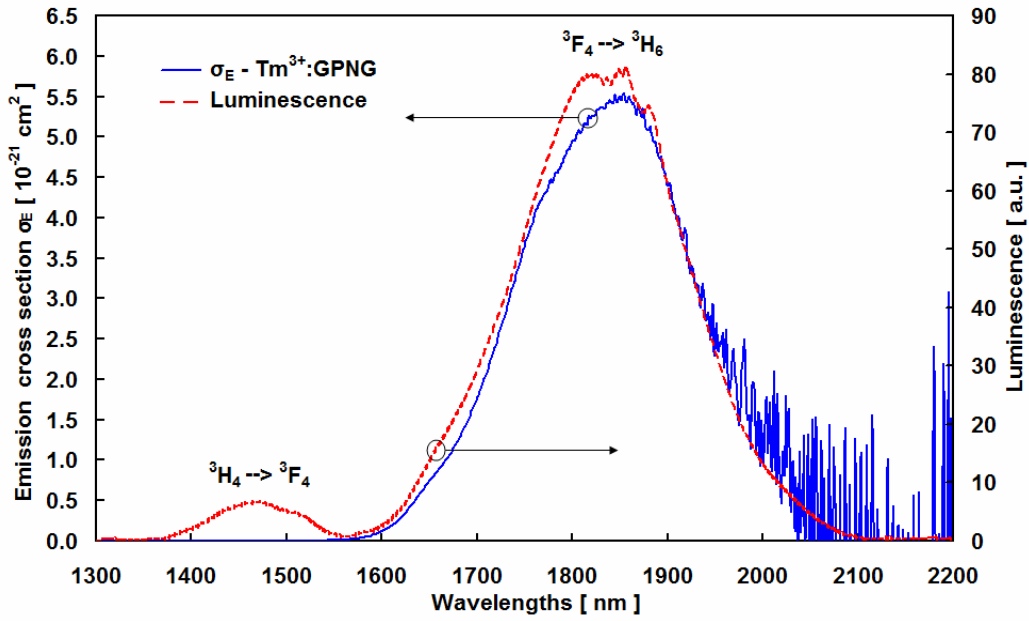
Fig 2.15 The luminescence and the emission cross section spectra for the Tm^{3+}:GPNG fluorogermanate glass. Peaks are labelled with their transition to ground.

The lifetime of the lasing level was also measured with the time resolved spectrophotometer and it showed a single exponential decay with constant of 2.9 ms which indicated a negligible energy transfer upconversion ($^3F_4 + {}^3F_4 \rightarrow {}^3H_6 + {}^3H_4$). The FOM was $16.2 \cdot 10^{-24}$ s·cm². A full comparison of the main spectroscopic parameters among Tm^{3+} doped glass samples is reported in section 2.6.

2.5.4 Tm^{3+} doped ZBLAN fluoride materials

The fluoride sample chosen was a ZBLAN type and its manufacture was described in section 2.4.3. The sample, coded Tm^{3+}:ZBLAN, was doped with 2 mol% Tm^{3+} and the ions concentration was calculated via density measurements at $3.56 \cdot 10^{20}$ ions/cm³. The ZBLAN has been extensively used and reported in literature, it is therefore useful to briefly present here the key parameters measured for the sample in use in this PhD. From the absorption coefficient measurements the absorption cross section peak at 1660 nm was of $2.7 \cdot 10^{-21}$ cm² as can be seen from the graph in fig 2.16. While the absorption coefficient reported so far for other samples were all corrected for Rayleigh and impurities scattering by removing the pedestal, it should be noted that the graph in fig 2.16 has been reported as measured and the pedestal is nearly zero proving the outstanding optical quality of the sample used in the experiments.
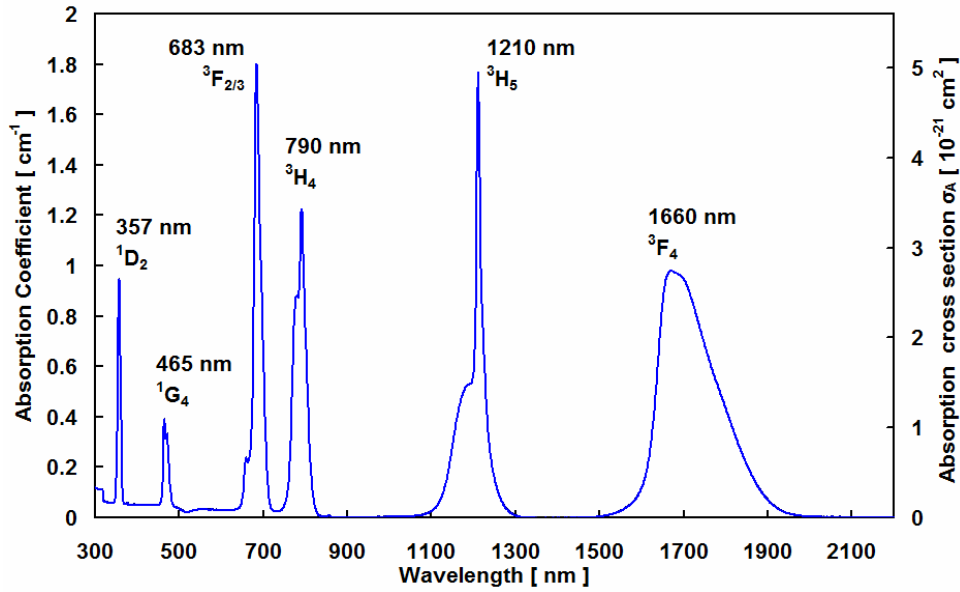
Fig 2.16 The absorption coefficient spectra for the Tm^{3+}:ZBLAN fluoride glass. The spectrum was not corrected for Rayleigh and impurities scattering. Peaks are labelled with the respective transition and wavelengths from ground.

It is also interesting to see that the wider transparency range of the fluoride glass allows the detection of the absorption from the $^1D_2$ level at 357 nm. Absorption peaks happens at higher energies than the ones recorded for the fluorogermanate glasses due to the ionic character of the fluoride network former. The McCumber theory applied to the absorption cross section returned a peak emission cross section of $2.5 \cdot 10^{-21}$ cm^2 at 1825 nm and this value is in agreement with the one reported in literature for the same type of glass[17]. The saturated peak gain is approximately 3.9 dB/cm. The lifetime was measured with the spectrophotometer and the 808 nm laser diode, the decay was single exponential with a constant of 4.6 ms. Longer lifetimes are expected for lower phonon energy samples and this in turn yielded a FOM of $11.5 \cdot 10^{-24}$ $s \cdot cm^2$.

2.6 Spectroscopic comparisons of Tm^{3+} doped active materials

In section 2.5 the spectroscopical investigation of the glasses used in this research project were carried out for singly Tm^{3+} and doubly Tm^{3+}-Ho^{3+} doped samples. Leaving out the Ho^{3+} emitting materials, it is interesting to compare the characteristics of the Tm^{3+} doped ones in different hosts. Table 2.4 below sums up the mechanical and

spectroscopical characteristics of three samples: $Tm_{2.0}$:TZNG, Tm^{3+}:GPNG and Tm^{3+}:ZBLAN.

Sample codes	Tm^{3+} conc. [10^{20} ions/cm^3]	Peak Phonon Energy ħω [cm^{-1}]	Abbe Number [.]	n_2 [10^{-15} cm^2/W]	2nd order dispersion at 2 μm [fs^2/mm]	Peak σ_E (1850 nm) [10^{-21} cm^2]	g Saturated Peak Gain per cm [dB/cm]	τ_F ($^3F_4$) [ms]	FOM [10^{-24} s·cm^2]
$Tm_{2.0}$:TZNG	3.35	790	18	5.74	70	5.3	7.7	1.3	6.9
Tm^{3+}:GPNG	3.10	890	42	9.5	280	5.6	7.5	2.9	16.2
Tm^{3+}:ZBLAN	3.56	500	70	0.24	-15	2.5	3.9	4.6	11.5

Tab 2.4 The mechanical and spectroscopic parameters for the three Tm^{3+} doped glass different glassy hosts as they were presented in the text.

The characteristics of the three samples compared in table 2.4 all fall within expected behaviour for the different hosts. The peak phonon energy is maximum for the fluorogermanate sample that also exhibits a very high nonlinear refractive index compared to the other two specimens. The GPNG sample also maintains an emission cross section and a saturated peak gain comparable to the one in TZNG, which was expected for high refractive index glasses. The figure of merits FOMs of the three samples are mostly connected to the lasing threshold values and such values are consequently found to be smaller for higher FOM as described in Chapter 3. In the case of the lifetimes it was expected that samples with higher phonon energies would return short lifetimes due to the high multi-phonon relaxation rates. Nevertheless in the case of the fluorogermanate glass the lifetime of the lasing level is longer than the one found in the tellurite sample. This may be due to the low energy lead fluoride local environment that the Tm^{3+} ions interact with in the GPNG sample.

2.7 Conclusions

In this chapter the basics of glassy amorphous materials used for laser generation have been introduced. The physics of the glass formation and the *melt and quenching* technique used in this PhD for manufacturing of the glass samples were also described. After a brief introduction on the typical glasses used in the state of the art of solid state glass lasers, the mechanical properties of glasses were also reported.. In section 2.3 the interactions that take place between the two forming elements were investigated in depth. The basic concepts of the trivalent *rare earths ions* as active ions were described

along with their mechanical interaction with the host environment and their electronic interactions with the electric fields of the glassy networks. The relative influence that the electrical and the mechanical factors have on the spontaneous emission of the active ions can also be found at the end of section 2.3. In order to better explain the nano-structural features of the glasses, the results of the Raman spectra were reported for the Tellurite glasses and for the Fluorogermanate glasses compounds used for the research project and the results were described in section 2.4. Most importantly the spectroscopical performance characterisation were carried out for the Tellurite, Fluorogermanate and Fluoride glasses doped with Tm^{3+} or Tm^{3+}-Ho^{3+} combinations in section 2.5. Finally it is important to underline the necessity of spectroscopical investigation on potential laser elements as a fundamental step prior to the commitment to laser characterisations. The investigations described in this chapter underpin the development of all this research project and they are used in the next chapters: Chapter 3 and Chapter 4 where the continuous wave laser characterisations are presented.

2.8 References

[1]   K. Hirao*, et al.*, *Active Glass for Photonics Devices* **1**. Berlin Heidelberg New York: Springer-Verlag, 2000, Isbn: 3540410651.

[2]   J. E. Shelby and Royal Society of Chemistry (Great Britain), *Introduction to glass science and technology*, 2nd ed. Cambridge: Royal Society of Chemistry, 2005, Isbn: 9781847551160.

[3]   ASTM-Committee, "*ASTM Standard on Glass and Glass products*", **C14**, pp. - (April 1995).

[4]   W. H. Zachariasen, "*The Atomic Arrangement in Glass*", Journal of the American Chemical Society, **54**, pp. 3841-3851, (1932).

[5]   K. Pátek and J. G. Edwards, *Glass lasers*. London: Iliffe, 1970, Isbn: 0592027783.

[6]   J. E. Stanworth, *Physical properties of glass*. Oxford: Clarendon Press, 1950, Isbn:

[7]   http://www.sciglass.info/.

[8]   L. Le Neindre, *et al.*, "*Effect of relative alkali content on absorption linewidth in erbium-doped tellurite glasses*", Journal of Non-Crystalline Solids, **255**, pp. 97-102, (1999).

[9]   E. Snitzer, "*Optical Maser Action of Nd^{3+} in a Barium Crown Glass*", Physical Review Letters, **7**, p. 444, (1961).

[10]   A. Kermaoui and F. Pelle, "*Synthesis and infrared spectroscopic properties of Tm^{3+}-doped phosphate glasses*", Journal of Alloys and Compounds, **469**, pp. 601-608, (2009).

[11]   K. Annapurna, *et al.*, "*Spectral analysis of thulium doped zinc-boro-silicate glass*", Physica B-Condensed Matter, **388**, pp. 174-179, (2007).

[12]   B. M. Walsh, *et al.*, "*Optical properties of Tm^{3+} ions in alkali germanate glass*", Journal of Non-Crystalline Solids, **352**, pp. 5344-5352, (2006).

[13]   Q. F. Lin, *et al.*, "*Gain properties of germanate glasses singly doped with Tm^{3+} and Ho^{3+} ions*", Journal of Rare Earths, **27**, pp. 76-82, (2009).

[14]   L. D. da Vila, *et al.*, "*Time resolved luminescence in (Tm : Ho) doped tellurite glass*", Optical Materials, **27**, pp. 1333-1339, (2005).

[15]   G. Ozen, *et al.*, "*Thermal and optical properties of Tm^{3+} doped tellurite glasses*", Spectrochimica Acta Part a-Molecular and Biomolecular Spectroscopy, **57**, pp. 273-280, (2001).

[16]   C. K. Jayasankar and A. Renuka Devi, "*Optical properties of Tm^{3+} ions in lithium borate glasses*", Optical Materials, **6**, pp. 185-201, (1996).

[17]   J. L. Doualan, *et al.*, "*Spectroscopic properties and laser emission of Tm doped ZBLAN glass at 1.8 μm*", Optical Materials, **24**, pp. 563-574, (2003).

[18]   B. Dussardier, *et al.*, "*Spectroscopy and CW 2-Photon up-Conversion in Tm^{3+}-Doped $ZnCl_2$-Based Glass*", Optical Materials, **4**, pp. 565-573, (1995).

[19]   M. Yamane and Y. Asahara, *Glasses For Photonics*: Cambridge University Press, 2007, Isbn: 0-521-58053-6.

[20]   Y. S. Han, *et al.*, "*Cross relaxation mechanism among Tm^{3+} ions in $Ge_{30}Ga_2As_6S_{62}$ glass*", Journal of Non-Crystalline Solids, **316**, pp. 302-308, (2003).

[21]   J. H. Song, *et al.*, "*Emission properties and local structure of Tm^{3+} in Ge-Ga-S-Br glass*", Journal of Non-Crystalline Solids, **353**, pp. 1676-1680, (2007).

[22] M. P. Shepilov, "*On light scattering in fluorozirconate glass-ceramics containing BaCl₂ nano-crystals*", Optical Materials, **30**, pp. 839-846, (2008).

[23] F. Urbach, "*The Long-Wavelength Edge of Photographic Sensitivity and of the Electronic Absorption of Solids*", Physical Review, **92**, p. 1324, (1953).

[24] A. J. Kenyon, "*Recent developments in rare-earth doped materials for optoelectronics*", Progress in Quantum Electronics, **26**, pp. 225-284, (2002).

[25] J. Wang*, et al.*, "*Local structures of rare-earth ions in glasses: the [`]crystal-chemistry' approach*", Journal of Non-Crystalline Solids, **163**, pp. 261-267, (1993).

[26] M. G. Mayer, "*Rare-Earth and Transuranic Elements*", Physical Review, **60**, p. 184, (1941).

[27] G. H. Dieke and H. M. Crosswhite, "*The Spectra of the Doubly and Triply Ionized Rare Earths*", Applied Optics, **2**, pp. 675-686, (1963).

[28] M. J. Weber, "*Science and technology of laser glass*", Journal of Non-Crystalline Solids, **123**, pp. 208 - 222, (1990).

[29] M. D. Shinn*, et al.*, "*Optical transitions of Er3+ ions in fluorozirconate glass*", Physical Review B, **27**, p. 6635, (1983).

[30] L. A. Riseberg and M. J. Weber, "III Relaxation Phenomena in Rare-Earth Luminescence," in *Progress in Optics*. vol. Volume 14, E. Wolf, Ed., ed: Elsevier, 1977, pp. 89-159.

[31] X. Zou and H. Toratani, "*Spectroscopic properties and energy transfers in Tm3+ singly- and Tm3+/Ho3+ doubly-doped glasses*", Journal of Non-Crystalline Solids, **195**, pp. 113-124, (1996).

[32] R. Balda*, et al.*, "*Spectroscopy and concentration quenching of the infrared emissions in Tm3+-doped TeO2-TiO2-Nb2O5 glass*", Optics Express, **15**, pp. 6750-6761, (2007).

[33] F. Auzel*, et al.*, "*Radiation trapping and self-quenching analysis in Yb3+, Er3+, and Ho3+ doped Y2O3*", Optical Materials, **24**, pp. 103-109.

[34] M. Yokota and O. Tanimoto, "*Effects of Diffusion on Energy Transfer by Resonance*", Journal of the Physical Society of Japan, **22**, p. 779, (1966).

[35] A. I. Brushteĭn, "*Hopping Mechanism of Energy Transfer*", Soviet Journal of Experimental and Theoretical Physics, **35**, p. 882, (1972).

[36] M. Inokuti and F. Hirayama, "*Influence of Energy Transfer by the Exchange Mechanism on Donor Luminescence*", The Journal of Chemical Physics, **43**, pp. 1978-1989, (1965).

[37] S. Rai and S. Hazarika, "*Fluorescence dynamics of Tb3+ and Tb3+/Ho3+ doped phosphate glasses*", Optical Materials, **30**, pp. 1343-1348, (2008).

[38] S. A. Payne*, et al.*, "*Infrared Cross-Section Measurements for Crystals Doped with Er^{3+}, Tm^{3+}, and Ho^{3+}*", IEEE Journal of Quantum Electronics, **28**, pp. 2619-2630, (1992).

[39] D. E. McCumber, "*Einstein relations connecting broadband emission and absorption spectra.*", Physical Review B, **136**, pp. 954 - 957, (1964).

[40] B. R. Judd, "*Optical Absorption Intensities of Rare-Earth Ions*", Physical Review, **127**, p. 750, (1962).

[41] G. S. Ofelt, "*Intensities of Crystal Spectra of Rare-Earth Ions*", The Journal of Chemical Physics, **37**, pp. 511-520, (1962).

[42] A. M. Guénault, *Statistical physics*, 2nd rev. and enl. ed. Dordrecht ; London: Springer, 2007, Isbn: 9781402059742 (pbk.).

[43] A. J. Bayramian*, et al.*, "*Gain saturation measurements of ytterbium-doped Sr-5(PO4)(3)F*", Applied Optics, **39**, pp. 982-985, (2000).

[44] J. J. Berzelius, "*Untersuchung über die Eigenschaften des Tellurs*", Annalen der Physik - Wiley, **108**, pp. 577-666, (1834).

[45] R. A. H. El-Mallawany, *Tellurite Glasses Handbook: Physical Properties and Data* CRC, 2001, Isbn: 0849303680.

[46] L. Huang*, et al.*, "*Visible emissions at 592 and 613 nm in Er3+-Eu3+-codoped tellurite fibers*", Optics Communications, **239**, pp. 403-408, (2004).

[47] J. S. Wang*, et al.*, "*Tellurite Glass : A new candidate for fiber devices*", Optical Materials, **3**, pp. 187-203, (1994).

[48] H. Gebavi*, et al.*, "*Spectroscopic investigation and optical characterization of novel highly thulium doped tellurite glasses*", Journal of Non-Crystalline Solids, **355**, pp. 548-555, (2009).

[49] C. J. Hill and A. Jha, "*Development of novel ternary tellurite glasses for high temperature fiber optic mid-IR chemical sensing*", Journal of Non-Crystalline Solids, **353**, pp. 1372-1376, (2007).

[50] J. C. McLaughlin, *et al.*, "*The Structure of Alkali Tellurite Glasses*", The Journal of Physical Chemistry B, **105**, pp. 67-75, (2000).

[51] A. Jha, *et al.*, "*Structural origin of spectral broadening of 1.5-mum emission in Er3+-doped tellurite glasses*", Physical Review B, **62**, p. 6215, (2000).

[52] S. Hazarika and S. Rai, "*Structural, optical and non-linear investigation of Eu3+ ions in sol-gel silicate glass*", Optical Materials, **27**, pp. 173-179, (2004).

[53] R. Adair, *et al.*, "*Nonlinear refractive-index measurements of glasses using three-wave frequency mixing*", J. Opt. Soc. Am. B, **4**, pp. 875-881, (1987).

[54] M. E. Lines, "*A possible non-halide route to ultralow loss glasses*", Journal of Non-Crystalline Solids, **103**, pp. 279-288, (1988).

[55] X. Jiang, *et al.*, "*Investigation on germanium oxide-based glasses for infrared optical fibre development*", Optical Materials, **31**, pp. 1701-1706 (2009).

[56] J. E. Shelby and E. A. Bolden, "*Formation and Properties of Lead Fluorogermanate Glasses*", Journal of Non-Crystalline Solids, **142**, pp. 269-277, (1992).

[57] G. S. Henderson, "*The Germanate Anomaly: What do we know?*", Journal of Non-Crystalline Solids, **353**, pp. 1695-1704, (2007).

[58] S. Todoroki, *et al.*, "*Local-Structure around Rare-Earth Ions in Indium-Based and Lead-Based Fluoride Glasses with High up-Conversion Efficiency*", Journal of Non-Crystalline Solids, **143**, pp. 46-51, (1992).

[59] H. T. Sun, *et al.*, "*Structural and up-conversion luminescence properties in Tm (3+)/Yb3+-codoped heavy metal oxide-halide glasses*", Spectrochimica Acta Part a-Molecular and Biomolecular Spectroscopy, **63**, pp. 149-153, (2006).

[60] P. Thangadurai, *et al.*, "*Raman studies in nanocrystalline lead (II) fluoride* ", Journal of Physics: Condensed Matter, **17**, p. 863, (2005).

[61] J. F. Scott, "*Raman Spectra of GeO2*", Physical Review B, **1**, p. 3488, (1970).

[62] J. McDougall, *et al.*, "*Judd Ofelt parameters of rare-earth ions in ZBLALI, ZBLAN, and ZBLAK fluoride glass*", Physics and Chemistry of Glasses, **35**, pp. 258-259, (1994).

[63] X. Zhu and N. Peyghambarian, "*High-Power ZBLAN Glass Fiber Lasers: Review and Prospect*", Advances in OptoElectronics, **2010**, p. 501956, (2010).

[64] J. M. Parker, "*Fluoride Glasses*", Annual Review of Materials Science, **19**, pp. 21-41, (1989).

[65] F. X. Gan, "*Optical-Properties of Fluoride Glasses - a Review*", Journal of Non-Crystalline Solids, **184**, pp. 9-20, (1995).

[66] K. Scholle*, et al.*, "*Single mode tm and Tm,Ho : LuAG lasers for LIDAR applications*", Laser Physics Letters, **1**, pp. 285-290, (2004).

[67] E. Sani*, et al.*, "*Comparative analysis of Tm-Ho : KYF4 laser crystals*", Applied Physics B-Lasers and Optics, **81**, pp. 847-851, (2005).

[68] A. K. Singh*, et al.*, "*Up-conversions in Ho3+ doped tellurite glass*", Journal of Alloys and Compounds, **403**, pp. 97-103, (2005).

3. BULK GLASS CONTINUOUS WAVE 2 μm LASERS PUMPED AT 800 nm

3.1 Chapter Synopsis

This chapter presents results obtained on the continuous wave laser performance characteristics obtained from Tm^{3+} and Tm^{3+}-Ho^{3+} doped Tellurite, Fluorogermanate and Fluoride glass lasers $^3H_4$ pumped by 800 nm Ti:Sapphire laser system.

Tellurite glass samples were prepared at the University of Leeds in the laboratories of the Institute of Material Research under the supervision and collaboration of Dr Gin Jose and Prof Animesh Jha. Many different dopants concentration and combinations were spectroscopically investigated as described in chapter 2 and laser behaviour was achieved for three Tm^{3+} and three Tm^{3+}-Ho^{3+} doped samples which respective performance characteristics are presented in section 3.2 and section 3.3 respectively.

Drawing from the experience and results gained from the Tm^{3+}:Tellurite samples, a new class of samples based on the fluorogermanate network former was designed at the University of Leeds, Tm^{3+}:GPNG. The fabrication and spectroscopy characterization of the samples were previously discussed in chapter 2 and laser results are presented in section 3.4.

In order to compare and evaluate the performance characteristics, many fluoride ZBLAN samples provided by Dr D. Hollis from the University of West Scotland were also investigated. The 2 mol% Tm^{3+} doped ZBLAN was selected for lasing experiments the results are discussed in Section 3.5. Concluding remarks and a comparison of the laser performance characteristics across host type are presented in Section 3.6.

3.2 Tm^{3+} Tellurite Glasses

3.2.1 Introduction and samples description

In Tm^{3+}:TZN and Tm^{3+}:TZNG glass samples threshold was reached and laser characteristics could be measured around a central lasing wavelength of 1950 nm. Table 3.1 reports the detailed list of lasing glass samples with sizes, geometries and dopant concentrations.

Sample codes	A [mm]	B [mm]	Tm^{3+} concentrations [wt%]	Host
$Tm_{2.0}$:TZNG	5	3	2.0	TZNG
$Tm_{1.5}$:TZN	7	4	1.5	TZN
$Tm_{1.0}$:TZN	10.3	-	1.0	TZN

Tab 3.1 An overview of the dimensions and concentrations of the tellurite based samples where laser characteristics performances were recorded. Subscripts on the sample codes are related to the Tm^{3+} concentrations.

After spectroscopic characterisation, reported in section 2.5, samples were cut and polished according to concentration and the absorption coefficient at the pumping wavelength. The lengths of the active materials were designed so that absorptions of the pump radiation in excess of 70 % were possible without compromising laser characteristics. However for low concentrations and therefore a long interaction of pump and mode active volumes, as in the 1 wt%-doped $Tm_{1.0}$:TZN, the resulting thermal lensing proved to be detrimental.

3.2.2 Continuous wave laser performance characterizations

The 2.0 wt% doped $Tm_{2.0}$:TZNG was Brewster cut to a length of 5 mm so that 75% of the incident power was absorbed. The Ti:Sapphire pump beam, tuned to the peak of the $^3H_4$ transition at 793 nm, was focused with a 63 mm focal-length lens and after the folding mirror M1 produced a 33 µm beam spot size radius measured with a beam-profiler. The glass was wrapped in indium foil, kept at 15 °C by the thermo-electric cooler (TEC) and inserted in an asymmetric Z-folded cavity as shown in Fig. 3.1. The laser resonator allowed a stable mode beam spot radius of 30 µm according to the paraxial approximation.
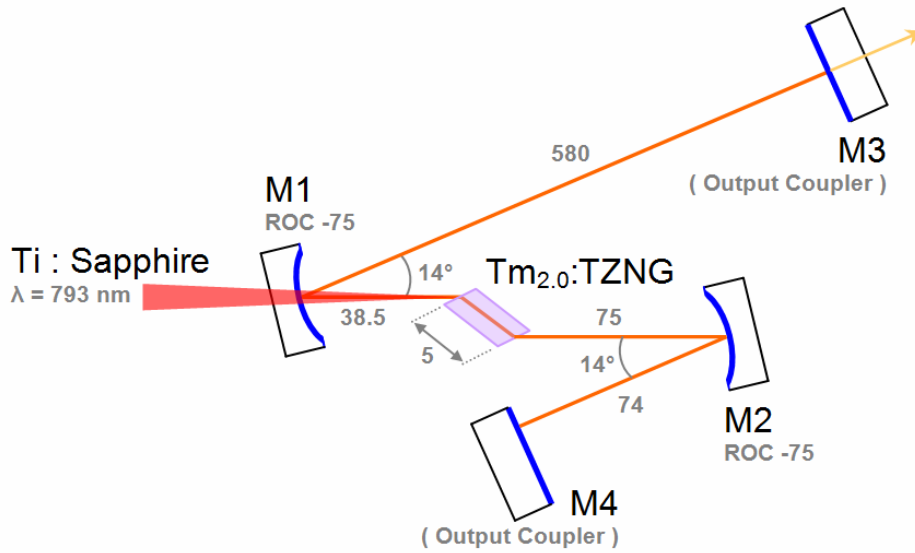
Fig 3.1 The Z-folded laser resonator used for the $Tm_{2.0}$:TZNG sample. All distances are reported in millimetres. The mode beam spot radius at the active material was calculated to be 30 µm.

The absorbed to output power characteristics were recorded for the four different output couplers OC, and are presented in Fig 3.2. The lowest lasing threshold was measured at 134 mW of incident power with the 0.8% OC. A combined output coupling of 6.1 % could also be achieved by employing simultaneously both the 4.1 % and 2.0 % OCs in place of cavity mirrors M3 and M4, Fig. 3.1. The maximum output power obtained was of 124 mW with the 6.1 % OC at a free running wavelength of 1932 nm. The efficiency of the laser was 11.9%, 19.6%, 25.6% and 28.4% using the 0.8%, 2.0%, 4.1% and 6.1% output couplers respectively[1]. In order to characterise the laser system and provide a quantitative comparison term, from the different output efficiencies at different output couplers an estimation of the loss present on the material can be provided.

The formula that links the efficiency with the losses reported in the work of Caird et al[2]:

$$\eta(T) = \eta_0 \cdot \frac{T}{T + \delta} \qquad (3.1)$$

where δ are the total roundtrip losses in the system, T is the transmission of the output couplers and independent variable, η(T) and η_0 are the slope efficiency and the maximum attainable slope efficiency respectively. The latter can be defined as:

$$\eta_0 = \eta_Q \cdot \frac{\lambda_P}{\lambda_L} \qquad (3.2)$$

where the ratio λ_P/λ_L is the maximum theoretical efficiency (~40 %) also called quantum limit and η_Q is the quantum efficiency or quantum yield. Formula (3.1) is very useful and has been used throughout as it can be written in the following way:

$$\frac{1}{\eta(T)} = \frac{1}{\eta_0} + \frac{\delta}{\eta_0}\left(\frac{1}{T}\right) \qquad (3.3)$$

By plotting the inverse of the slope efficiencies measured for the laser against the inverse of the output coupler transmissivities it is possible to give an accurate estimation of the losses in the system and ultimately of the quantum efficiency. In section 3.2.3 the value of η_Q found with (3.2) is explained in relation to our laser systems and its spectroscopical definition.
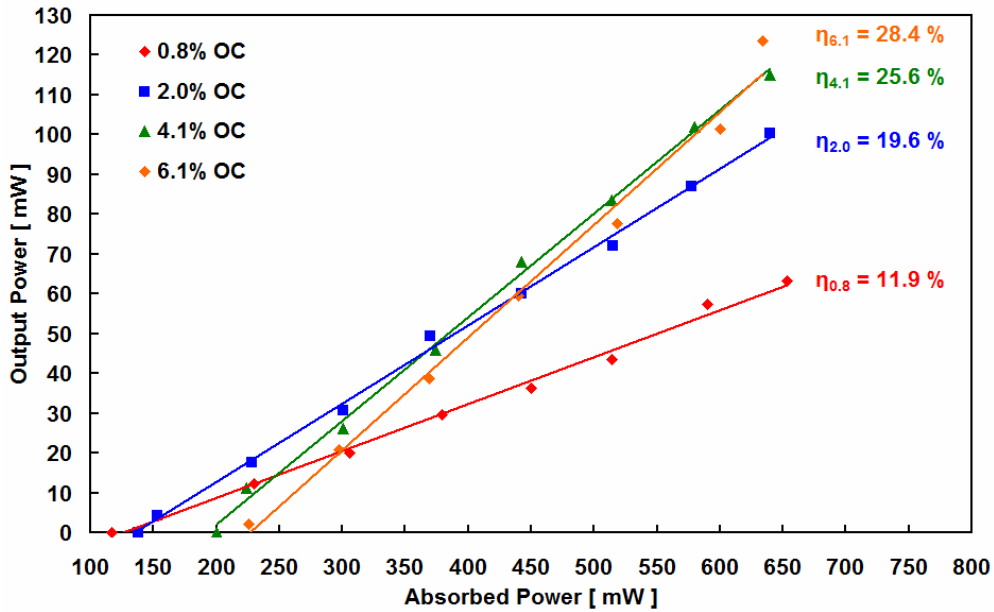
Fig 3.2 The absorbed to output power slope efficiency curves of the tellurite sample $Tm_{2.0}$:TZNG doped at 2.0 wt% for four different output couplers when pumped at 793 nm.

From the data shown in Fig 3.3, we can infer an $\eta_0 = 35\%$ and $\delta = 1.5\%$. If we take into account the 0.1% losses per each mirror M1, M2 and M4 and the 0.2% roundtrip losses due to the residual reflections at the surfaces of the active element inserted at Brewster's angle we obtain final losses of approximately 1%. The number is usually reported per cm of gain material therefore: $\delta_{Tm2.0:TZNG} = 2 \pm 0.2\ \%/cm$.
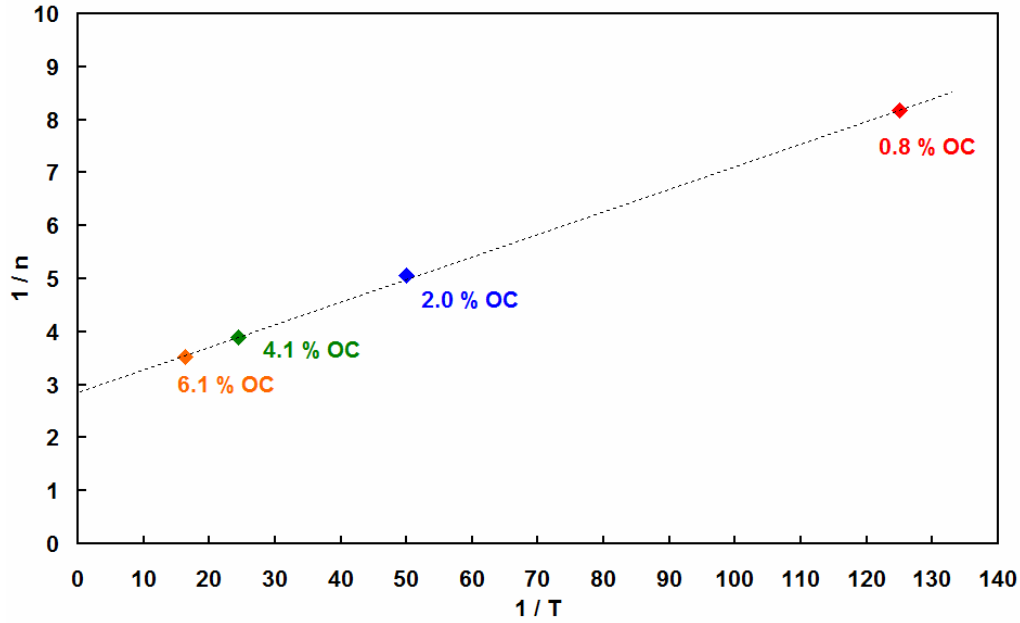

Fig 3.3 The inverse of the slope efficiencies of Fig 3.2 plotted versus the inverse of the output coupler transmissivities for the 2 wt% $Tm_{2.0}$:TZNG sample, the results stand on a straight line.

The error reported is estimated by assuming an experimental variation of 2% on the values of the efficiencies measured. From η_0 and formula (3.2) we can infer an approximate value for the quantum efficiency of $\eta_Q = 87\%$. Losses and quantum efficiencies are compared at the end of this section for all samples tested.

The laser tunability was assessed by inserting in the laser cavity an infrared-grade fused silica prism at the minimum deviation angle and by tilting the output coupling mirror. The data obtained were normalized and are depicted in Fig. 3.4 for three output couplers. The full width at half maximum FWHM values for the 0.8% OC, the 2.0% OC and the 4.1% OC were 135 nm, 125 nm and 100 nm respectively. The emission peaked at 1950 nm centre wavelength and was continuously tuneable throughout the output spectrum.
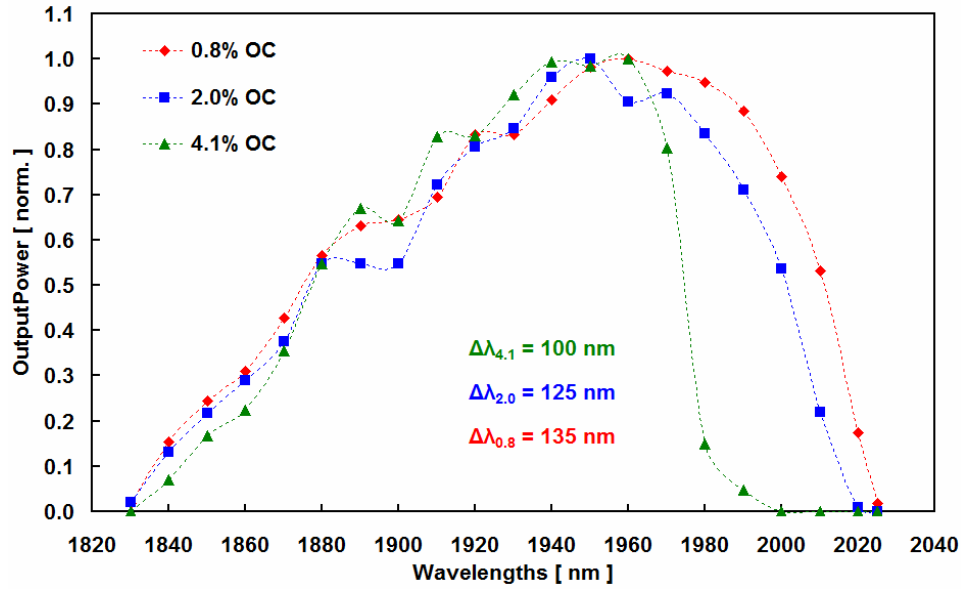
Fig 3.4 The laser tunability of the tellurite sample $Tm_{2.0}$:TZNG doped at 2.0 wt% for three different output couplers measured with the insertion of a fused silica prism in the cavity. The FWHM of the curves are reported in the picture.

The 1.5 wt% Tm^{3+}-doped $Tm_{1.5}$:TZN was Brewster cut to a length of 7 mm and 80% of the incident power tuned at the peak of the $^3H_4$ transition at 793 nm was absorbed. Once again the Ti:Sapphire pump beam was focused with the same 63 mm focal-length lens and the element was deployed in a similar type of Z-folded resonator configuration. Distances between optical elements in resonators of the two systems changed slightly as a result of cavity optimisation.
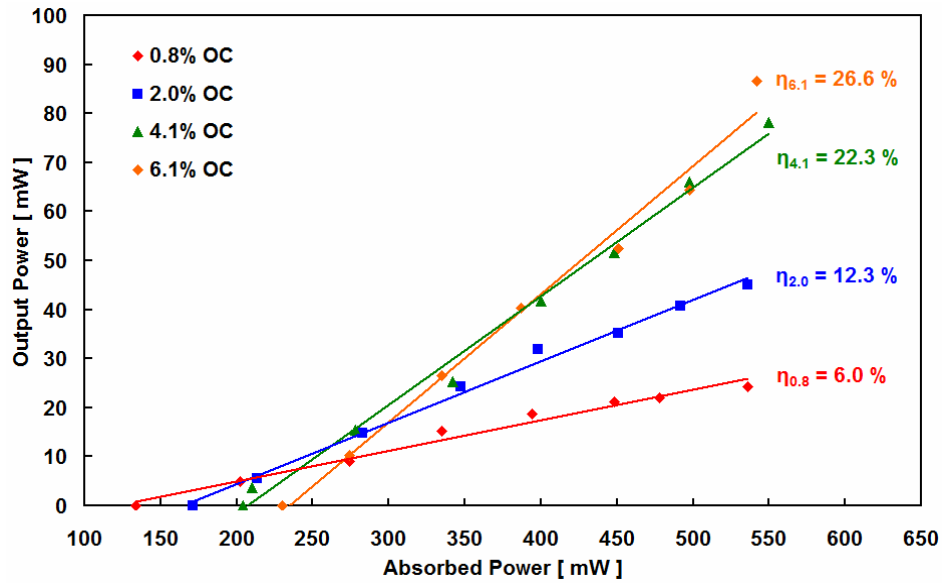
Fig 3.5 The absorbed to output power slope efficiencies of the tellurite sample $Tm_{1.5}$:TZN doped at 1.5 wt% for four different output couplers.

The angles of the two arms of the resonator were increased so to compensate for the stronger astigmatism inserted by the longer active element. The absorbed to output power curves were recorded for the four different output coupling transmissivities and are reported in Fig. 3.5. The maximum slope efficiency of 26.6% and 86 mW of output power were recorded for the 6.1% OC at a free-running wavelength of 1926 nm. The minimum threshold was at 195 mW of incident power with the 0.8% OC.
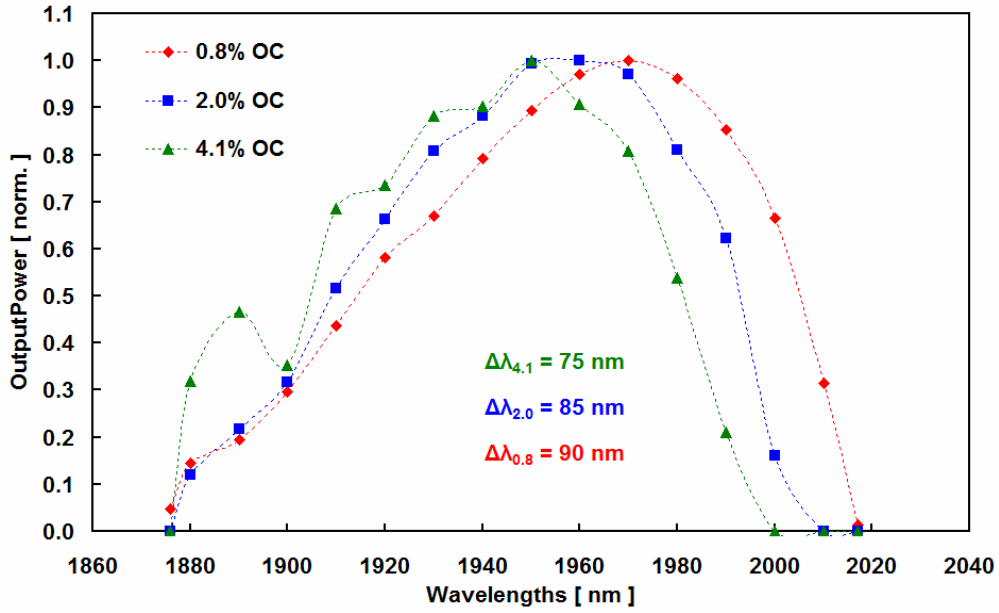

Fig 3.6 The tunability of the sample $Tm_{1.5}$:TZN doped at 1.5 wt% for three different OCs measured with the insertion of the prism. The FWHM of the curves are reported in the picture.

The tunability was once again recorded for the three output couplers with the fused silica prism inserted in the laser cavity and the maximum output powers after alignment optimization were 20 mW, 33 mW and 40 mW for the 0.8%, 2.0% and 4.1% OCs respectively. The normalized tunability curves are depicted in Fig. 3.6, as can be clearly noticed the laser has a narrower tuning range compared to the 2 wt% $Tm_{2.0}$:TZNG. The output power decreased for the 4.1% OC when tuned to 1900 nm exactly and that is due to thermal lensing instability. As for the first $Tm_{2.0}$:TZNG sample, for the 1.5 wt% doped $Tm_{1.5}$:TZN the inverse of the slope efficiencies plotted versus the inverse of the output coupler transmissivities, Fig 3.7, stand on a straight line with R^2 of 0.998. From the intersection of the straight line with the $1/\eta$ axis the maximum attainable efficiency value resulted $\eta_0 = 56\%$ for an approximate quantum efficiency of $\eta_Q = 140\%$.
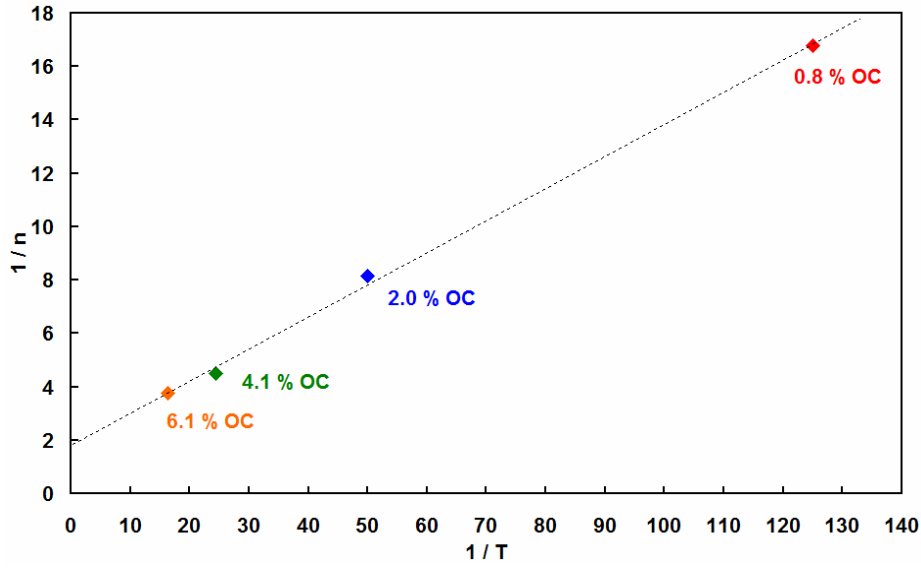
Fig 3.7 The inverse of the slope efficiencies of Fig 3.5 plotted versus the inverse of the output coupler transmissivities for the 1.5 wt% $Tm_{1.5}$:TZN sample, the results stand on a straight line.

As explained in chapter 2, due to the cross-relaxation mechanism in Tm^{3+} systems quantum efficiencies can theoretically reach 200%. The slope of the straight line was 0.121 and that yielded $\delta = 6.8\%$. Once more, taking into account the mirror losses and the reflection losses at the Brewster surfaces totalling 0.5% and quoting the number per centimetre of active material, we obtain $\delta_{Tm1.5:TZN} = 9 \pm 1$ %/cm, the error is estimated with a 2% experimental variation on the efficiencies of Fig 3.7.

Finally in this series of samples, the 1.0 wt% doped $Tm_{1.0}$:TZN was plane-plane polished and cut to a length of 10.3 mm so that nearly 70 % of the incident power at 793 nm was absorbed. The sample was glued with thermal conductive paint to the copper TEC surface at 15 °C and inserted on a V-cavity arranged to produce a mode spot size of 25 μm in radius. The pump beam spot size radius was also of 25 μm focused with a 50 mm focal-length lens. A very high threshold of 260 mW of incident power for the 0.8% OC was obtained. Threshold could not be reached for higher values of OC. The maximum power obtained was of 16 mW and the efficiency to the absorbed power was of 6%. The high threshold and the low gain of $Tm_{1.0}$:TZN compared to the other two samples suggested that the sample possessed high losses and a very low efficiency cross-relaxation process. Due to the poor characteristics measured for $Tm_{1.0}$:TZN the sample is not included in the discussion and comparison presented in the next section.

3.2.3 Comparison of Tm^{3+} doped tellurite glasses pumped at 793 nm

Although it is in principle very difficult to compare Tm$_{2.0}$:TZNG and Tm$_{1.5}$:TZN for the characteristic laser performances as changes are present in both composition and concentration of active ion, it is nonetheless very interesting to provide an analysis of the results to gain a deeper understanding of the inner workings of the two systems.

Sample codes	Tm^{3+} conc. [wt%]	Host	η at 6.1% OC [%]	η$_Q$ [%]	Max P$_{OUT}$ [mW]	δ [%/cm]	Peak σ$_E$ [10^{-21} cm^2]	τ$_F$ [ms]	Min P$_{TH}$ [mW]
Tm$_{2.0}$:TZNG	2.0	TZNG	28.4	87	124	2	5.3	1.3	134
Tm$_{1.5}$:TZN	1.5	TZN	26.6	140	86	9	6.2	1.14	195

Tab 3.2 The continuous wave laser performance characteristics and some spectroscopic parameters of the samples Tm$_{1.5}$:TZN and Tm$_{2.0}$:TZNG.

In table 3.2 some of the continuous wave results and of the spectroscopic parameters carried over from chapter 2 and relevant to the discussion below are presented. It is straightforward to notice that Tm$_{1.5}$:TZN has much higher losses, a slightly shorter lifetime and higher peak emission cross section than Tm$_{2.0}$:TZNG and that obviously accounts for a higher threshold according to formula (3.6). This is, in turn, compensated by a higher quantum yield η$_Q$ thus the overall optical efficiency becomes comparable to Tm$_{2.0}$:TZNG for the same output coupling conditions.

It has been shown that the cross-relaxation efficiency increases for increasing Tm^{3+} concentrations[3]. However it is clear from Table 3.2 that Tm$_{2.0}$:TZNG has a lower quantum efficiency than Tm$_{1.5}$:TZN and this is most likely to be due to an increased nonradiative relaxation rate from the $^3F_4$ lasing level to ground due to impurities. In order to fully appreciate the mechanism we need to define the important factors for the quantum yield, η$_Q$. For any given electronic level in a laser gain medium η$_Q$ depends on many parameters and its absolute value is estimated by the ratio of the measured luminescence lifetime τ$_F$ and the radiative time τ$_R$ obtained from the Judd-Ofelt (JO) theory model analysis[4]. The quantum yield, in the case of the Tm^{3+} $^3F_4$ lasing with $^3H_4$ pumping, closely connects to the cross-relaxation efficiency ($^3H_4$, $^3H_6$) → ($^3F_4$, $^3F_4$) which contributes up to a 200% to η$_Q$ as discussed in chapter 2. In a simplified fashion η$_Q$ can be written:

$$\eta_Q = \frac{\eta_{CR}}{\eta_{NR} \cdot \eta_{ESA}} \tag{3.4}$$

where η_{CR} is the cross-relaxation efficiency, η_{ESA} is the parasitic excited state absorption efficiency from $^3F_4$ and η_{NR} is the non-radiative transition efficiency that is directly proportional to the multi-phonon relaxation rate. The higher the peak phonon energy value, the higher η_{NR} is and consequently the lower the overall quantum efficiency. The processes are highlighted for clarity in the inset of Fig 3.8. The Raman spectra for the two glass samples $Tm_{2.0}$:TZNG and $Tm_{1.5}$:TZN were reported in Fig 2.5 section 2.4.1 up to 1000 cm^{-1} energy shifts.
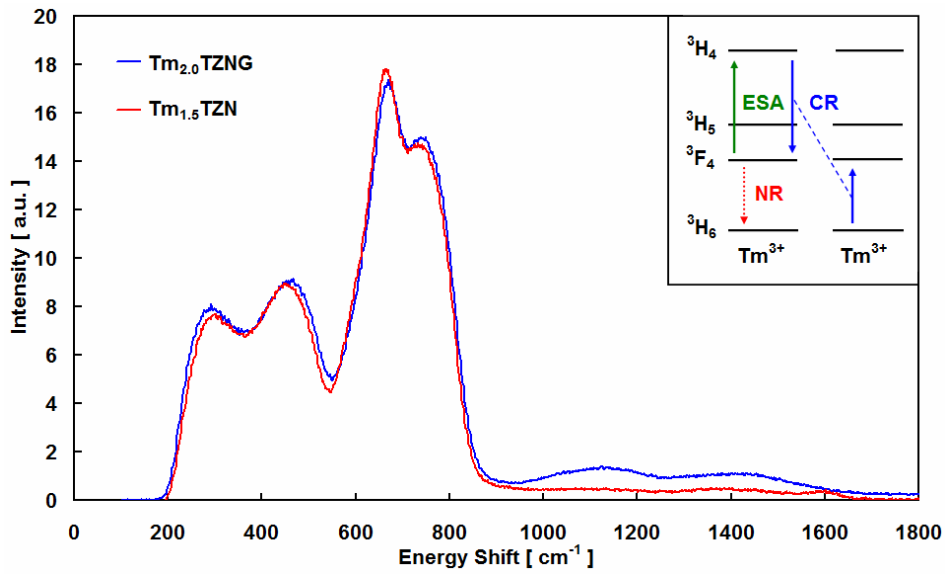
Fig 3.8 The Raman spectra for the $Tm_{2.0}$:TZNG and the $Tm_{1.5}$:TZN extended to 1800 cm^{-1}. In the inset the processes of Cross-relaxation CR, Excited State Absorption, ESA and Non-Radiative relaxation NR.

However it can be seen in Fig 3.8 that with further measurements extended up to 1800 cm^{-1} two peaks are present at 1120 cm^{-1} and 1430 cm^{-1}. These two peaks, possibly due to heavy metals impurities, may be responsible for the higher η_{NR} that is found in $Tm_{2.0}$:TZNG. Finally it is worth commenting on the mechanical strength of the two samples tested. Both of them sustained breakdown structural damage with high pump powers. The structural damage threshold was identified and cracks started to form for incident powers around 900 mW. Two types of damages could be observed, a dynamic one whereby the crack would close when the incident power decreased, and a static one that would permanently set in the structure.

3.3 Tm^{3+}-Ho^{3+} Tellurite Glasses

3.3.1 Introduction and sample description

The Tm^{3+}-Ho^{3+} glass samples were also prepared at the Institute of Materials Research at the University of Leeds as it was presented in section 2.5.2. In this section the laser performance characteristics of the Tm$_{2.0}$-Ho$_{0.4}$:TZN, Tm$_{2.0}$-Ho$_{0.2}$:TZN and Tm$_{2.0}$-Ho$_{0.1}$:TZN are compared. Table 3.3 summarizes the geometrical details and dopants concentrations of the samples used.

Sample codes	A	B	Dopants concentrations [wt%]		Tm^{3+}/Ho^{3+} ratio	Host
	A [mm]	B [mm]	Tm^{3+}	Ho^{3+}	[.]	
Tm$_{2.0}$-Ho$_{0.4}$:TZN	4.4	3.1	2.0	0.4	5	TZN
Tm$_{2.0}$-Ho$_{0.2}$:TZN	4.5	3.1	2.0	0.2	10	TZN
Tm$_{2.0}$-Ho$_{0.1}$:TZN	5	-	2.0	0.1	20	TZN

Tab 3.3 An overview of the Tellurite based samples doped with Tm^{3+} and Ho^{3+} where laser characteristics performances were recorded. Tm^{3+} is used as a sensitizer for Ho^{3+}.

The Tm$_{2.0}$-Ho$_{0.4}$:TZN was Brewster cut, polished and wrapped in indium foil while the Tm$_{2.0}$-Ho$_{0.2}$:TZN and the Tm$_{2.0}$-Ho$_{0.1}$:TZN were cut and parallel polished in house and glued to the TEC surface to be used in the laser cavity. In section 3.3.2 the continuous wave laser performance characteristics are described for the three samples in the following order: Tm$_{2.0}$-Ho$_{0.1}$:TZN, Tm$_{2.0}$-Ho$_{0.2}$:TZN and Tm$_{2.0}$-Ho$_{0.4}$:TZN.

3.3.2 Continuous wave laser performance characterizations

The Tm$_{2.0}$-Ho$_{0.1}$:TZN was cut and parallel polished in house to a thickness of 4.5 mm. The interaction length of the pump beam with the lasing mode was approximately 5 mm as the sample was inserted at Brewster's angle in the lasing setup. The copper substrate was kept at 15 °C and silver paint was used to glue the active element to it. The system is shown in Fig 3.9. The sample absorbed 67 % of the 793nm pump radiation. The pump beam was focused to a 23 µm beam spot size radius measured after M1 via a 50 mm focal length lens and the Z-folded resonator was designed to match the mode spot size accordingly.
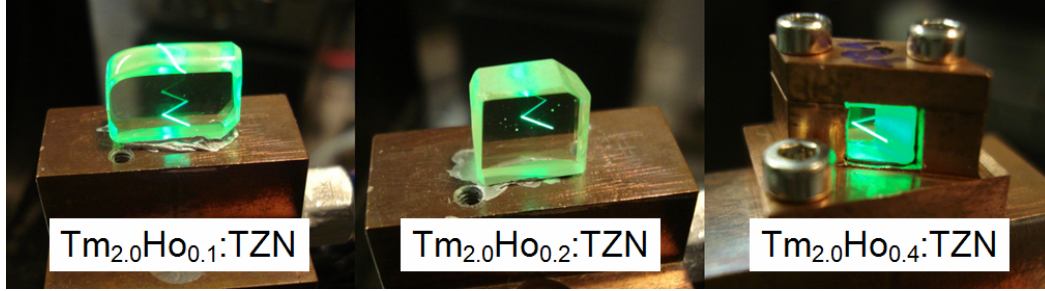
Fig 3.9 The three active elements as mounted to the TEC copper substrate for the laser characterizations.

The absorbed to output power characteristics curves, Fig 3.10, were recorded for the three output couplers 0.8 %, 2.0 % and 4.1 % and the slope efficiencies were found to be 17.9 %, 25.9 % and 25.6 % respectively. The free running wavelengths were 2048 nm and 2010 nm for the 0.8 % OC and for the 2.0 % OC demonstrating that emission was from the $^5I_7$ level of Ho^{3+}. The free running wavelength was 1966 nm for the 4.1 % OC and emitted from the $^3F_4$ level of Tm^{3+}. The free running emission wavelength corresponds to the wavelength at the peak of the gain at threshold lasing condition[5]. When increasing the output coupler value and therefore the roundtrip losses the threshold is reached for higher values of inversion β and consequently in the quasi-three level Tm^{3+}-Ho^{3+} system emission wavelengths shorten and eventually hop to the Tm^{3+} laser level $^3F_4$. The maximum output power obtained was of 74 mW at 2010 nm with a 2.0 % OC at 715 mW of incident power.
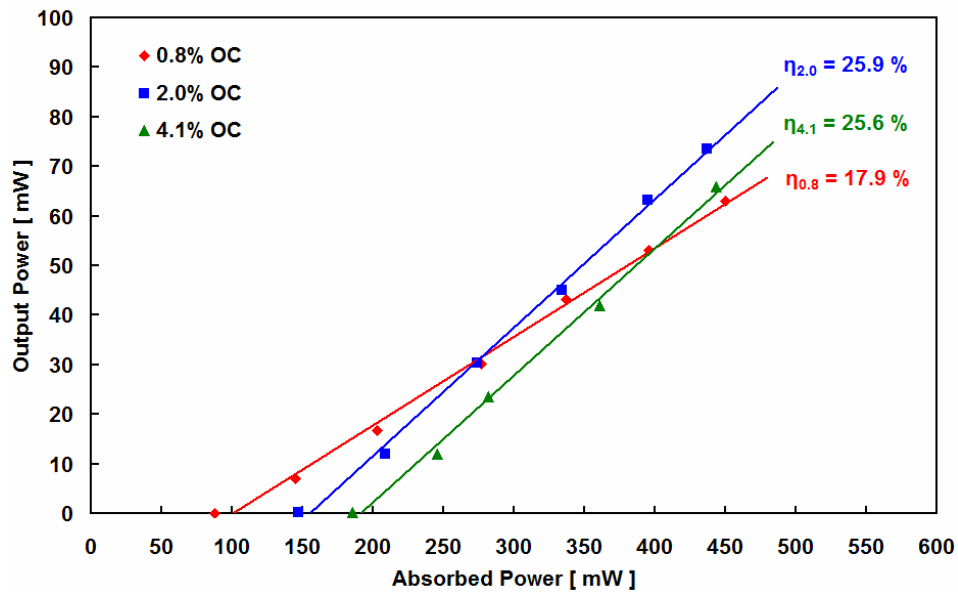

Fig 3.10 The absorbed to output power characteristics of the $Tm_{2.0}$-$Ho_{0.1}$:TZN sample when pumped at 793 nm.

The incident power was limited to prevent thermal damage and as can be seen in Fig 3.10 no rollover is present. A further confirmation of the Tm^{3+} lasing in the case of the 4.1% OC comes from the fact that the threshold and the efficiency of the laser are nearly identical to the one obtained for the singly doped $Tm_{2.0}$:TZNG sample that has the same thulium concentration. The lowest threshold was recorded at 120 mW of incident power with the 0.8 % OC. The tunability of the laser was measured for the 0.8 % OC. Prism insertion losses were negligible and the normalized tunability graph is reported in Fig 3.11.
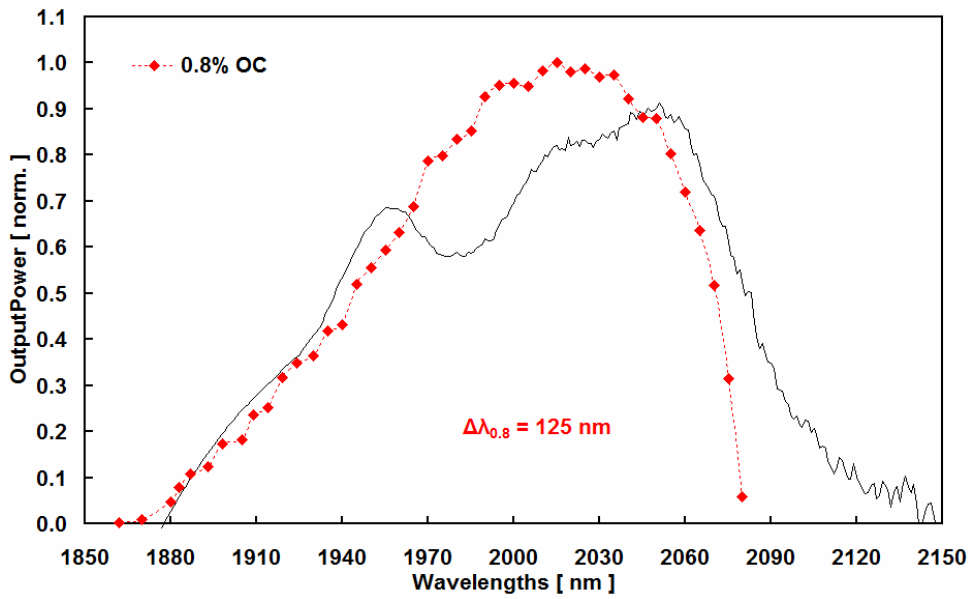
Fig 3.11 The tunability of the $Tm_{2.0}$-$Ho_{0.1}$:TZN sample measured the prism inserted in the laser cavity, the FWHM is 125 nm. The gain spectrum, thin black line, is overlapped.

The emission is limited on the blue side by the Tm^{3+} reabsorption losses and on the red side by the reflectivity of the 0.8 % OC mirror that reached 98% at 2080 nm. Fig 3.11 also shows the gain spectrum of the $Tm_{2.0}$-$Ho_{0.1}$:TZN derived from section 2.5.2 for an inversion factor $\beta = 0.13$, the two curves show a reasonable overlap. The emission, centred at 2020 nm, ranges from 1860 nm to 2080 nm with a bandwidth FWHM value of 125 nm. An estimation of the losses and maximum achievable slope efficiency gives value of η_0 as 37 % and the losses are $\delta = 0.9$ %. With mirrors and Brewster's surfaces the total losses quoted per centimetre are: $\delta_{Tm2.0Ho0.1:TZN} = 0.8 \pm 0.2$ %/cm. Losses are indeed very low in this sample and they demonstrate the quality of the glass and of the polished surfaces. The quantum efficiency is $\eta_Q = 96$ % and, in the case of Tm^{3+}-Ho^{3+}

transition, also accounts for the Tm^{3+} cross-relaxation efficiency $(^3H_4, {}^3H_6) \rightarrow (^3F_4, {}^3F_4)$ and the Tm^{3+} to Ho^{3+} energy transfer efficiency $^3F_4 \rightarrow {}^5I_7$.

The remaining Tm^{3+}-Ho^{3+} doped two samples possessed strong thermal lensing and the measurements had to be carried out with a 50:50 chopper at the pump beam. Powers reported are then renamed as *inferred* and obtained by doubling the measured values. This technique allows the assessment of the expected characteristics of the laser material while a solution to the thermal lensing is found. The reasons for the higher thermal lensing are investigated in the next section.

The $Tm_{2.0}$-$Ho_{0.2}$:TZN was cut and parallel polished in house with a thickness of 4 mm, the element inserted at Brewster's angle in the laser resonator had an interaction length with the pump beam that was then 4.5 mm. The sample was glued with conductive paste to the copper block as shown in Fig 3.9. The $Tm_{2.0}$-$Ho_{0.4}$:TZN was Brewster cut to a length of 4.5 mm polished with a square cross section of 3 by 3 mm, wrapped in Indium foil and inserted in a copper mount, the element can also be seen in Fig 3.9. Z-folded resonator arrangements were then set up and the absorbed to expected output powers efficiencies could be recorded. The curves, reported in Fig 3.12, were only taken with the 0.8 % OC for both samples as higher output coupling would prevent lasing or would produce very unstable lasing as it is explained in the following section. The maximum expected output powers were of nearly 40 mW with a slope of 11 % for the $Tm_{2.0}$-$Ho_{0.4}$:TZN and of 25 mW with a slope of 9.5 % for the $Tm_{2.0}$-$Ho_{0.2}$:TZN.
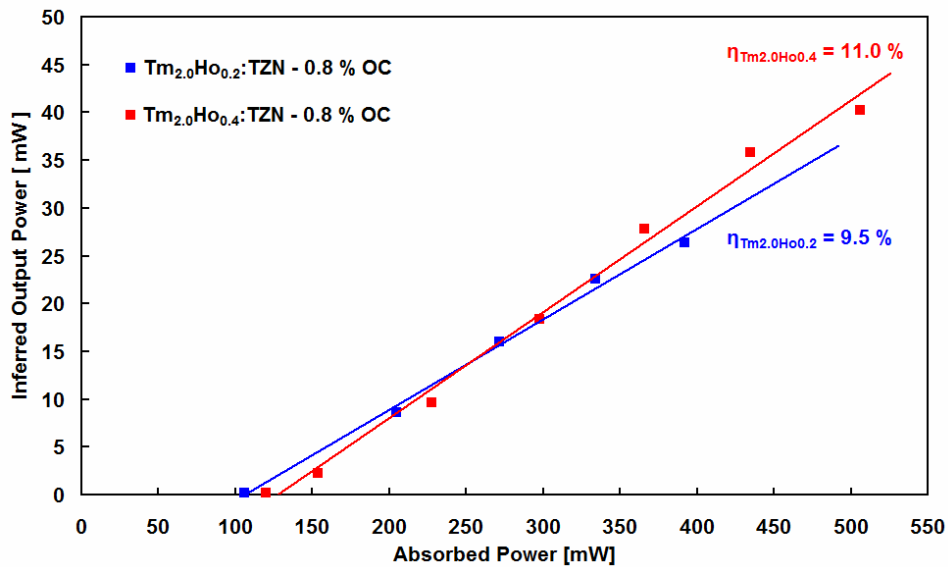

Fig 3.12 The absorbed to expected output power slope efficiencies of the two samples $Tm_{2.0}$-$Ho_{0.4}$:TZN and $Tm_{2.0}$-$Ho_{0.2}$:TZN. Powers are *inferred* as explained in the text.

Thresholds were recorded around 150 mW of incident power. In order to obtain a fuller picture of the characteristics of these two laser gain material the tunability was also recorded with the fused silica prism inserted at the minimum deviation angle. The tunability was smooth across the emitted wavelengths and extended from 2005 to 2095 nm peaking at 2066 nm and with a FWHM of 60 nm for the $Tm_{2.0}$-$Ho_{0.4}$:TZN. The $Tm_{2.0}$-$Ho_{0.2}$:TZN sample emission could be tuned from 1960 to 2100 nm centred in 2045 nm with a full width at half maximum of 80 nm.

3.3.3 Comparison of Tm^{3+}-Ho^{3+}:Tellurite glasses pumped at 793 nm

Among all the Tm^{3+}-Ho^{3+} doped tellurite samples tested the continuous wave performance characteristics were very different and dramatically worsened when increasing the Ho^{3+} concentration from 0.1 to higher concentrations and the Tm^{3+}/Ho^{3+} concentration ratio from 20 to lower values. Since the latter two samples $Tm_{2.0}$-$Ho_{0.2}$:TZN and $Tm_{2.0}$-$Ho_{0.4}$:TZN did not lase or produced unstable lasing with output couplers higher than 0.8 % the parameters that can be significantly compared are summed in table 3.4. The losses that this class of samples showed were very low in the order of 0.8 %/cm but they could be measured only for the $Tm_{2.0}$-$Ho_{0.1}$:TZN as higher output couplers would prevent lasing. In this aspect it is interesting to notice that higher output couplers in Tm^{3+}-Ho^{3+} doped systems required higher inverted populations to reach threshold and this in turn increased the upconversion losses to the $^5S_2$, $^5F_4$ Ho^{3+} levels as we demonstrated for the Tm,Ho:KYW crystal[6].

Sample codes	Ho^{3+} conc.	Tm^{3+}/Ho^{3+} ratio	η at 0.8% OC	Max P_{OUT} 0.8% OC	Spectrum $\Delta\lambda_{FWHM}$
	[wt%]	[.]	[%]	[mW]	[nm]
$Tm_{2.0}$-$Ho_{0.4}$:TZN	0.4	5	11 *	28 *	60 *
$Tm_{2.0}$-$Ho_{0.2}$:TZN	0.2	10	9.5 *	26 *	80 *
$Tm_{2.0}$-$Ho_{0.1}$:TZN	0.1	20	17.9	55	125

Tab 3.4 The continuous wave laser parameters that are compared for the three Tm^{3+}-Ho^{3+} doped tellurite glass samples. * expected values measured with the 50:50 chopper. The maximum powers are reported for the same absorbed power.

Strong thermal lensing was present with the samples having low Tm^{3+}/Ho^{3+} ratio, the characteristics were therefore estimated with the 50:50 chopper and are highlighted in

Table 3.5. This increased thermal lensing may have been caused by highly localized heat that generates in these samples as a result of high energy photons that find paths to nonradiatively relax to ground $^5S_2, ^5F_4 \rightarrow ^5I_8$. The Ho^{3+} concentration is in fact higher in these samples and so is the density of photons that upconvert to $^5S_2, ^5F_4$ levels, see Fig 3.13 for a simplified energy transfers scheme.

The energy transfer ET processes accounting for populating the Ho^{3+} levels, are mainly in the $Tm^{3+} \rightarrow Ho^{3+}$ direction but in the case of the $^3F_4 \leftrightarrow ^5I_7$ it is very much bidirectional and dependent on dopants concentration. This affects the lifetimes of the two levels as it is explained in section 2.3.3. The parasitic 550 nm green upconversion takes place from the long lived $^5F_4$ and the mechanism is non-trivial. Ions in $^3F_4$ upconvert via UC1 in $^5I_5$ and then relax to $^5I_6$ populating it. Ions directly pumped from $^3H_4$ then via UC2 pass their energy to the population in $^5I_6$ upconverting them to $^5F_2$. The ions in $^5F_2$ finally nonradiatively relax to $^5F_4$.
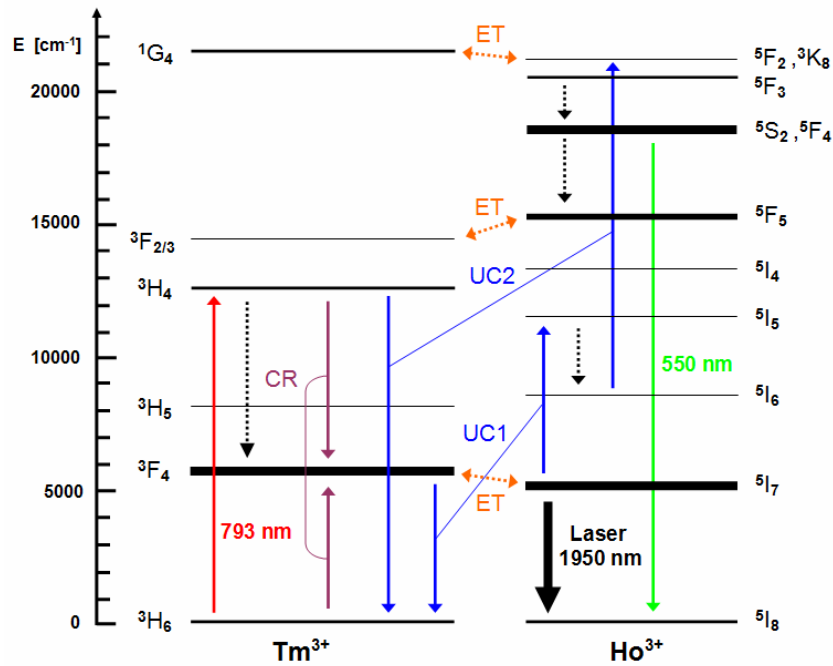

Fig 3.13 Tm^{3+}-Ho^{3+} Energy levels diagram when pumped at 793 nm. Continuous straight lines highlight the main radiative transitions. The main energy transfer mechanism involved are upconversion (UC1, UC2), cross-relaxation (CR) and energy transfers (ET). Dashed lines indicate phonon-assisted transitions and nonradiative energy transfer. The energy levels are weighed according to their radiative lifetime[8].

This process is efficient also because pump photons can directly promote ions from $^5I_6$ to $^5F_2$ as their energy coincides with the energy difference between the two levels, the

process in known as excited state absorption, ESA, and was not reported in Fig 3.13 for simplicity. Furthermore, once infrared photons from the pump or Tm^{3+} radiative relaxations become available to the Ho^{3+} ion, the UC process is very efficient and was demonstrated as 50 times stronger than other UC processes in the tellurite network[7]. This is the reason why performance characteristics generally deteriorate by decreasing the Tm^{3+}/Ho^{3+} ratio, tunability ranges decreases, output powers decrease and thermal lensing worsen. There is a 1.5 % small difference between the expected slope efficiencies of the two $Tm_{2.0}$-$Ho_{0.4}$:TZN and $Tm_{2.0}$-$Ho_{0.2}$:TZN samples which is well within experimental error.

3.4 Tm^{3+} Fluorogermanate Glasses

3.4.1 Performance characteristics of the Tm^{3+}:GPNG

The Tm^{3+} doped composition of germanium oxide, lead fluoride, sodium oxide and gallium oxide, GPNG, was extensively introduced in section 2.4 and was in turn derived from an all-oxides composition formed at high temperature of 1200 °C. One Tm^{3+}:GPNG sample was produced and was cut and parallel polished in St Andrews to a thickness of 4.5 mm and inserted at Brewster's angle in a standard Z-folded laser resonator. The pump beam, tuned at 792 nm was focused with a 50 mm lens to a 25 µm spot size radius inside the glass with an interaction length of 5.1 mm. 64 % of the incident radiation was absorbed. Once again four output coupling sets were used and the absorbed to output power slope efficiencies obtained were 32.4 %, 39.6 %, 47.8 % and 49.7 % with the 0.8 %, 2.0 %, 4.1 % and 6.1 % output couplers respectively. The rollover free curves are reported in Fig 3.14. Due to the quasi three level nature of the lasing transition the free running wavelengths were 1985, 1979, 1953 and 1944 nm with the 0.8 %, 2.0 %, 4.1 % and 6.1 % OCs respectively. The maximum output power obtained was of 190 mW with the 4.1 % output coupler and it was limited by the pump power that was set at 750 mW at most to avoid thermal damage to the glass. Once the characterization had been completely carried out the pump power was increased to the maximum power available with the Ti:Sapphire of 1100 mW and the maximum output power reached ~ 300 mW with the 4.1 % OC.
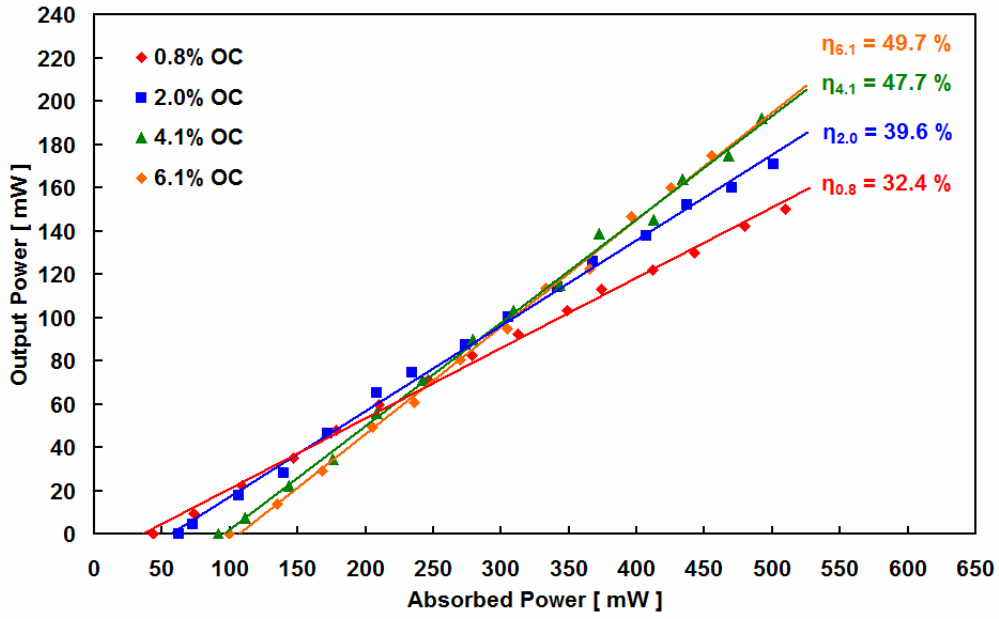
Fig 3.14 The absorbed to output power slope efficiencies for the Tm^{3+}:GPNG for four different output coupling values. The slope efficiency values are reported on the graph.

Thermal lensing up to the incident powers tested was not experienced in this material and an explanation is given further in the section. Lasing threshold values were also very low and with a minimum of 60 mW of incident power with the 0.8 % OC. The lasing thresholds obtained could also be modelled with the Risk model[9]. Formula (3.5) details the parameters involved:

$$P_{th}(T) = \frac{\pi h \upsilon_P (4w_L{}^2 + 4w_P{}^2)(\delta + T + 2\delta_R(\lambda_{FR}))}{4\sigma_E(\lambda_{FR}) \cdot \tau_F} \tag{3.5}$$

where $h\upsilon_P$ is the energy of the pump photons, δ is the roundtrip scattering loss which value is calculated below, T the transmission losses of the mirrors and w_L and w_P the beam waist radiuses. It has to be highlighted that in order for the model to adhere do the experimental results the $\delta_R(\lambda_{FR})$ one-pass reabsorption losses and $\sigma_E(\lambda_{FR})$ emission cross-section must be taken from the absorption spectra and the emission cross-section spectra respectively *at the free running emission wavelength*. Finally τ_F is the lifetime of the lasing level $^3F_4$. The results obtained are plotted in Fig 3.15 and show that the experimental data fit well the model within modelling errors. The losses could also be estimated and gave values of $\eta_0 = 52.5$ % and the loss, $\delta = 0.51$ % generating a %/cm scattering loss, $\delta_{Tm:GPNG} = 0.02 \pm 0.2$ %/cm. This value is very low and confirms the high quality of the glass specimen in use.
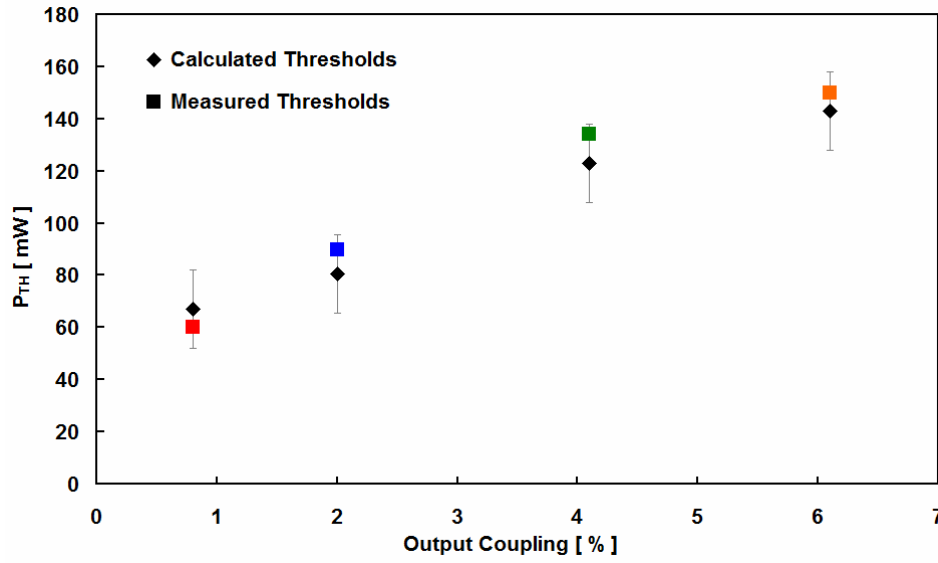
Fig 3.15 The threshold values plotted against the four different output couplers used for the Tm[3+]:GPNG. The square dots represent the measured thresholds.

From these values, the inferred quantum efficiency was $\eta_Q = 130\ \%$. The tuning curve is shown in Fig 3.16 and shows the emission peaks at 2030 nm and its full width at half maximum is of 140 nm. The gain spectrum from section 2.5.3 is overlapped in Fig 3.16 for an inversion factor $\beta = 1$ and smoothed with the moving average, it can be clearly seen that the emission on the longer wavelengths is limited by the decreasing gain. The tunability on the blue side is, as in all quasi-three level laser system, limited by the reabsorption losses.
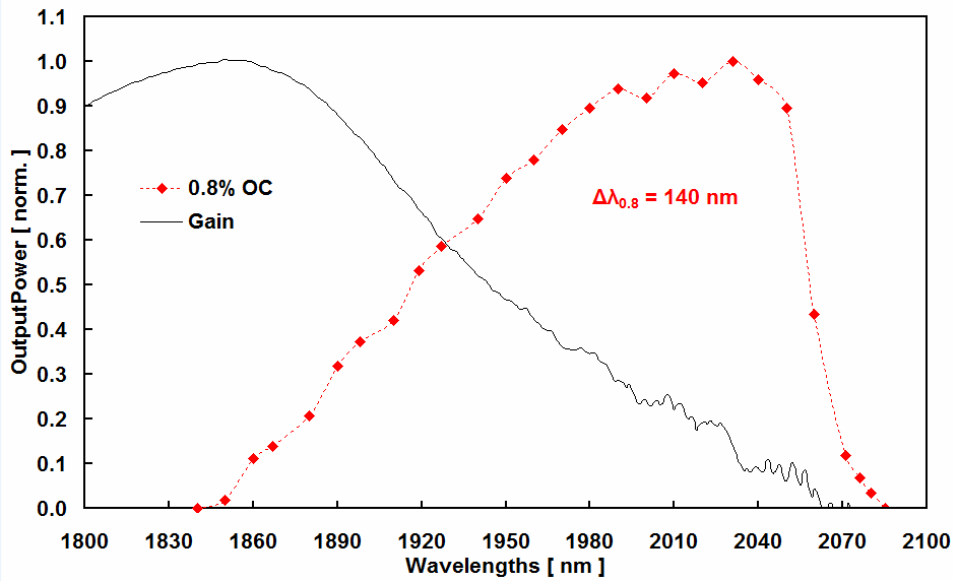

Fig 3.16 The tunability of the Tm[3+]:GPNG measured with the prism and the 0.8 % OC. The FWHM is 140 nm. The thin black line represents the gain spectrum.

The performance characteristics obtained with the Tm^{3+}:GPNG fluorogermanate glass, and especially the efficiency to the absorbed power, represent the highest achieved in the literature to date for an end pumped bulk glass lasers emitting at 2 μm and the results were accepted for publication in Optics Express. Furthermore the glass had not reached its best performance as the quality of the cast specimen was not fully optimised. The high quantum efficiency is allegedly due to the lower local peak phonon energy[10] the Tm^{3+} ions interact with, this in turn decreases the multi-phonon relaxation rates and therefore yields improved efficiencies. The experimental evidence that the measurements taken were virtually free of thermal lensing can be explained by one important fact. Despite being cut to a 4.5 mm thickness, parallel polished and inserted at Brewster's angle inside the laser resonator likewise the Tellurite specimens, the Fluorogermanate sample absorbed only 65 % of the incident radiation compared to the 80 % of the Tellurite counterparts. This of course had an effect on the amount of heat locally deposited in the structure and ultimately on the thermal lensing. The laser characteristics of this Fluorogermanate and of all others are compared in section 3.6.

3.5 Tm^{3+} Fluoride Glasses

3.5.1 Performance characteristics of the Tm^{3+}:ZBLAN

The spectroscopy of the 2 mol% Tm^{3+} doped ZBLAN fluoride composition is reported in section 2.5.4. The ZBLAN has had widespread use for its exceptional optical qualities[11-12] and it represented a good benchmark for our research project. The optical quality of the sample was outstanding compared to the Tellurite and the Fluorogermanate ones and, it can be seen in section 2.5.4 Fig 2.15, that the scattering line on the absorption spectrum was nearly zero.

The sample was machined from a disc of 25 mm in diameter, it was polished to optical quality and cut to a length of 9 mm and inserted in the standard Z-folded laser cavity under the experimental conditions formerly described. The interaction length of the active sample inserted at Brewster's angle was 10.8 mm and the sample absorbed nearly 52 % of the incident radiation. The slope efficiencies obtained were 19.9 %, 30.5 %, 37.7 % and 37.6 % with the 0.8 %, 2.0 %, 4.1 % and 6.1 % output couplers. The free running wavelengths were from 1944 nm to 1911 nm for increasing output coupling

transmittances. The curves are reported in Fig 3.17.The minimum threshold value was measured with the 0.8 % OC and was of 80 mW of incident power. Lasing was observed without appreciable thermal lensing and no rollover up to the maximum incident powers used of 820 mW. The maximum output power recorded was of 145 mW with the 4.0 % OC.
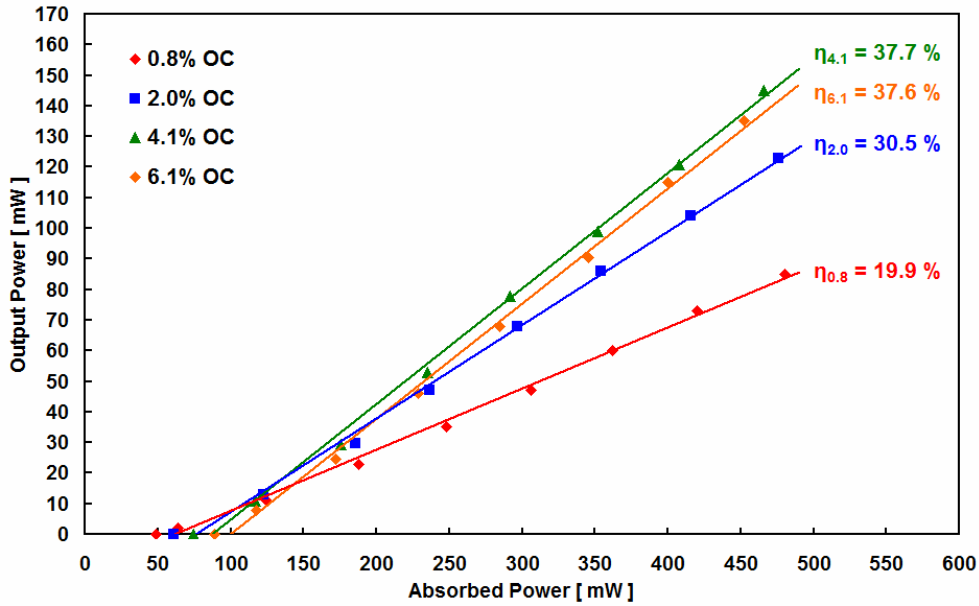

Fig 3.17 The absorbed to output power slope efficiencies of the Tm^{3+}:ZBLAN fluoride sample measured for the four output couplers.

The output radiation was very stable once the cavity was optimized and this it is likely to be due to the long interaction length and thus the large active volume compared to previous experiments. The laser emission peaking at 1980 nm was tuneable from 1810 to 2050 nm with a record FWHM of 150 nm. The losses analysis yielded an η_0 of 45.7 %, $\delta_{Tm:ZBLAN} = 0.5 \pm 0.2$ %/cm and $\eta_Q = 115$ %.

3.6 Conclusions and comments

In this chapter, the continuous wave characteristic performances of different solid state 2 µm bulk glass based laser systems were described and the treatment was especially focused on the Tellurite based ones. Section 3.2 extensively dissected the Tellurite media doped with Tm^{3+} as an active ion while the Tm^{3+}-Ho^{3+} were presented in section 3.3. It is very difficult to compare the two systems on an absolute basis because of the difference on the dopant concentration and combination; however it is worth presenting

here the relevant laser characteristics in the perspective of 2 µm solid state Tellurite laser sources pumped at 793 nm. Table 3.5 sums up the lasing data for the best Tm^{3+} doped sample, $Tm_{2.0}$:TZNG, and the best Tm^{3+}-Ho^{3+} doped sample, $Tm_{2.0}$-$Ho_{0.1}$:TZN.

Sample codes	η at 2.0% OC [%]	P_{OUT} with P_{ABS} = 440 mW 2.0% OC [mW]	P_{ABS} at threshold 2.0% OC [mW]	Spectrum $\Delta\lambda_{FWHM}$ 0.8% OC [nm]	λ [nm]
$Tm_{2.0}$:TZNG	19.6	60	138	135	1960
$Tm_{2.0}$-$Ho_{0.2}$:TZN	25.9	74	147	125	2020

Tab 3.5 The continuous wave laser parameters that are compared for the two tellurite laser media as 2 µm laser sources the $Tm_{2.0}$:TZNG and the $Tm_{2.0}$-$Ho_{0.1}$:TZN.

The internal efficiency of the two laser sources is reported for the 2.0 % OC, the reason is that the Ho^{3+} ion in the $Tm_{2.0}$-$Ho_{0.1}$:TZN sample stopped lasing for higher output couplers. It is interesting to see that an efficient $Tm^{3+} \rightarrow Ho^{3+}$ energy transfer yields greater internal efficiencies for the doubly doped Tm^{3+}-Ho^{3+} sample. The output power and the absorbed power at threshold are therefore reported with the 2.0 % OC and although the threshold values are similar the output power is 25 % higher in the Tm^{3+}-Ho^{3+} sample. Spectral tunability is alike for the two samples and their peak wavelength is characteristic to the respective lasing ions. It can be stated then that overall performance characteristics of the Tm^{3+}-Ho^{3+} doubly doped sample were better as a 2 µm laser material and looked promising as a potential candidate for mode-locking. Mode-locked results are presented in chapter 5.

In the main body of the chapter also two other substrate were presented a Tm^{3+} doped Fluorogermanate sample and a Tm^{3+} doped Fluoride ZBLAN glass. The results were described in Section 3.4 and Section 3.5 respectively. As it was introduced in Section 2.3.2 each network former, NWF, is characterized by a peak phonon energy that is peculiar of the vibrational energy modes of the atoms and ions nanoscale arrangement. Even though the effect of the ion concentration should be factored in and a full treatment would have to be done for different concentrations in different hosts it is relevant in this PhD to compare the different results obtained for the three main NWF treated. In this respect Fig 3.18 shows the absorbed to output power curves for the three samples: $Tm_{2.0}$:TZNG, Tm^{3+}:GPNG and Tm^{3+}:ZBLAN for the 0.8 % OC.
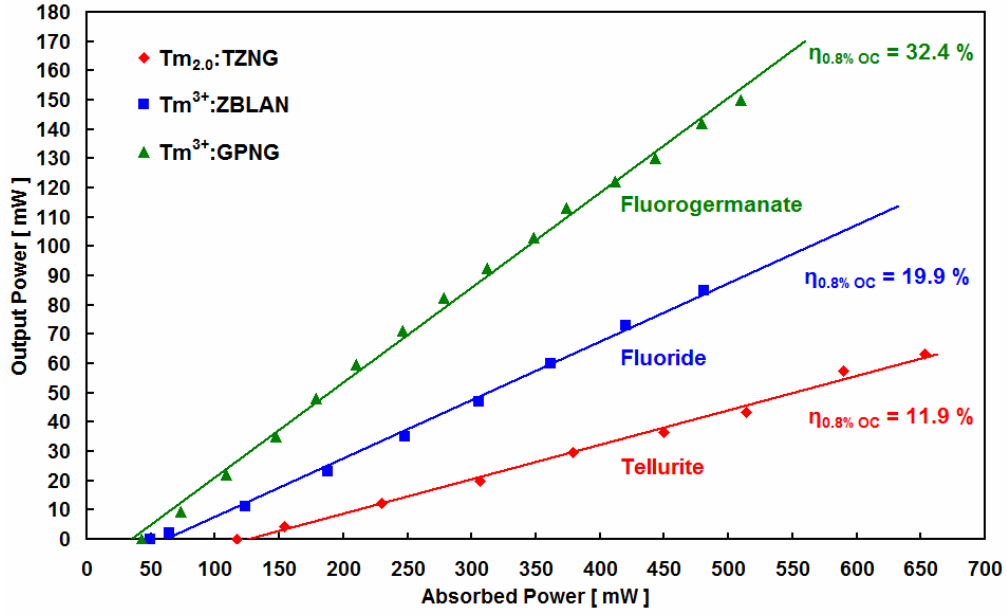
Fig 3.18 The absorbed to output power curves for the $Tm_{2.0}$:TZNG, Tm^{3+}:GPNG and Tm^{3+}:ZBLAN lasers tested during this PhD with the 0.8 % OC.

The superior laser characteristics of the fluorogermanate gain element is clear. Since the pumping beam waist adopted was similar for all three materials it is therefore possible to compare threshold values and the recorded lowest was for the fluorogermanate element. High internal efficiency and output powers associated with the GPNG sample are comparable to the values obtained for crystalline bulk lasers[6, 13].
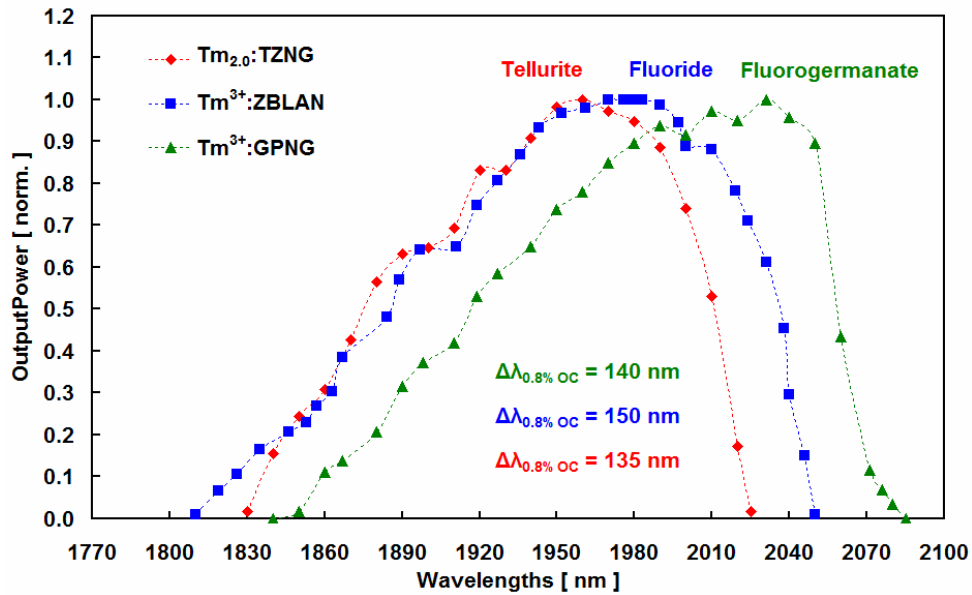

Fig 3.19 The tunability of the $Tm_{2.0}$:TZNG, Tm^{3+}:GPNG and Tm^{3+}:ZBLAN lasers tested during this PhD with the 0.8 % OC measured with the prism.

This confirms that Germanium based amorphous glasses represent an optimum candidate for high performance solid state infrared lasers as presented by G. Turri et al.[14]. All active elements had good stable output powers and provided for relatively thermal lensing free operations, however from a mechanical strength and chemical stability Germanium based oxyfluoride compounds are to be preferred as can be read in chapter 2. In our GPNG composition a substantial percentage of it is Lead Oxide that for its toxicity and environmental impact would need to be replaced in future developments. The laser emission when tuned with a prism and with the 0.8 % OC for the three elements is reported in Fig 3.19. For the three elements the FWHM reported in the picture are similar and it is easy to see that laser elements based on NWF that had higher gains can be tuned to longer wavelengths. Reabsorption losses are higher in the Fluorogermanate sample and limit the emission on the short wavelength tail of the tunability more than the other networks. Nevertheless, in all cases, tuning was smooth and continuous as it is expected in an inhomogeneously broadened material and this was fundamental in the use of such media for the mode-locked experiments introduced in chapter 5.

3.7 References

[1]   F. Fusari, *et al.*, "*Spectroscopic and lasing performance of Tm^{3+}-doped bulk TZN and TZNG tellurite glasses operating around 1.9 μm*", Optics Express, **16**, pp. 19146-19151, (2008).

[2]   J. A. Caird, *et al.*, "*Quantum Electronic Properties of the Na$_3$Ga$_2$Li$_3$FI$_{12}$ Cr^{3+} Laser*", IEEE Journal of Quantum Electronics, **24**, pp. 1077 - 1098, (1988).

[3]   H. Gebavi, *et al.*, "*Spectroscopic investigation and optical characterization of novel highly thulium doped tellurite glasses*", Journal of Non-Crystalline Solids, **355**, pp. 548-555, (2009).

[4]   A. Sennaroglu, *et al.*, "*Spectroscopic properties ot Tm3+: TeO2-PbF2 glasses*", Journal of Luminescence, **116**, pp. 79-86, (2006).

[5]   H. M. Pask, *et al.*, "*Ytterbium-Doped Silica Fiber Lasers - Versatile Sources for the 1-1.2 Mu-M Region*", IEEE Journal of Selected Topics in Quantum Electronics, **1**, pp. 2-13, (1995).

[6]   A. A. Lagatsky*, et al.*, "*Optical spectroscopy and efficient continuous-wave operation near 2 μm for a Tm, Ho:KYW laser crystal*", Applied Physics B-Lasers and Optics, **97**, pp. 321-326, (2009).

[7]   A. K. Singh*, et al.*, "*Up-conversions in Ho3+ doped tellurite glass*", Journal of Alloys and Compounds, **403**, pp. 97-103, (2005).

[8]   G. H. Dieke and H. M. Crosswhite, "*The Spectra of the Doubly and Triply Ionized Rare Earths*", Applied Optics, **2**, pp. 675-686, (1963).

[9]   W. P. Risk, "*Modeling of Longitudinally Pumped Solid-State Lasers Exhibiting Reabsorption Losses*", Journal of the Optical Society of America B-Optical Physics, **5**, pp. 1412-1423, (1988).

[10]   S. Todoroki*, et al.*, "*Local-Structure around Rare-Earth Ions in Indium-Based and Lead-Based Fluoride Glasses with High up-Conversion Efficiency*", Journal of Non-Crystalline Solids, **143**, pp. 46-51, (1992).

[11]   J. L. Doualan*, et al.*, "*Spectroscopic properties and laser emission of Tm doped ZBLAN glass at 1.8 μm*", Optical Materials, **24**, pp. 563-574, (2003).

[12]   W. E. K. Gibbs*, et al.*, "*Population dynamics of the 3F4 and 3H4 levels in highly-doped Tm3+:ZB(L)AN glasses*", Journal of Non-Crystalline Solids, **353**, pp. 1-5, (2007).

[13]   X. Han*, et al.*, "*Continuous-wave laser operation of Tm and Ho co-doped NaY(WO4)(2) and NaLu(WO4)(2) crystals*", Optics Express, **18**, pp. 5413-5419, (2010).

[14]   G. Turri*, et al.*, "*Temperature-dependent spectroscopic properties of Tm^{3+} in germanate, silica, and phosphate glasses: A comparative study*", Journal of Applied Physics, **103**, p. 093104, (2008).

4. BULK GLASS CONTINUOUS WAVE 2 μm LASERS PUMPED AT 1200 nm

4.1 Chapter Synopsis

This chapter presents a discussion of the continuous wave laser performance characteristics obtained from Tm^{3+} and Tm^{3+}-Ho^{3+} doped Tellurite glasses pumped by a 1200 nm semiconductor disk laser (SDL) system. A brief account of the SDL is presented in section 4.2.

The SDL pump system was developed the Institute of Photonics, IOP at Strathclyde University in Glasgow[1] and two different glass samples were tried with $^3H_6 \rightarrow {}^3H_5$ pumping, one singly Tm^{3+} doped and one doubly doped Tm^{3+}-Ho^{3+}.

The Tm^{3+} doped sample used for laser characterizations under this new pumping scheme was the 2 wt% doped TZNG and its laser performances are reported in section 4.3.1. $Tm_{2.0}$:TZNG was selected as it demonstrated very good laser performances when pumped at 793 nm by Ti:Sapphire. The Tm^{3+}-Ho^{3+} doped element selected for $^3H_5$ excitation was the Tm^{3+} 2 wt% and Ho^{3+} 0.2 wt% that was named $Tm_{2.0}$-$Ho_{0.2}$:TZN the results obtained are presented in section 4.3.2. Unfortunately $Tm_{2.0}$-$Ho_{0.2}$:TZN was not the best sample in 793 nm pumping but it was the only one available at the time the

1200 nm source could be used in St Andrews. Drawing from the results reported in the previous chapter, section 4.4 reports the comparison of the performances for the two excitation mechanisms $^3H_4$ (793 nm pumping) and $^3H_5$ (1200 nm pumping) in the two systems, the singly doped one and the doubly doped one. A brief explanation of the main energy transfers that happen in the Tellurite network in the two cases of $^3H_4$ and $^3H_5$ pumping are also reported in section 4.4.

4.2 Semiconductor disk laser at 1200 nm

4.2.1 Introduction to the SDL structure

In section 2.3 the different level transitions and therefore possible pumping schemes for the Tm^{3+} ion were introduced. Many excitation paths were presented and Ti:Sapphire excitation of the $^3H_4$ transition around 800 nm was shown to be the most widely used for pumping lasers operating around 2 μm. Another less frequent way of creating a population inversion on the $^3F_4$ level is the excitation of the $^3H_5$ level around 1200 nm pumping. Only very few commercially available pump sources have been developed in such region and we therefore collaborated with the Institute of Photonics, IOP at Strathclyde University in Glasgow and the group of Prof. M. D. Dawson to obtain the use of a Semiconductor Disk Laser, SDL[2]. SDLs can produce very good quality laser beams and their emission wavelengths can be customized, for these reasons they are suitable for the exploitation as end-pumped bulk laser pump sources[3].
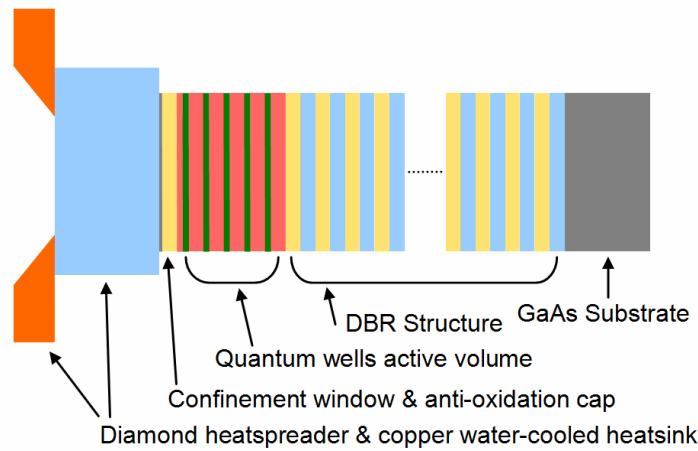

Fig 4.1 The SDL device layered structure sectioned along a plane perpendicular to the device surface. All key elements of the structure are highlighted.

85

The optically-pumped SDL used in this research was developed by Ms Sharon Vetter and Dr Stephane Calvez[1]. They are also known as the vertical-external-cavity surface-emitting lasers (VECSEL)[4] and the working principle, optical resonator arrangements and laser characteristics are briefly introduced here. The SDL device, reported in detail in Fig 4.1, is fabricated via molecular beam epitaxy on a Gallium arsenide GaAs substrate. A distributed Bragg reflector DBR mirror structure is designed to be highly reflective from 1180 nm to 1300 nm and directly grown on the GaAs substrate, with 30.5 layered pairs of AlAs/GaAs. The active volume was designed as a resonant 3.5λ-cavity with five pairs of strain-compensated $Ga_{0.71}In_{0.29}N_{0.011}As_{0.989}/GaAs_{0.989}N_{0.011}$ quantum wells, QW, and $3\lambda/4$ $Al_{0.3}Ga_{0.7}As$ confinement window and a 10 nm GaAs cap to prevent oxidation. The SDL chip was bonded on to a type II synthetic diamond heatspreader using the liquid-capillary method[5], and then mounted on to a copper heatsink that was water-cooled to 10 °C. The diamond bonding technique guarantees an efficient thermal management and allows the extraction of very high continuous wave output powers.
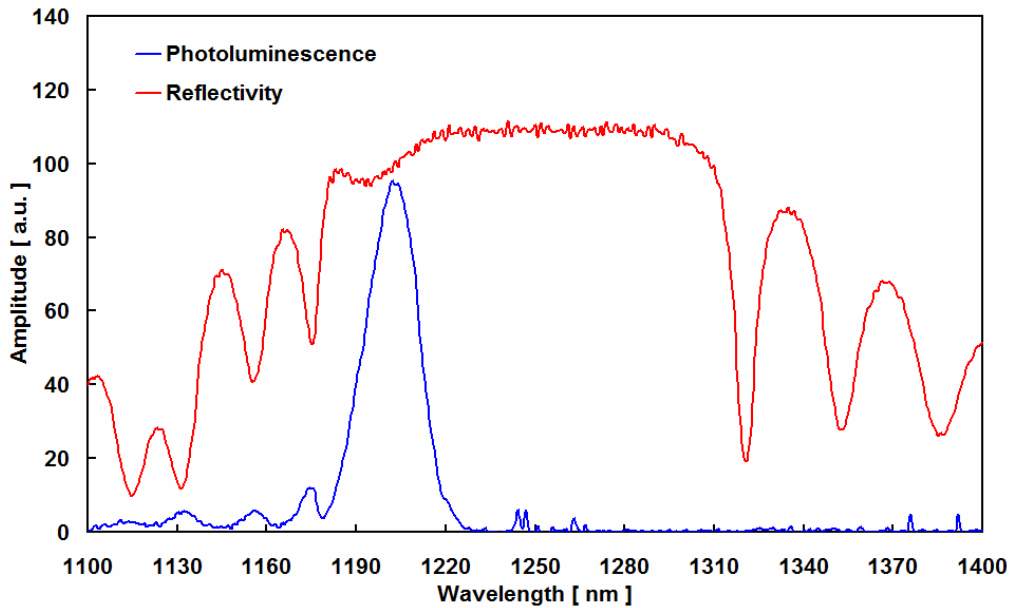

Fig 4.2 The reflectivity and surface photoluminescence spectra of the SDL structure measured at 20 °C from 1100 nm to 1400 nm.

The confinement window that sits on top of the whole structure is transparent to the pump photons[6], they are therefore almost completely absorbed by the active region as their energy (1.534 eV) is higher than the bandgap energy of the active volume (~1.43 eV [7]). Electron-hole pairs are then optically created in the volume, the carriers diffuse

in the structure, the QW captures them hence creating optical gain. The reflectivity and the surface photoluminescence spectra measured at 20°C of the device obtained are shown in Fig 4.2.

4.2.2 SDL Laser performance characterizations

The SDL device could then be exploited as an *active mirror* and it was inserted in a resonating cavity, depicted in Fig 4.3, so to produce optical feedback and achieve stimulated emission around 1200 nm. The pump laser used was an 808 nm diode laser array with 10.3 W maximum output power and fiber-coupled to a 100 µm core fiber with numerical aperture NA of 0.22. The laser performances were measured in Strathclyde University but measurements were repeated once the system had been moved to St Andrews.
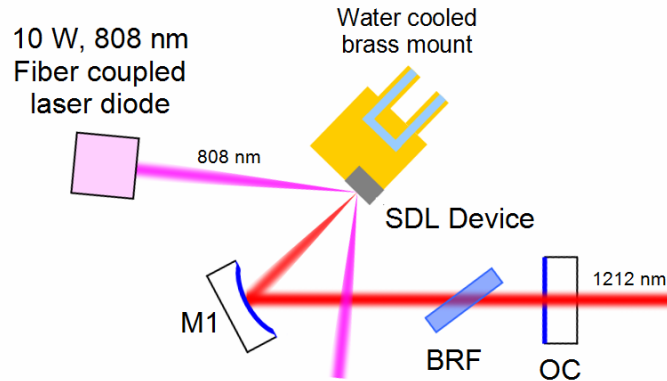

Fig 4.3 The V-cavity used to generate 1200 nm coherent radiation off the SDL device. The BRF is a custom-designed birefringent filter and OC is the output coupler.

The pump beam was, in turn, focused to a 40 µm radius mode size. The SDL gain element was used as the end mirror of a V-cavity configured to form a 38 µm radius spot for the laser mode on the SDL device as shown in Fig 4.3. The mirrors used for the cavity were designed to be highly reflective around 1200 nm. The insertion of the birefringent (BRF) filter at Brewster's angle[8] enabled tuning of the laser emission centred around 1215 nm with a tuning range of 34 nm as can be seen in Fig 4.4. The input to output power slope efficiency of 7.2 % was achieved for a 2 % output coupler and a maximum output power of nearly 650 mW was obtained. In Fig 4.5 the incident to output power transfers characteristics are reported. As can be seen, thermal rollover sets
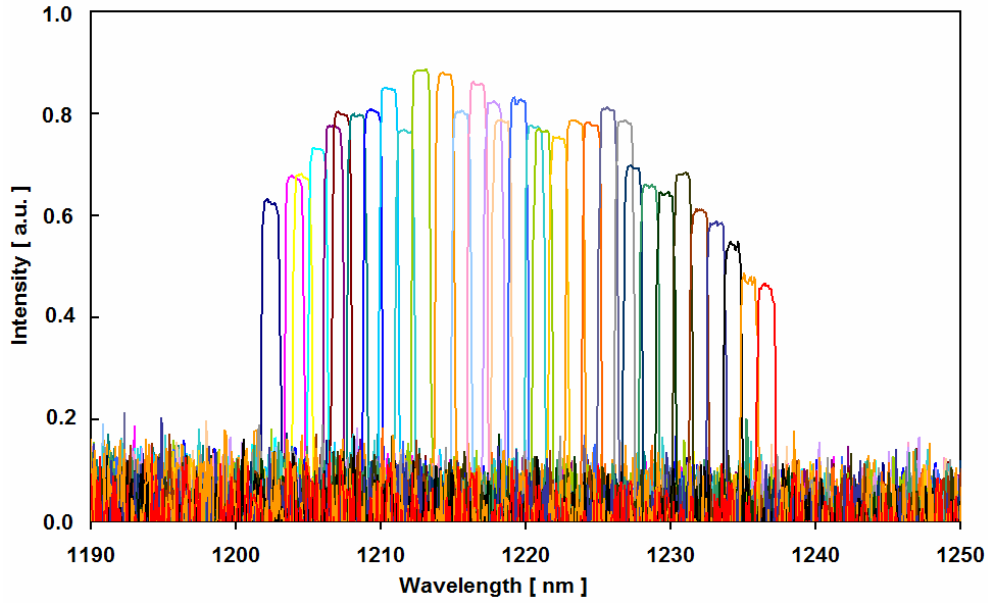
in around 9 W of incident power.

Fig 4.4 The tuning of the V-cavity as obtained in Strathclyde University with the rotation of the custom-designed birefringent filter BRF for the 2 % OC.
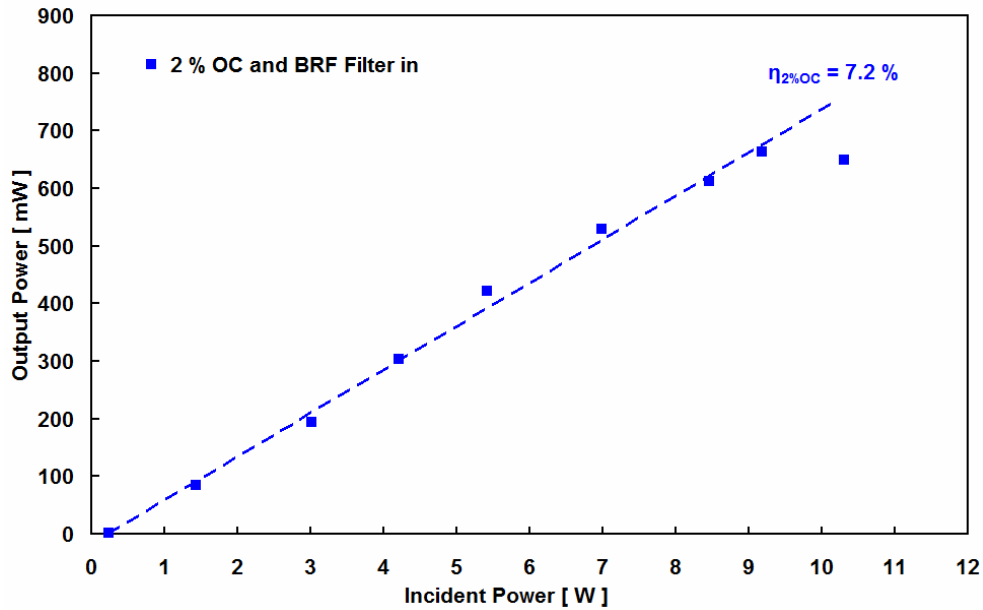

Fig 4.5 The Slope efficiency of the SDL pumped at 808 nm with a 2 % output coupler OC and a birefringent filter inserted in the cavity.

Beam quality measurements carried out on the SDL laser at its maximum output power revealed an M^2 of 2.1 in both sagittal and tangential planes. The good output power and beam quality were exploited to pump the Tellurite glasses as it is reported in the following sections and the results were published in Optical Materials[9].

4.3 Tellurite glasses pumped at 1200 nm

4.3.1 Singly doped Tm^{3+} Tellurite glass lasers

The 2.0 wt% Tm^{3+}-doped $Tm_{2.0}$:TZNG was selected among the samples of Table 3.1 as it demonstrated the best lasing characteristics when pumped at 793 nm. The SDL laser exciting the $^3H_5$ transition was tuned with the birefringent filter to the peak of absorption at 1211 nm and was focused with a 50 mm focal length lens to a beam spot radius of 25 µm. Almost 70 % of the incident radiation was absorbed by the gain element that was inserted in a V-type laser cavity, depicted in Fig. 4.6 that could sustain a stable mode spot size radius of 25 µm. The temperature of the thermo electric cooler was set at 15 °C.
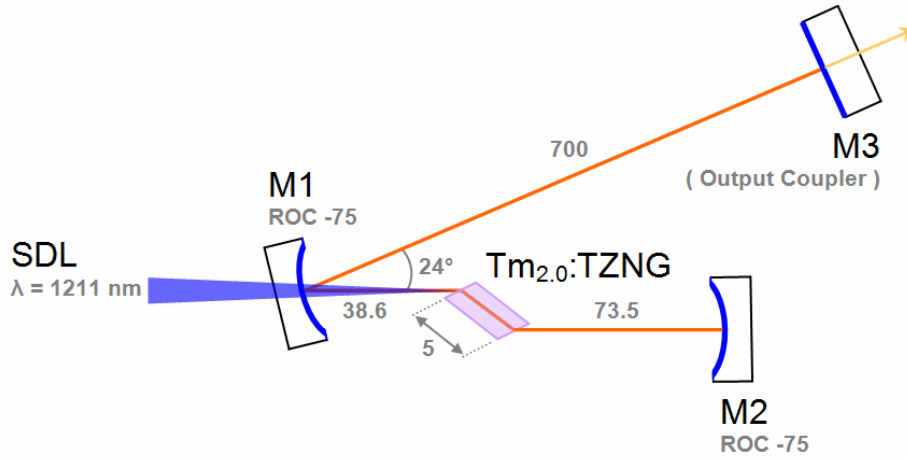

Fig 4.6 The V-folded laser resonator used for the $Tm_{2.0}$:TZNG sample pumped by the 1211 nm SDL source. All distances are reported in millimetres. The mode beam spot radius at the active material is of 25 µm.

The output laser radiation, centred around 1980 nm, was recorded with the three output couplers available and the absorbed to output power curves (internal efficiencies) recorded were of 22.4 %, 16.5 % and 9 % with the 4.1 %, 2.0 % and 0.8 % OCs respectively, and are shown in Fig 4.7. The maximum output power recorded with the 4.1% OC was of 60 mW with an incident power of 650 mW and the minimum threshold was found at an incident power of 149 mW with the 0.8% OC. It is interesting to notice that the curves do not show any onset of thermal rollover and that higher incident powers could have been used if available.

An intracavity birefringent crystal quartz plate (VLOC BF254-3T) was used to measure the tunability of the emitted laser radiation.
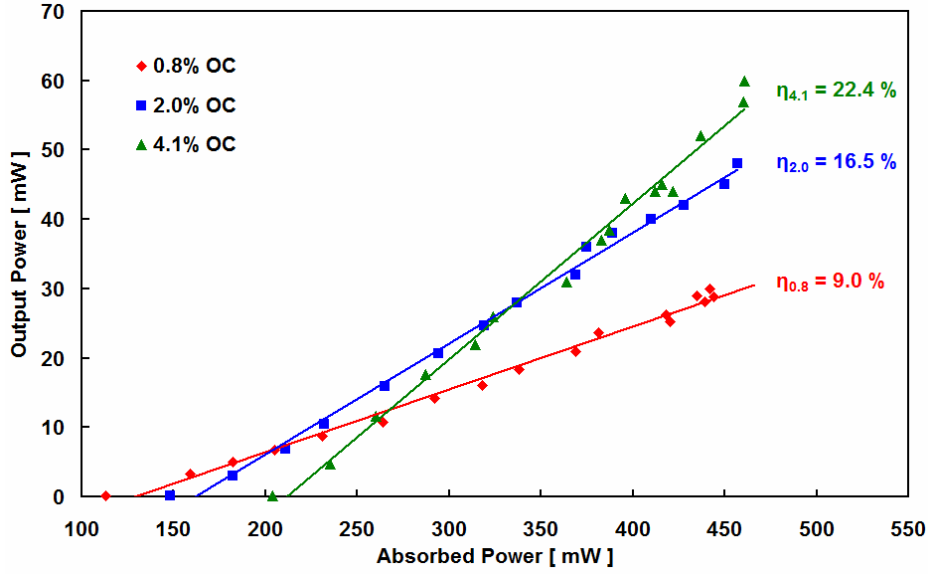

Fig 4.7 The absorbed to output power slope efficiencies of the tellurite sample $Tm_{2.0}$:TZNG doped at 2.0 wt% for three different output couplers when pumped at 1211 nm.

The results normalized to the maximum power are presented in Fig 4.8 for the three different output couplers. The broadest full width at half maximum value was recorded with an 0.8% OC and was of 115 nm continuously tuneable from 1850 nm to 2040 nm and centred around 1980 nm.
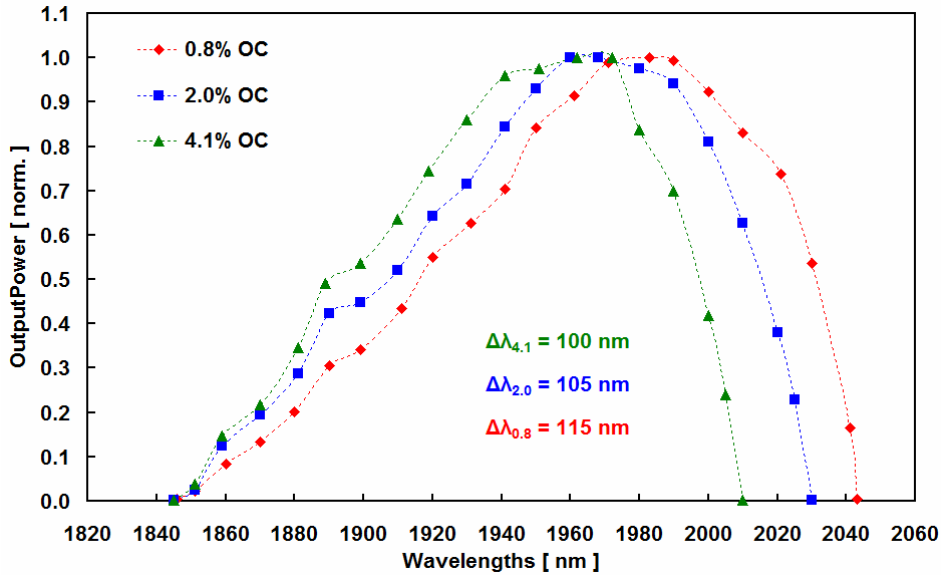

Fig 4.8 The tunability normalized to the maximum power of the tellurite sample $Tm_{2.0}$:TZNG doped at 2.0 wt% for three different output couplers when pumped at 1211 nm. The FWHM values are reported in the picture.

A loss analysis was carried out by plotting the inverse of the slope efficiencies against the inverse of the mirror transmissivities as discussed earlier in Chapter 3. The value obtained for η_0 was of 35.7 % and the scattering and impurities losses were of $\delta = 2.4\%$. If the losses at the high reflecting mirrors and at the Brewster's surfaces are factored in the total losses quoted per centimetre are: $\delta_{Tm2.0:TZNG} = 3.7$ %/cm.

4.3.2 Tm^{3+}-Ho^{3+} Tellurite glass lasers

The $^3H_5$ pump of Tm^{3+}-Ho^{3+} tellurite glasses was investigated with the $Tm_{2.0}$-$Ho_{0.2}$:TZN as the better performing $Tm_{2.0}$-$Ho_{0.1}$:TZN had not been fabricated at the time the 1200 nm SDL pump system was available. In an attempt to tackle the thermal lensing issues found in the experiments with a 793 nm pump, the $Tm_{2.0}$-$Ho_{0.2}$:TZN was this time Brewster cut to a length of 4.5 mm polished with a square cross section of 3 by 3 mm and wrapped in indium foil and cooled to 15 °C as can be seen in the inset of Fig 3.23. The sample absorbed nearly 70 % of the incident radiation that was tuned at 1213 nm and it was inserted on a V-cavity shown in Fig 4.9. As it was set up for the case of the singly Tm^{3+} doped samples the pumping beam was focused with a 50 mm lens down to 25 μm in radius and the laser resonator was in turn designed to be stable producing a 25 μm mode lasing radius.
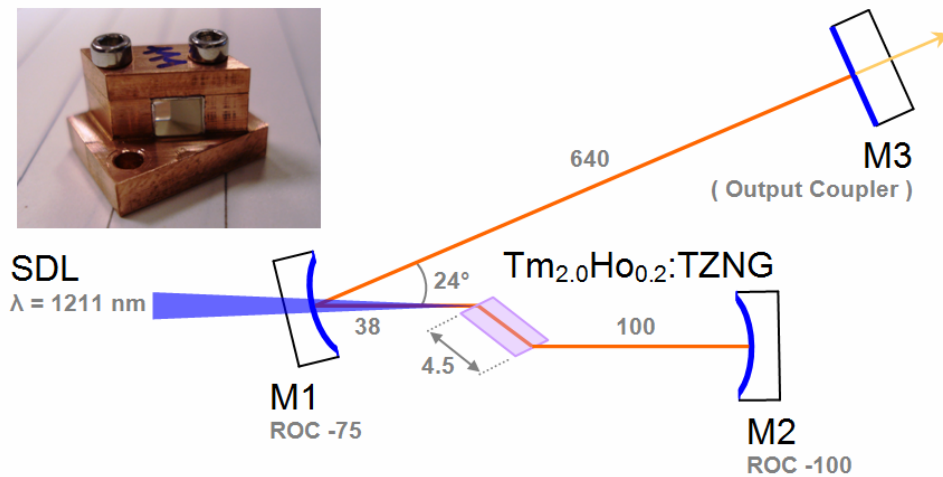

Fig 4.9 The laser resonator arrangement used for the test of the $Tm_{2.0}$-$Ho_{0.2}$:TZN. In the inset the picture of the sample as wrapped in Indium foil and inserted in the copper substrate. All measurements are reported in mm.

The output couplers used in this set of experiments were the usual 0.8 % and 2.0 % ones but also the high reflecting mirror which has a transmittance of around 0.1 % at the lasing wavelengths. The slope efficiencies recorded were then 1.3 %, 5.3 % and 7.2 % with the 0.1 %, 0.8 % and 2.0 % output couplers respectively, the three curves are reported in Fig 4.10. The incident power had to be limited to around 470 mW as strong thermal lensing effects would prevent lasing at higher powers. The maximum output power measured was of 11.5 mW with the 0.8 % OC while thresholds were 170 mW and 290 mW of incident powers with the 0.8 % and the 2.0 % OCs.
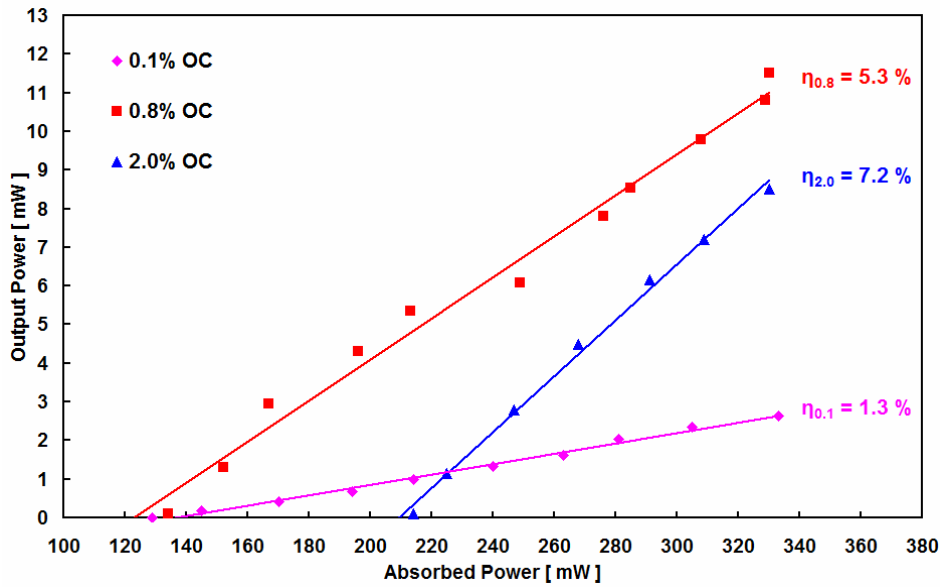

Fig 4.10 The absorbed to output power curves of the $Tm_{2.0}$-$Ho_{0.2}$:TZN when pumped at 1213 nm. The HR mirror, used as an output coupler, has a transmittance of 0.1 % at the lasing wavelengths.

As it was previously reported, the insertion of a birefringent plate would allow tuning of the emission wavelength. Tuning was smooth throughout the spectrum but the low gain of the material caused very narrow tuning ranges shown in Fig 4.11. The laser is tunable over the expected Ho^{3+} emission and centers at 2080 nm, 2065 nm, and 2060 nm for increasing transmittance of the OCs. Tuning is limited by the mirror losses on short wavelengths side and by the reabsorption losses on the longer wavelength side and has a maximum full width at half maximum of 35 nm.
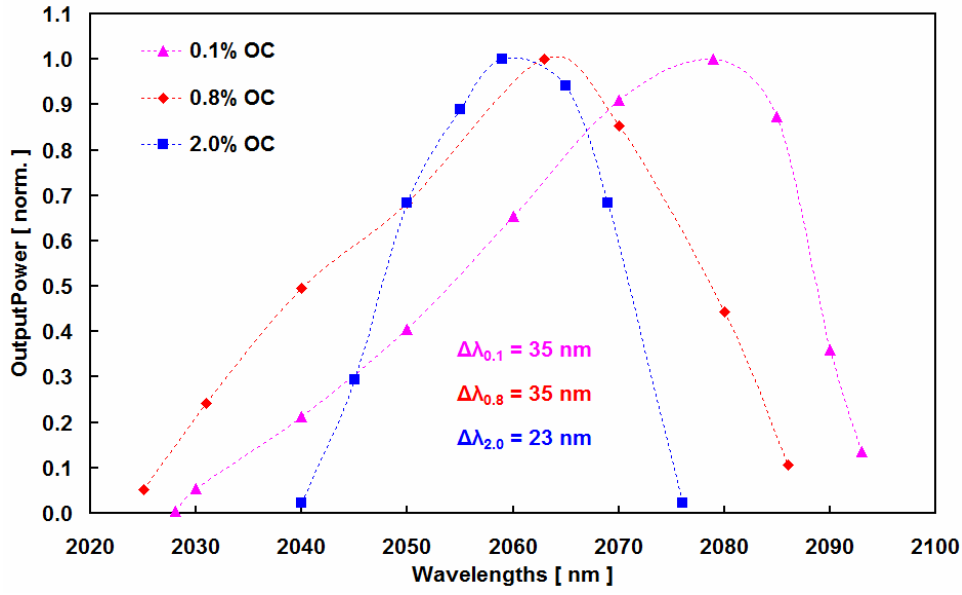
Fig 4.11 The graph of the tunability normalized to the maximum power for the $Tm_{2.0}$-$Ho_{0.2}$:TZN when pumped at 1213 nm. The FWHM values are reported on the graph.
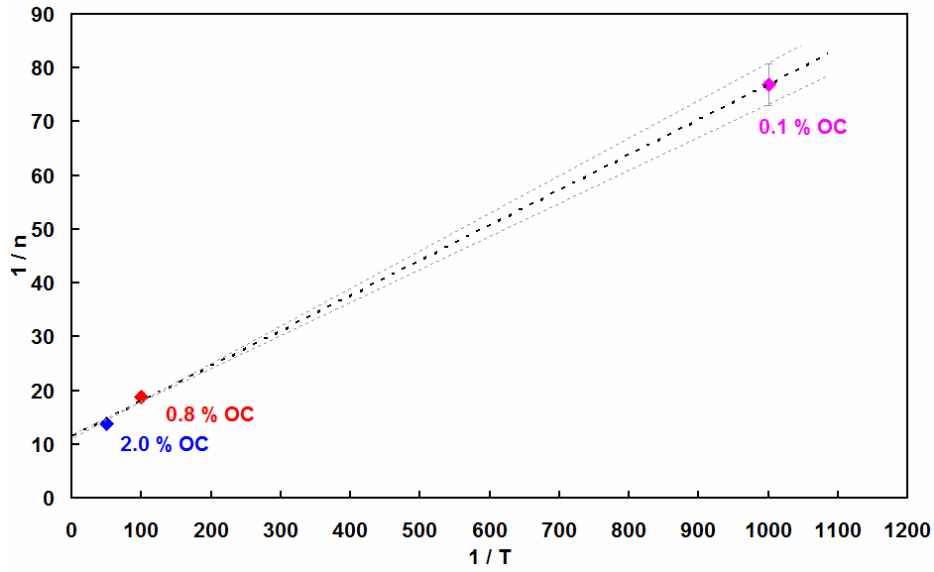

Fig 4.12 The inverse of the slope efficiencies plotted against the inverse of the transmittances for the $Tm_{2.0}$-$Ho_{0.2}$:TZN when pumped at 1213 nm. The two error lines account for a 5 % variation on the $1/\eta$ value at 0.1 % OC.

The performance characteristic analysis is reported in Fig 4.12. The value of η_0 is then 8.7 % and the losses are $\delta = 0.6$ %. If the losses at the high reflecting mirrors and at the Brewster's surfaces, totalling 0.5 %, are factored in the overall scattering and impurities losses quoted per centimetre are: $\delta_{Tm2.0Ho0.2:TZN} = 0.16$ %/cm. Losses are very small in this glass sample but the difference between the OCs is of one order of magnitude and

this plays a major role on the experimental error. As it is shown in Fig 4.12 in fact, a 5 % variation on the values of the slope efficiency as measured for the 0.1 % output coupler propagates to a ~ 60 % variation on the %/cm value of 0.16 %/cm.

4.4 Comparisons of pumping schemes

4.4.1 Comparison of pumping schemes in Tm^{3+} doped tellurite samples

In section 4.3 the performance characteristics of the $Tm_{2.0}$:TZNG glass element pumped by an SDL system at 1211 nm were presented. The results were published in Optical Materials[9] and it is interesting to compare them with the 793 nm Ti:Sapphire pumping reported in section 3.2 on the same gain media. In both cases the laser performance characteristics were recorded under the same environmental settings, the temperature of the sample was kept at 15 ºC and the same set of mirrors and output couplers were employed. Table 4.1 summarizes the relevant parameters of comparison.

Pump λ [nm]	Sample codes	Tm^{3+} conc. [wt%]	Host	η at 4.1% OC [%]	Max P_{OUT} [mW]	Min P_{TH} [mW]	Spectrum $\Delta\lambda_{FWHM}$ [nm]	η_0 [%]	δ [%/cm]
793	$Tm_{2.0}$:TZNG	2.0	TZNG	25.6	115	134	135	35	2
1211	$Tm_{2.0}$:TZNG	2.0	TZNG	22.4	60	149	115	36	3.7

Tab 4.1 The continuous wave laser performance characteristics and some spectroscopic parameters of the $Tm_{2.0}$:TZNG sample pumped at two different wavelengths.

The output to absorbed slope efficiency recorded with a 4 % OC was of 25.6 % and 22.4 % for the 793 nm and the 1211 nm pumping respectively. Similar laser threshold values are also found in the two cases. The net difference around 3 % between the efficiencies of the two lasers is low and confirms that excitation of the $^3H_5$ level of thulium via 1200 nm radiation for this Tm^{3+} concentration in this tellurite glass is comparable to $^3H_4$ Ti:Sapphire pumping[10]. The two different values of $\delta_{793nm} = 2$ % and $\delta_{1211nm} = 3.7$ % that were found were probably due to the fact that different spots of the same glass sample may be not homogeneous in quality. It is also interesting to give an explanation of the energy transfer mechanisms that come into play in the two cases.
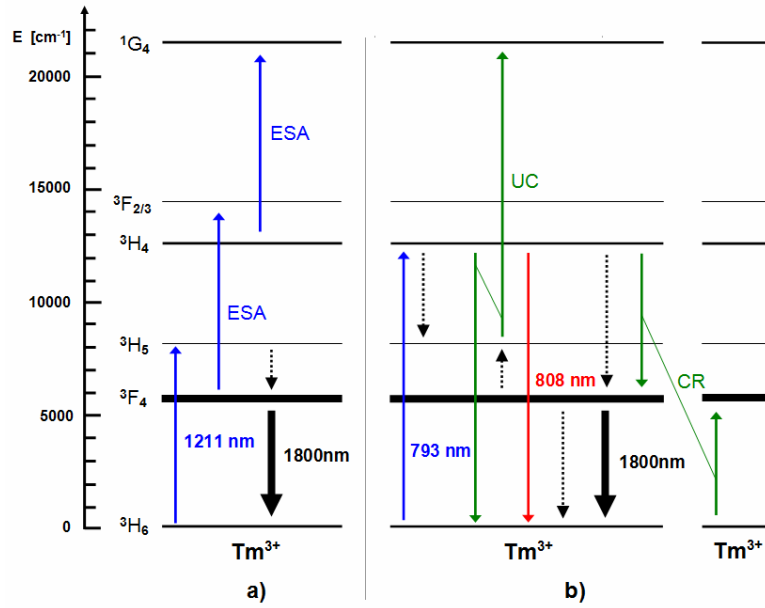
Fig 4.13. Simple Tm^{3+} Energy levels diagram. Continuous straight lines highlight the main transitions a) $^3H_5$ pumping and b) $^3H_4$ pumping. The main energy transfer mechanism involved are excited state absorption (ESA and UC) and cross-relaxation (CR). Dashed lines indicate phonon assisted transitions, nonradiative energy transfer.

Parameters strongly connected to the host-dopant combination and common to all types of excitations are the lifetimes of the energy levels and branching rations of the radiative transitions. In section 2.5.1 the luminescence lifetimes of the $^3F_4$ and of the $^3H_4$ were measured as 1.3 ms and 319 μs respectively. The two levels were highlighted accordingly to their lifetimes in Fig 4.13. The *radiative* branching ratios of the $^3H_4$ level on similar Tellurite based glass[11] shows that almost 90 % of the radiating ions excited in $^3H_4$ will radiatively relax to ground, ~8 % would relax to $^3F_4$ and ~2 % would relax to $^3H_5$. As it was introduced in chapter 2, many parameters affect the performances of the $^3F_4 \rightarrow {}^3H_6$ laser transition and in this discussion a qualitative indication of the various radiative and nonradiative effects in the case of the two pump regimes is presented.

In the case of $^3H_5$ pumping of the Tm^{3+}:TZNG glass sample a blue upconversion signal was produced and its intensity appeared weaker during lasing and vice versa. This showed that the well known sequential excited state absorption ESA of three pump photons promoted ions to the $^1G_4$ at 480 nm, Fig. 4.13a, and that it was dependent on the population of level $^3F_4$. Out of all the ions excited to $^3H_5$ the vast majority of them would quickly relax to the lasing level in multi-phonon aided transition, some of them would upconvert to $^3H_4$ and ultimately to $^1G_4$ and a very tiny part promoted in $^3H_4$

would undergo cross-relaxation CR and populate the lasing level. Under this excitation the laser emission is less dependent on the cross-relaxation CR and therefore less dependent on the dopant concentration, the limiting factors are the ESA efficiency, the concentration quenching and the lifetime quenching described in chapter 2.

In the case of $^3H_4$ pumping of the glass the blue upconversion was inversely proportional to the laser output power and also a red radiation scattered from the pump could be seen. The energy step from $^3F_4$ to $^1G_4$ is 15280 cm^{-1} in this glass and corresponds to a 654 nm photon wavelength, while the energy step from $^3H_5$ to $^1G_4$ is 12580 cm^{-1} and corresponds to a 794 nm photon wavelength therefore it is thought that the blue upconversion to $^1G_4$ is taking place from the $^3H_5$ level via an upconversion mechanism UC. The population in $^3H_5$ would then be supplied either by multi-phonon relaxation from $^3H_4$ or phonon assisted transitions[12] from $^3F_4$ as shown in Fig. 4.13b. In steady state conditions most of the ions pumped in $^3H_4$ would nonradiatively relax to the lasing level $^3F_4$ or cross-relax to populate $^3F_4$ once again. A small part would upconvert to $^1G_4$ and or emit to the ground level $^3H_6$. Having the correct dopant concentration is paramount in $^3H_4$ pumping as the CR plays the major role in the overall efficiency of the laser. Since the CR is directly proportional to the concentration[13] a tradeoff needs to be found between the CR and the limiting factors such as upconversion, concentration quenching and lifetime quenching.

It would be important to define which of the two pumping schemes would perform best and this can only be done by extensive spectroscopy and laser characterisation of samples with different combination of hosts (changing the phonon energy ħω) and varying dopant concentration. The relative upconversion signal strengths would need to be quantified and that would require the design of an excitation setup where the pump wavelengths can be easily swapped and where the upconverted luminescence can be measured while the 2 μm laser is running. The upconversion signals in the Tm^{3+}:TZNG sample with both pump wavelengths were very weak for many reasons. The short lifetime of $^3H_4$ compared to the tens of milliseconds of lower doped samples would not favor the upconversion and in the case of the $^3H_5$ excitation the 1211 nm pump was almost completely off the excited absorption (ESA) spectra as measured by Jackson et al.[14].

4.4.2 Comparison of pumping schemes in Tm^{3+}-Ho^{3+} doped samples

Performance characteristics of the $Tm_{2.0}$-$Ho_{0.2}$:TZN glass pumped at 793 nm were investigated and presented in section 3.3. The thermal lensing in that case was detrimental and the measurements had to be carried out with the aid of a 50:50 chopper. In order to improve the measurements and tackle the thermal lensing when pumping at 1213 nm the sample was Brewster cut and cooled on four side surfaces by wrapping in Indium foil and mounting on a cooled copper substrate. The thermal performances improved and the 50:50 chopper could be avoided, the results were presented in section 4.3.2 however it is very difficult to compare the characteristics as thermal effects heavily impinge on them. It is nonetheless important to describe how the 1213 nm pump may represent a better solution to counteract the upconversion losses. It can clearly be noticed, in comparison against 793 nm pumping depicted in Chapter 3 Fig 3.13, that the cross relaxation CR does not play an important role in 1213 nm pumping anymore and that the upconversion mechanism UC2 that acted to populate $^5F_3$ is not relevant as the $^3H_4$ level is no longer directly populated by the exciting photons.
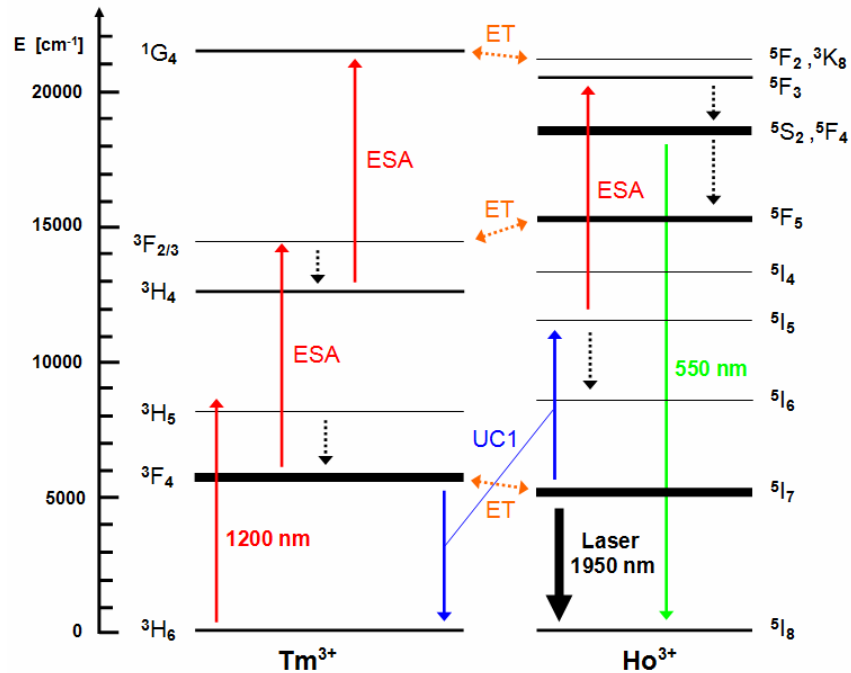

Fig 4.14 Tm^{3+}-Ho^{3+} Energy levels diagram when pumped at 1213 nm. Continuous straight lines highlight the main radiative transitions. The main energy transfer mechanisms involved are upconversion (UC1), excited state absorption (ESA) and energy transfers (ET). Dashed lines indicate phonon assisted transitions and nonradiative energy transfer. The energy levels are weighed according to their radiative lifetime[15].

The majority of photons that reach the green emitting $^5S_2$ are then brought by energy transfers ET from $^1G_4$ that is in turn populated by subsequent ESA in the Tm^{3+} system and by UC1 and ESA from $^5I_5$ that get to $^5F_3$ and then finally nonradiatively relax to $^5S_2$. The processes are less efficient than the direct upconversion UC2 experienced in the 793 nm systems and the green emission is visibly less strong. In order to confirm the substantial difference once again measurements should be organised with coaxial pump systems at 793 and 1213 nm and the necessary optics to collect the green fluorescence during lasing conditions.

4.5 Conclusions and comments

Two Tellurite glass samples doped with different dopants concentrations and combinations were tested under 1200 nm pumping by a SDL laser system. It was the first time that an SDL at such wavelength was used as a pump source for an end-pumped bulk system, the results were published in Optical Materials[9].

Both systems were compared against their same performance characteristics when pumped by Ti:Sapphire at 793 nm. The singly doped Tm^{3+} tellurite TZNG showed that 1200 nm pumping is competitive to $^3H_4$ pumping in this sample with this particular concentration value and this size. It is important to notice at this stage that different concentration values would have changed the comparative results, it was therefore highlighted in section 4.4 that further measurements would be necessary to fully characterize the energy transfer mechanisms that play significant roles in the two pumping systems. Such measurements would require the capacity of measuring the upconverted luminescence off the samples when pumped by one or the other wavelength and during lasing operations.

The results obtained with the 1200 nm pump were very promising, however the system was returned to the IOP and the best 793 nm pumped glasses, fluorogermanate and telluride were selected for the ultrashort pulse characterization with the aid of the semiconductor saturable absorber mirror, SESAM. The results are presented in the next chapter.

4.6 References

[1] S. L. Vetter*, et al.*, "*Short-wavelength GaInNAs/GaAs semiconductor disk lasers*", Electronics Letters, **44**, pp. 1069-1070, (2008).

[2] M. D. Dawson*, et al. The Institute of Photonics at Strathclyde University*. URL: http://www.photonics.ac.uk

[3] N. Schulz*, et al.*, "*High-brightness long-wavelength semiconductor disk lasers*", Laser & Photonics Reviews, **2**, pp. 160-181, (2008).

[4] A. C. Tropper*, et al.*, "*Vertical-external-cavity semiconductor lasers*", Journal of Physics D-Applied Physics, **37**, pp. R75-R85, (2004).

[5] Z. L. Liau, "*Semiconductor wafer bonding via liquid capillarity*", Applied Physics Letters, **77**, pp. 651-653, (2000).

[6] D. E. Aspnes*, et al.*, "*Optical-Properties of $Al_xGa_{1-x}As$*", Journal of Applied Physics, **60**, pp. 754-767, (1986).

[7] S. Ben Bouzid*, et al.*, "*Effect of nitrogen in the electronic structure of GaAsN and GaInAs(N) compounds grown by molecular beam epitaxy*", Materials Science and Engineering B-Solid State Materials for Advanced Technology, **112**, pp. 64-68, (2004).

[8] A. L. Bloom, "*Modes of a Laser Resonator Containing Tilted Birefringent Plates*", Journal of the Optical Society of America, **64**, pp. 447-452, (1974).

[9] F. Fusari*, et al.*, "*Tunable laser operation of a Tm^{3+}-doped tellurite glass laser near 2 μm pumped by a 1211 nm semiconductor disk laser*", Optical Materials, **32**, pp. 1007-1010, (2010).

[10] S. D. Jackson, "*Efficient Tm^{3+}, Ho^{3+}-co-doped silica fibre laser diode pumped at 1150 nm*", Optics Communications, **281**, pp. 3837-3840, (2008).

[11] R. Balda*, et al.*, "*Spectroscopy and concentration quenching of the infrared emissions in Tm3+-doped TeO2-TiO2-Nb2O5 glass*", Optics Express, **15**, pp. 6750-6761, (2007).

[12] T. Miyakawa and D. L. Dexter, "*Phonon Sidebands, Multiphonon Relaxation of Excited States, and Phonon-Assisted Energy Transfer between Ions in Solids*", Physical Review B, **1**, pp. 2961-&, (1970).

[13] F. Cornacchia*, et al.*, "*2 μm lasers with fluoride crystals: Research and development*", Progress in Quantum Electronics, **33**, pp. 61-109, (2009).

[14] S. D. Jackson and T. A. King, "*Theoretical modeling of Tm-doped silica fiber lasers*", Journal of Lightwave Technology, **17**, pp. 948-956, (1999).

[15] G. H. Dieke and H. M. Crosswhite, "*The Spectra of the Doubly and Triply Ionized Rare Earths*", Applied Optics, **2**, pp. 675-686, (1963).

5. CW-MODELOCKED FEMTOSECOND 2 µm GLASS LASERS

5.1 Introduction and chapter synopsis

In Chapters 3 and 4 the continuous wave laser characterisations of the bulk glass laser systems developed in this thesis were reported. In this chapter the continuous wave mode locked (CWML) pulsed regimes, for the Tm^{3+} doped fluorogermanate and the Tm^{3+}-Ho^{3+} doped tellurite systems are presented.

The aim of the work carried out during the course of this PhD was to demonstrate femtosecond pulse operations in bulk glass lasers at around 2 µm. The advantages of such result were explained in Chapter 1 and in this chapter the overall femtosecond results are presented. The technique used for the modelocking of the glasses is a well known method in ultrafast laser technology and it was briefly introduced in Chapter 1. Semiconductor saturable absorber mirrors SESAM were deployed inside the laser cavities with optimised geometries to obtain the shortest pulses and the maximum output powers. In section 5.2, the manufacturing of the SESAM used and its consequent post-processing is explained in detail. The deployment of the SESAM in laser cavities is reported in sections 5.3 and 5.4 for the fluorogermanate and the tellurite compounds respectively. Pulses as short as 410 fs at 2 µm are demonstrated in the case of the

Tm^{3+}:GPNG fluorogermanate glass. In the concluding section, 5.6, the overall results obtained are compared.

5.2 SESAM for modelocking 2 μm lasers

5.2.1 Structure of the SESAM

The SESAM used in this research was produced and supplied by Dr J. A. Gupta from the Institute for Microstructural Sciences at the National Research Council of Canada[1].
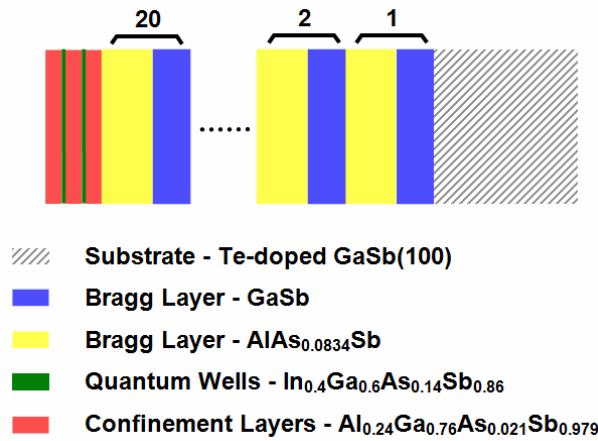

Fig 5.1 The structure of the SESAM used for modelocking of the laser, the quantum wells along with the Bragg Stack various layers are represented.

The structure of the saturable absorber comprises of two absorbing quantum wells grown on top of a Bragg stack mirror as illustrated in fig 5.1. The substrate chosen for the structure was a 500 μm thick Te-doped GaSb(100). The Bragg reflector structure comprises of 20 pairs of 128.65 nm thick (λ/4) GaSb and 154.52 nm thick (λ/4) AlAs$_{0.0834}$Sb layers and the reflectivity of the Bragg structure was of 99.9 % - 98.2 % in the 1960 to 2125 nm spectral range which is reported in fig 5.8. The two quantum wells were composed of 5.5 nm thick layers of In$_{0.4}$Ga$_{0.6}$As$_{0.14}$Sb$_{0.86}$ with separating layers of 20 nm thick Al$_{0.24}$Ga$_{0.76}$As$_{0.021}$Sb$_{0.979}$ layer surrounded by the same material. The quantum wells had photoluminescence peaks around 2100 nm and 2145 nm, fig 5.2. The peak in the emission spectrum at 2145 nm can be attributed to the quantum wells photoluminescence enhanced by the end of the mirror stopband. The measured modulation depths of the structure as manufactured were around 0.8 % and the recovery

time approximately 100 ps. The long recovery time caused relatively long pulse durations around 3.3 ps when the SESAM was used in a Tm,Ho:KYW laser[1]. It was then decided to use ion implantation to reduce the recovery time.
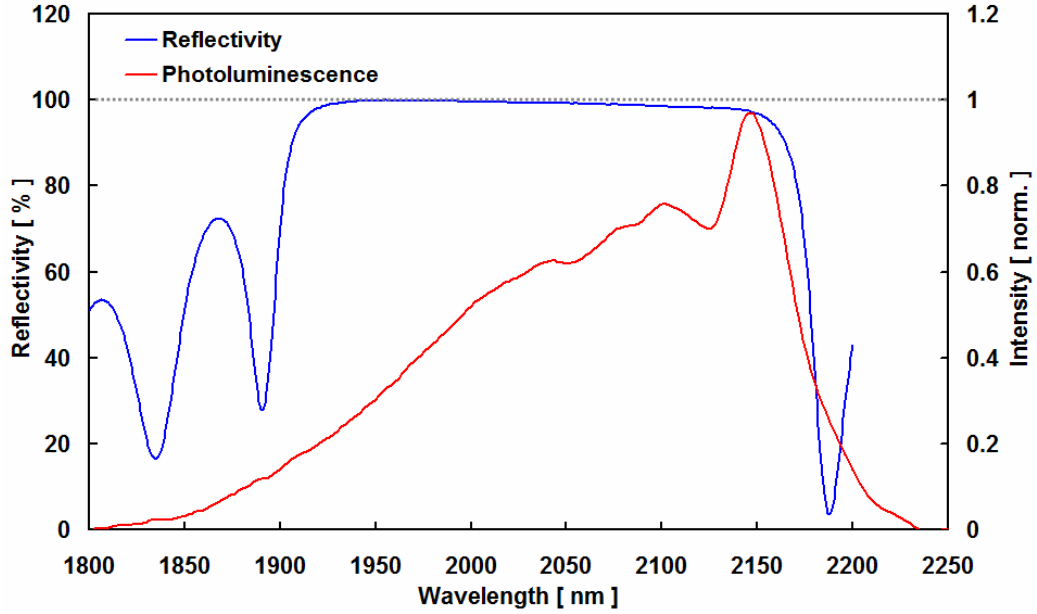

Fig 5.2 The reflectivity and the photoluminescence spectra of the SESAM structure as manufactured and used for modelocking of the glass materials.

5.2.2 As$^+$ Ion implantation

Ion implantation is a common technique in semiconductor technology as it allows post process doping of semiconducting layers. The technique is also used for lifetime engineering and this is the topic of this paragraph. In fact, in order to reduce the free electrons recombination time it has been shown[2] that the creation of defects, also called *recombination centres*, by ions or proton bombardment is effective without changing their density in the QW[3]. Our SESAM was irradiated with 4 MeV As$^+$ ions[4] with different dosages, the reflectivity spectrum of the implanted device is shown in fig 5.11. The implanted ions unfortunately also damage the Bragg reflector and cause an increase of the nonsaturable losses on the SESAM as it is evident by the overall reduction in reflectivity shown in fig 5.3 as the implantation dose increases. The recovery time of the implanted device was not measured as a pump-probe experiment would be needed to create the excitons and then measure their recombination time. However the proof of the effective change was given when the glass lasers could be

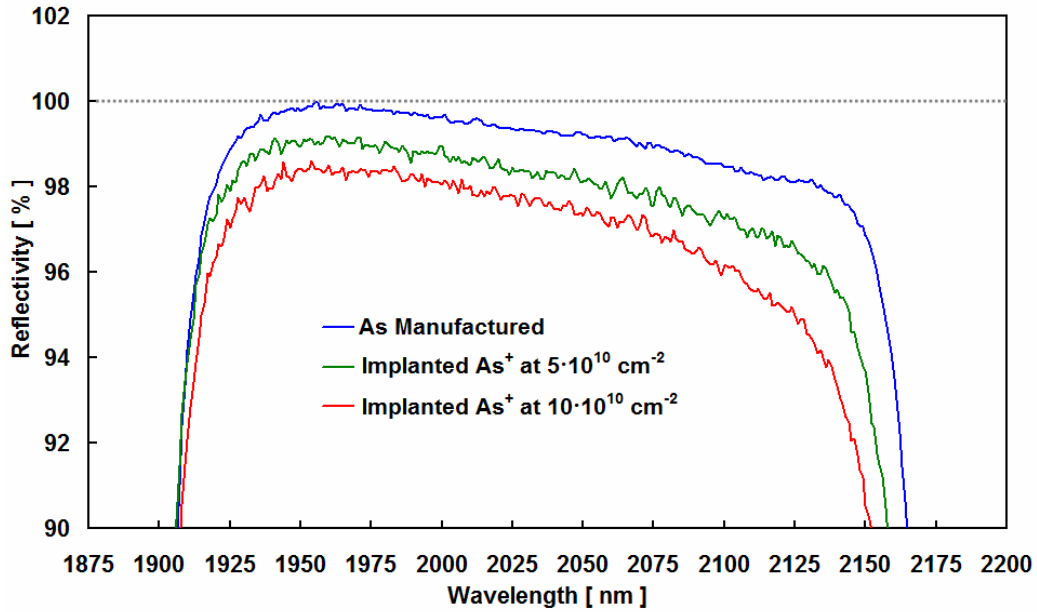modelocked and short pulses obtained with the implanted SESAM as it is presented in the next sections.

Fig 5.3 The reflectivity of the SESAM structure implanted with a dosage of $5 \cdot 10^{10}$ cm^{-2} As$^+$ ions, the blue line represents the reflectivity of the original as manufactured structure.

5.3 Modelocking of Tm^{3+}:GPNG fluorogermanate bulk glass lasers

The SESAM, implanted with an ion dose of $5 \cdot 10^{10}$ cm^{-2}, was glued to one of the end high reflecting mirrors of a Z-folded cavity, fig 5.12. The mirror, M4 was mounted on a linear translation stage so that the high reflector and the SESAM positions could be easily swapped. Two infrared grade fused silica prisms with a tip angle of 55°13´ were inserted on linear translation stages about their symmetry axis and inserted at minimum deviation angle to form the dispersion compensation system, as introduced in Chapter 1. The insertion losses were negligible in the laser system. Once the SESAM was inserted and modelocking was stabilised the cavity had to be optimised to produce the most stable and shortest pulses possible. The pump and mode spot size had to be adjusted in conjunction with the tip-to-tip distance d_{TTT} between the prisms therefore changing GVD in the cavity and negative dispersion respectively. The spot size on the short arm of the cavity and the output coupling mirror had to be optimised also to make sure the SESAM could operate in conditions of high saturation with fluencies of few times higher than the fluence threshold[5] but without reaching the damage threshold.
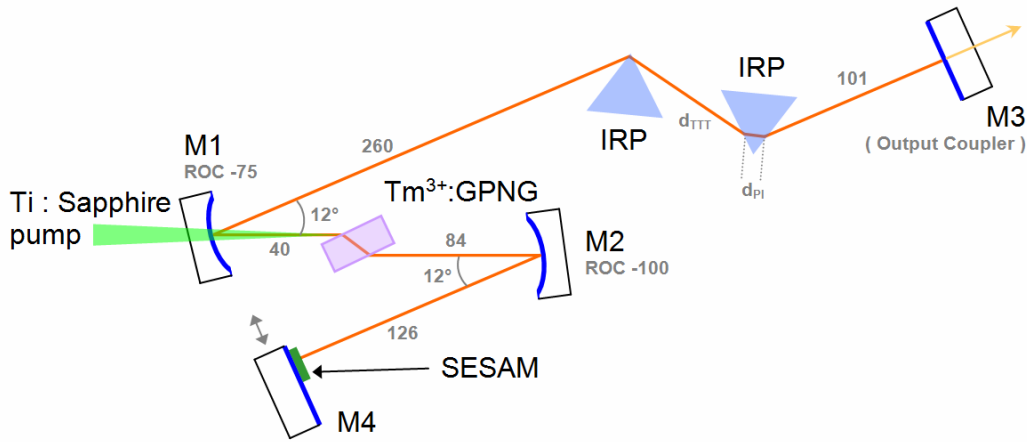
Fig 5.4 The cavity used in conjunction with the SESAM for the modelocking experiments with the Tm^{3+}:GPNG fluorogermanate sample. All distances are reported in mm. IRP – Infrared Prism, d_{TTT} = 59 mm tip-to-tip distance between prisms, d_{PI} – prism insertion distance

The laser in fig 5.4 represents the best performing cavity design. This design produced a 35 µm mode spot size radius on the active element and a 50 µm mode spot size radius on the SESAM. The values of the d_{TTT} and the output coupler were 59 mm and 0.8 % respectively. The Ti^{3+}:Sapphire pump beam was focused with an 80 mm focal length lens. The laser showed stable CWML behaviour by producing trains of pulses with a threshold of 37 mW of output power[6]. Pulses were self starting and very stable over long periods of time.
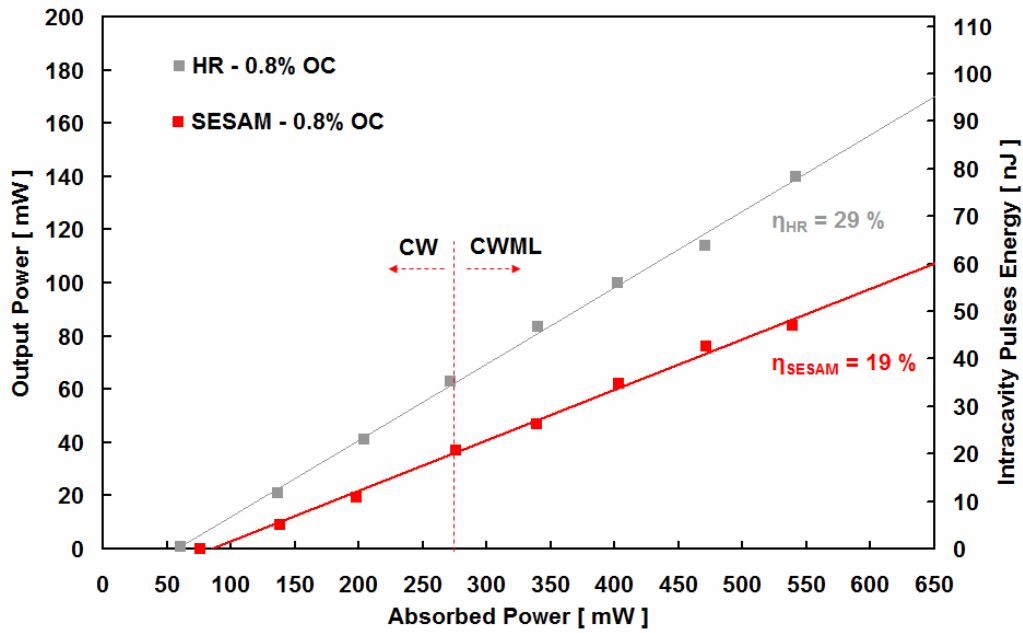

Fig 5.5 The absorbed to output power curves of the Tm^{3+}:GPNG fluorogermanate sample recorded with the SESAM inserted. The grey thin line represents the result with the HR in.

Fig 5.5 depicts the absorbed to output power graph obtained with the SESAM inserted giving a slope efficiency of 19 %. The second curve shows the operation of the laser with the HR mirror in replacing the SESAM. While laser threshold remains fairly similar in the two cases the difference in slope efficiencies is due to the nonsaturable losses of the SESAM. The RF spectrum of the pulses was measured with a resolution of 10 KHz and is depicted in fig 5.6, the value of υ_{REP} was 221.9 MHz. The train of pulses was very stable and there were no sign of Q-switching instabilities from threshold up to the maximum intracavity power.
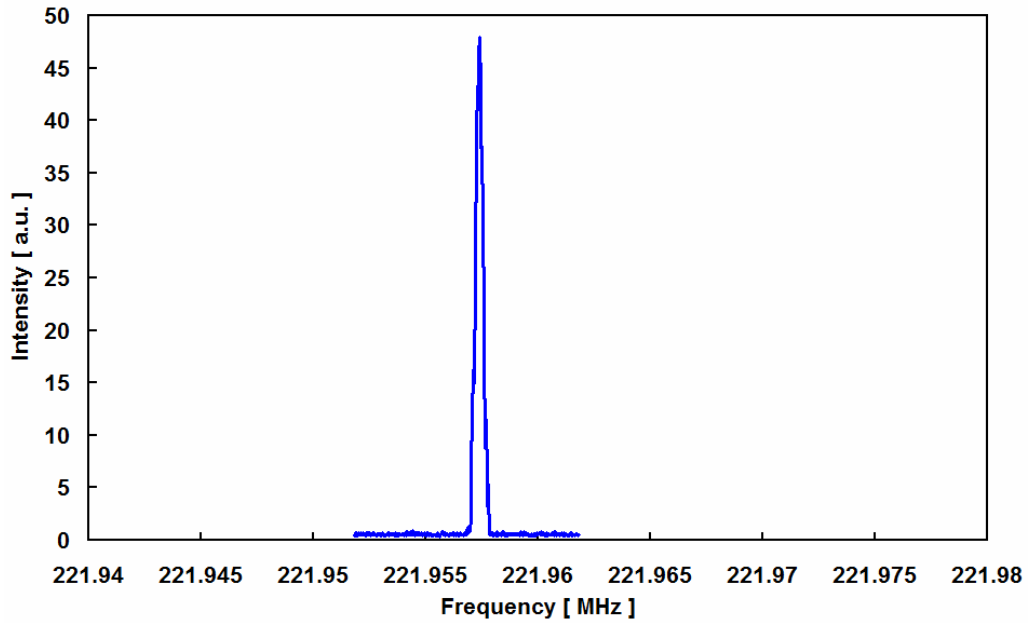

Fig 5.6 The RF spectrum of the signal detected with the InGaAs fast detector for the Tm^{3+}:GPNG laser with the SESAM inserted in the cavity.

With υ_{REP}, and the intracavity power at threshold P_{ITH} it was possible to calculate the intracavity pulse energy $E_P = P_{ITH} / \upsilon_{REP}$ and consequently the fluence at threshold $\phi_{th} = E_P / A$ where A is the area of the laser mode on the SESAM. $E_P = 21$ nJ and $\phi_{th} = 265$ $\mu J/cm^2$ if we repeat the calculation with the maximum output power we obtain a fluence on the SESAM of 602 $\mu J/cm^2$ that is over 2 times the fluence at threshold. Fig 5.5 reports the intracavity pulse energy on the right hand side axis. The fluorogermanate has a positive GVD of 280 fs^2/mm and has a length of 5.1 mm. The infrared fused silica prisms with GVD of -100 fs^2/mm around 2 µm, were inserted for $d_{PI} = 15$ mm into the cavity. Finally the two prisms with a d_{TTT} of 59 mm contributed to -2220 fs^2/mm of

second order dispersion calculated with formula (1.13) The total second order dispersion in the cavity D was of -2300 fs^2/mm.

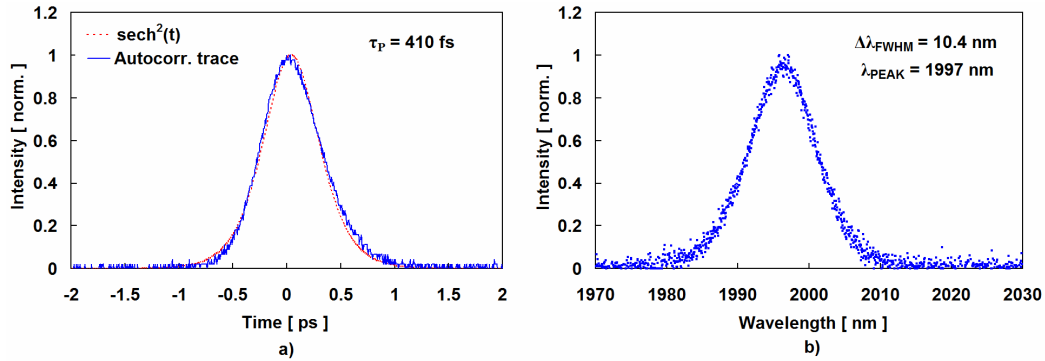Fig 5.7 The shortest pulses measured for the Tm^{3+}:GPNG, a) the autocorrelation trace with sech^2(t) overlapped and b) the optical spectrum recorded at the same time.

With the IAC system the pulse duration could be measured ranging from 600 fs to 410 fs, with optical FWHM spectra ranging from 8.1 nm to 10.4 nm respectively, centred around 1997 nm. The corresponding TBP ranged from 0.32 to 0.36. The pulse duration depended on the intracavity pulse energy as predicted by the soliton-like propagation model. In figure 5.7 the autocorrelation trace and optical spectrum of the shortest 410 fs pulses obtained are shown and the TBP was 0.32 showing the pulses were *transform limited*. The output power was 62 mW and the intracavity energy was 35 nJ/pulse. The intracavity peak power of 75 kW was calculated with $P_M = 0.88 \cdot E_P / \tau_P$[7].
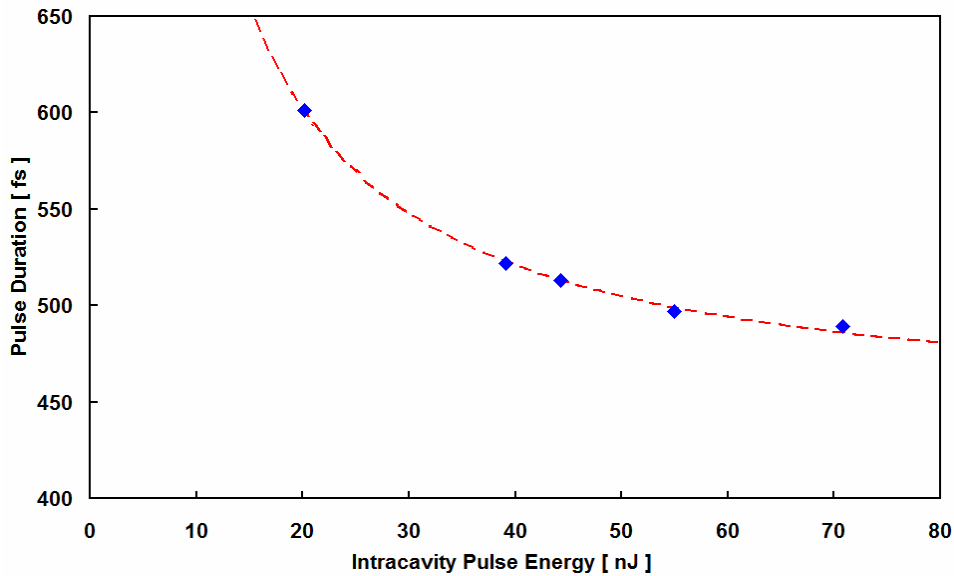

Fig 5.8 The pulses duration plotted vs. the pulses energies for the Tm^{3+}:GPNG during CWML regime of *soliton-like* propagation. The curve shows the best fit of the data with formula (1.18).

Fig 5.8 shows the curve obtained increasing the incident power on the laser element and the pulse duration is plotted against the intracavity energies. The curve follows the trend of formula (1.18) with $\rho_{KERR} = 2.51 \cdot 10^{-6}$ W^{-1}. The value for n_2 calculated with formula (1.20) was then $6.03 \cdot 10^{-15}$ cm^2/W which is slightly lower compared to the value of $9.5 \cdot 10^{-15}$ cm^2/W obtained in section 2.4.2. The difference may be due to the fact that the value obtained in section 2.4.2 was calculated with an empirical formula that was based on another rare earth ion in silica network. The performance obtained for the Tm^{3+}:GPNG laser during CWML operation are compared to that obtained for the Tm^{3+}-Ho^{3+}:TZN glasses in the section 5.5.

5.4 Modelocking of Tm^{3+}-Ho^{3+} tellurite bulk glass lasers

In this section the modelocked results obtained with the Tm^{3+}-Ho^{3+} tellurite sample are presented. Among all the doubly doped samples the Tm$_{2.0}$-Ho$_{0.1}$:TZN gave best CW results and was therefore selected for pulsed experiments. Once again after the SESAM was inserted and the first characterisations were conducted, the system had to be optimised and underwent three rounds of improvement finally yielding the results that are here reported.
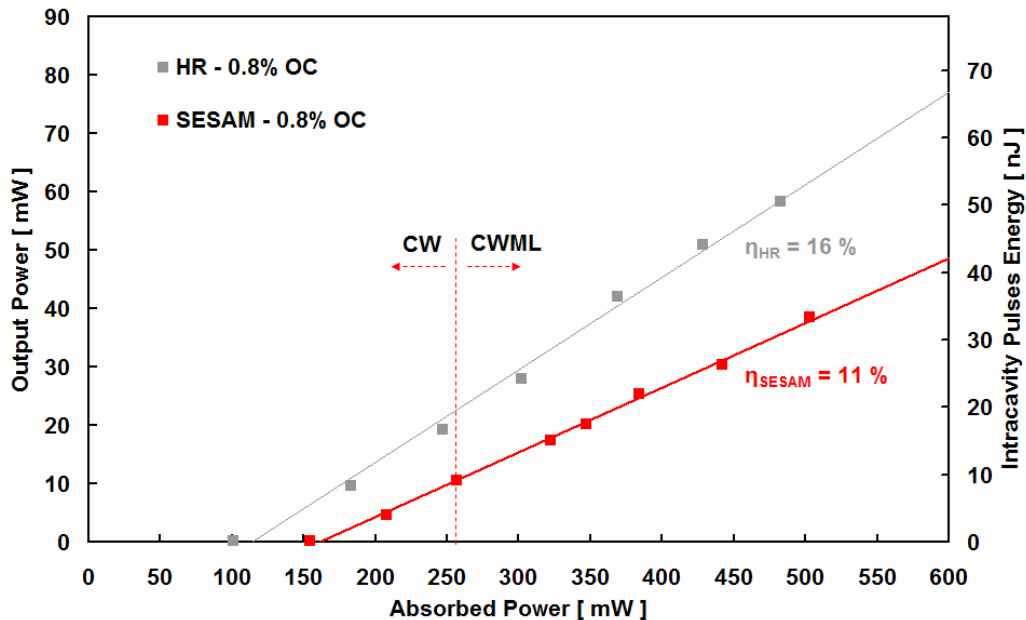

Fig 5.9 The absorbed to output power curves of the Tm$_{2.0}$-Ho$_{0.1}$:TZN tellurite sample recorded with the SESAM inserted. The grey thin line represents the result with the HR in.

The optimised cavity had the same cavity distances in Fig 5.4 on the short arm side but the long arm was 370 mm longer and its angle with the pump beam axis was of 16°. Fig 5.9 reports the absorbed to output power curves for the laser system when the HR mirror and the SESAM were inserted. The CWML regime had an output power threshold of 10.6 mW and emitted pulses up to 38 mW of output power centred around 2012 nm were obtained. Pulses were self-starting and very stable over many hours of operations. The pulse repetition frequency was 143 MHz and the intracavity pulses energies ranged from 9.2 nJ to 34 nJ as can be seen on the secondary axis of fig 5.15. The fluence at threshold could be calculated at ϕ_{th}=255 μJ/cm^2 similar to that found for the fluorogermanate case. The 5 mm long sample has a material positive dispersion at the emission wavelength of 2012 nm of 70 fs^2/mm. The system of prisms contributed with a total dispersion of -3700 fs^2/mm as their d_{TTT} was 59 mm and fused silica insertion in the laser was kept at 15 mm contributing to a total dispersion in the cavity of -3300 fs^2/mm. Pulses measured with the IAC were slightly longer in the case of the Tm^{3+}-Ho^{3+} sample ranging from 1010 fs to 630 fs with optical FWHM bandwidths from 4.2 nm to 6.8 nm respectively. The shortest pulses were transform-limited with a TBP of 0.32 and were produced with maximum average output power of 38 mW, fig 5.10 depicts the pulses autocorrelation trace and optical spectrum. Their intracavity energy was of 34 nJ with intracavity peak power of 47 kW.

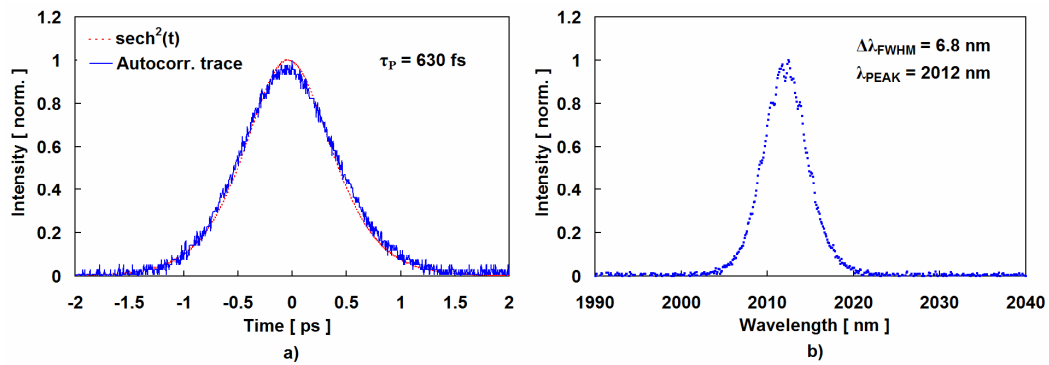

Fig 5.10 The shortest pulses measured for the $Tm_{2.0}$-$Ho_{0.1}$:TZN, a) the autocorrelation trace with sech^2(t) overlapped and b) the optical spectrum recorded at the same time.

Fig 5.11 shows a plot of pulse duration against intracavity energy. The trend fits well an hyperbolic curve (1.18) with parameter with $\rho_{KERR} = 2.33 \cdot 10^{-6}$ W^{-1}.
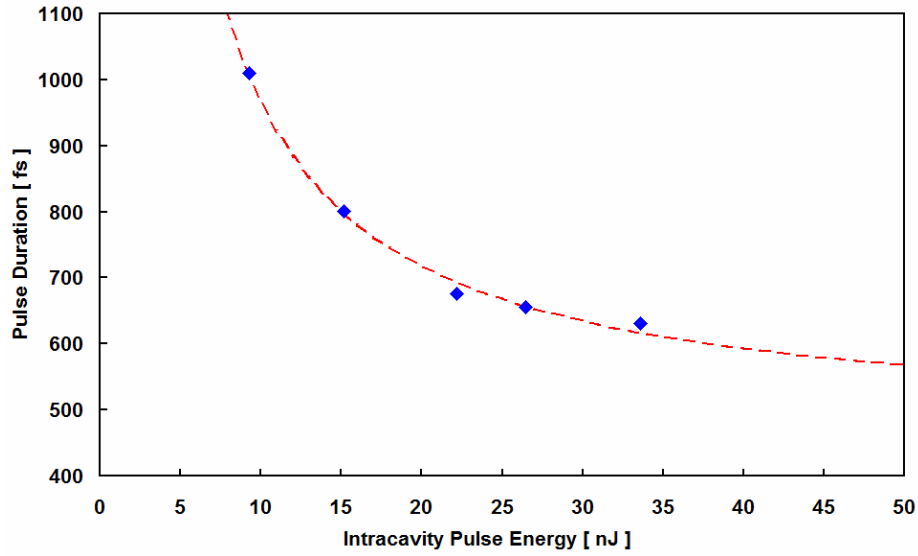
Fig 5.11 The pulses duration plotted against the intracavity pulses energies for the $Tm_{2.0}$-$Ho_{0.1}$:TZN during CWML regime of *soliton-like* propagation.

The value for n_2 calculated with formula (1.20) was then $2.93 \cdot 10^{-15}$ cm^2/W which is again lower compared to the value of $5.74 \cdot 10^{-15}$ cm^2/W obtained in section 2.4.1. This confirms the trend of formula (2.5) of overestimating the values of n_2 in the case of Tm^{3+} and Tm^{3+}-Ho^{3+} ions in fluorogermanate and tellurite networks.

5.5 Conclusions

In this chapter the CWML pulsed regimes of Tm^{3+} and Tm^{3+}-Ho^{3+} bulk fluorogermanate and tellurite glasses were investigated. In section 5.2 the basics of ultrafast phenomena were covered with particular attention to the infrared 2 μm systems. The characteristics of the linear and nonlinear propagation of the 2 μm femtosecond-long laser pulses into the transparent media within the laser cavity were introduced. Pulse formation was described with the use of SESAM mirrors implanted with As^+ ions in order to reduce the recovery time and the *quasi-soliton* propagation regime was explained. The measurement of the pulse duration was performed with an IAC that was custom-built for the 2 μm wavelength. The creation of ultrafast pulses is challenging as the second order dispersion had to be controlled with the well-known series of two infrared grade fused silica prisms. The two laser elements Tm^{3+}:GPNG and $Tm_{2.0}$-$Ho_{0.1}$:TZN were tested and produced transform-limited pulses with a duration

of 410 and 630 fs respectively around 2 μm with intracavity peak powers from 47 kW to 75 kW and the best pulse characteristics obtained are reported in table 5.1.

Sample codes	Dopants conc.		n_2	f_k	τ_P	λ	$\Delta\lambda$	TBP	υ_{REP}	E_P	P_M	ϕ_{SAT}
	Tm^{3+}	Ho^{3+}	[10^{-15} cm^2/W]	[mm]	[fs]	[nm]	[nm]	[nm]	[MHz]	[nJ]	[KW]	[μJ/cm^2]
Tm^{3+}:GPNG	2 wt%	-	6.03	2.0	410	1997	10.4	0.320	221.9	35	75	265
$Tm_{2.0}$-$Ho_{0.1}$:TZN	2 wt%	0.1 wt%	2.93	4.2	630	2012	6.8	0.320	143.0	34	47	255
Tm^{3+}:ZBLAN	2 mol%	-	0.24	51.1	-	-	-	-	-	-	-	-

Tab 5.1 The pulse characteristics for the shortest pulse durations obtained with the Tm^{3+}:GPNG and the $Tm_{2.0}$-$Ho_{0.1}$:TZN during CWML regimes.

Both laser systems operated in the negative second order dispersion regime with values of total D of -2300 fs^2/mm and of -3300 fs^2/mm for the Tm^{3+}:GPNG and $Tm_{2.0}$-$Ho_{0.1}$:TZN respectively and thus met the necessary condition for soliton creation[3].

As was explained the pulses are continuously shaped by the interplay between SPM and GVD and therefore are dependent not only on the modulation depth of the SESAM at the exact emission wavelength but also on the gain material characteristics. In this respect it has to be noted that the same SESAM was also tried in cavities with the Tm^{3+}:ZBLAN fluoride active material but no modelocking was observed. The reason is mainly due to two parameters, the lifetime of the lasing level in our fluoride compound is nearly twice the one in the other materials posing Q-switching instabilities problems[3] and also the n_2 is one order of magnitude smaller than the one found for fluorogermanate and tellurite networks. If we consider in fact that the SPM plays a great part in the shaping of the laser pulses we can compare the value of the equivalent Kerr lens focal length f_k for the three materials. If we set for instance the intracavity pulse energy at P_M = 50 kW and L = 5 mm with a laser mode radius w_L of 25 μm and n_2 calculated in Chapter 2 with the use of formula (1.16) in section 1.3.3 we obtain the values reported in Table 5.1. It can be clearly seen that the ZBLAN glass nonlinear response is very much weaker than the one found for the other network formers.

5.6 References

[1]   A. A. Lagatsky, *et al.*, "*Passive mode locking of a Tm,Ho:KY(WO₄)(₂) laser around 2 μm*", Optics Letters, **34**, pp. 2587-2589, (2009).

[2]   E. L. Delpon*, et al.*, "*Ultrafast excitonic saturable absorption in ion-implanted InGaAs/InAlAs multiple quantum wells*", Applied Physics Letters, **72**, pp. 759-761, (1998).

[3]   U. Keller*, et al.*, "*Semiconductor saturable absorber mirrors (SESAM's) for femtosecond to nanosecond pulse generation in solid-state lasers*", IEEE Journal of Selected Topics in Quantum Electronics, **2**, pp. 435-453, (1996).

[4]   J. W. Tomm*, et al.*, "*Properties of As$^+$-implanted and annealed GaAs and InGaAs quantum wells: Structural and band-structure modifications*", Journal of Applied Physics, **95**, pp. 1122-1126, (2004).

[5]   W. Koechner, *Solid-State Laser Engineering*, Sixth Edition ed.: Springer series in Optical Sciencies, 2006, Isbn: 0-387-29094-X.

[6]   F. Fusari*, et al.*, "*Femtosecond mode-locked Tm^{3+} and Tm^{3+}-Ho^{3+} doped 2 μm glass lasers*", Optics Express, **18**, pp. 22090-22098, (2010).

[7]   R. Paschotta, *Encyclopedia of Laser Physics and Technology*. Berlin: Wiley-VCH, 2008, Isbn: 978-3-527-40828-3.

6.   SUMMARY AND CONCLUSIONS

6.1 Thesis Summary

In this thesis, the development of Tm^{3+} and Tm^{3+}-Ho^{3+} doped bulk glass laser systems emitting at 2 µm in continuous wave (CW) and continuous wave modelocked regimes, (CWML) has been described. The use of two different optical pump sources, a traditional Ti:Sapphire system operating at 800 nm and a semiconductor disk laser emitting around 1.2 µm allowed the comparison of the results between the two different pumping schemes for the first time in bulk glass lasers.

At the beginning of this work considerable efforts were channelled on the research and development of glasses with physical characteristics and optical quality necessary for the deployment as active materials in free space CWML femtosecond laser cavities. Three families of glasses were examined. These were based on the Tellurite (TZN, TZNG), Fluorogermanate (GPNG) and Fluoride (ZBLAN) host matricies. The mechanical interaction with the host environment and the electronic interactions of the glassy networks of the trivalent *rare earths ions* as active ions were extensively studied and described in Chapter 2. Raman spectra were also recorded for the Tellurite and the Fluorogermanate compounds that provided some insight into the nano-structural features of the glasses. Most importantly spectroscopic performance characterisations

were carried out for the glasses doped with Tm^{3+} or Tm^{3+}-Ho^{3+} combinations. The results can be easily summarized in Table 6.1 below.

Sample codes	Tm^{3+} conc. [10^{20} ions/cm^3]	Peak Phonon Energy $\hbar\omega$ [cm^{-1}]	n_2 [10^{-15} cm^2/W]	Peak σ_E (1850 nm) [10^{-21} cm^2]	FOM [10^{-24} s·cm^2]
$Tm_{2.0}$:TZNG	3.35	790	5.74	5.3	6.9
Tm^{3+}:GPNG	3.10	890	9.5	5.6	16.2
Tm^{3+}:ZBLAN	3.56	500	0.24	2.5	11.5

Sample codes	Dopants Concentrations		Tm^{3+}/Ho^{3+} ratio	Peak σ_E (2010 nm)	FOM
	[10^{20} ions/cm^3]	[10^{20} cm^{-3}]	[.]	[10^{-21} cm^2]	[10^{-24} s·cm^2]
$Tm_{2.0}$-$Ho_{0.4}$:TZN	3.35	0.68	5	7.8	25.0
$Tm_{2.0}$-$Ho_{0.2}$:TZN	3.35	0.34	10	7.4	17.4
$Tm_{2.0}$-$Ho_{0.1}$:TZN	3.35	0.17	20	7.5	19.3

Tab 6.1 Mechanical and spectroscopic parameters for the Tm^{3+} and the Tm^{3+}-Ho^{3+} doped bulk glasses used in this research. Values are commented in the text.

In table 6.1 the three hosts are mechanically characterised by the three very different peak phonon energies that in turn impinge on the emission properties of the doping ions in the structures. The higher the peak phonon energies the lower the emission cross-sections. The emission cross sections are multiplied with the lifetimes, (not reported in table 6.1) to yield the figure of merit (FOM) that gives an indication of the potential of the materials to amplify the optical radiation and act as good laser elements for CW laser emission.

The nonlinear refractive index, n_2, provides an indication of the materials' capacity to generate and sustain femtosecond pulses. It is clear that the Tellurite and the Fluorogermanate represented the better choices for pulse generation. In the case of the doubly doped Tellurite samples the figure of merit topped at 25×10^{-24} s·cm^2 but the sample that showed the best performances was the one doped with 0.17×10^{-20} cm^3 where the Ho^{3+} emission was not self-quenched. The continuous wave characteristic performances of the different solid state 2 µm bulk glass based laser systems pumped with the Ti:Sapphire at 800 nm were then described in Chapter 3. The results are clearly presented in Figure 6.1 and Figure 6.2 shown below. The graphs compare the different

results obtained for the three main compounds treated. Figure 6.1 shows the absorbed to output power curves (internal efficiency) for the three samples: $Tm_{2.0}$:TZNG, Tm^{3+}:GPNG and Tm^{3+}:ZBLAN for the 0.8 % OC.
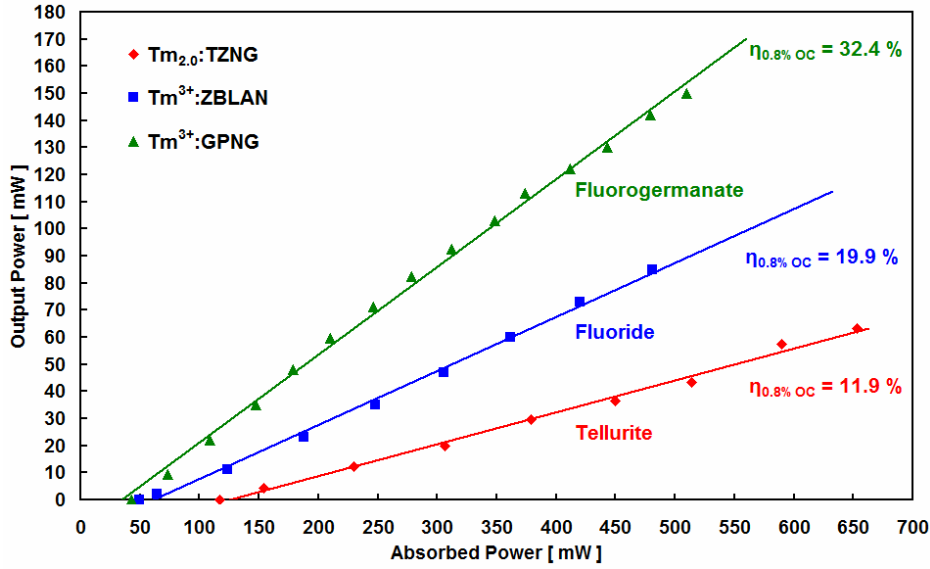
Fig 6.1 The absorbed to output power curves for the $Tm_{2.0}$:TZNG, Tm^{3+}:GPNG and Tm^{3+}:ZBLAN lasers tested during this PhD with the 0.8 % OC.

The superior laser characteristics of the fluorogermanate gain element were clear. The maximum internal efficiency obtained was of 50% and the maximum output power was of 190 mW limited by the incident power. The output powers associated with the GPNG sample were competitive with the values obtained for crystalline bulk lasers[1-2].
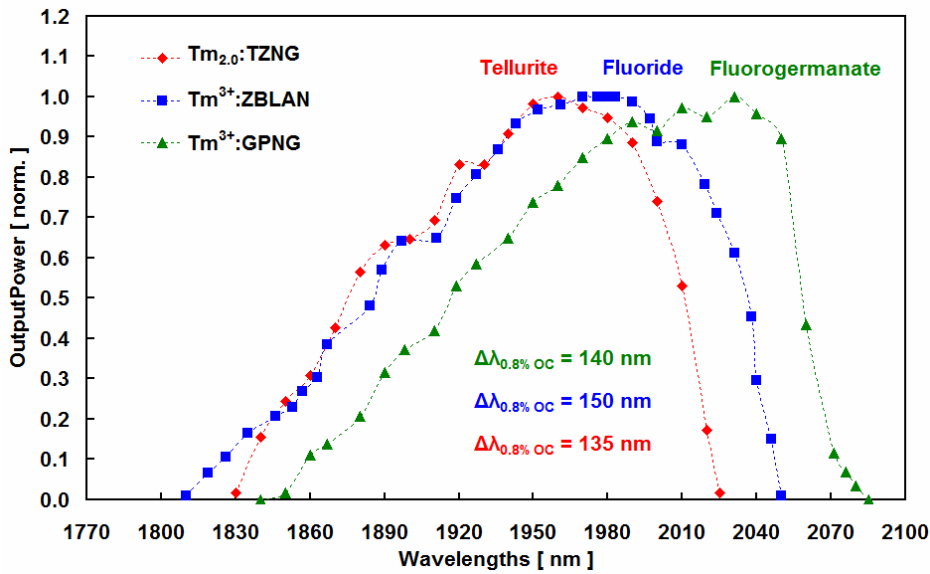

Fig 6.2 The tunability of the $Tm_{2.0}$:TZNG, Tm^{3+}:GPNG and Tm^{3+}:ZBLAN lasers tested in this thesis with the 0.8 % OC measured with the prism.

All active elements had stable output powers and provided for almost thermal lens free operation, however from a mechanical strength and chemical stability point of view germanium based oxyfluoride compounds were the most durable. Two of the tellurite glass samples doped with different dopant concentrations and combinations were also tested under the 1200 nm SDL pumping. This was the first time that an SDL at such wavelengths was used as a pump source for an end-pumped bulk system, the results were a maximum internal slope efficiency of 22.4% with a highest output power of 60 mW [3].

In chapter 5 the results obtained in CWML pulsed regimes of Tm^{3+} and Tm^{3+}-Ho^{3+} bulk fluorogermanate and tellurite glasses were presented. The two bulk glasses were modelocked with a SESAM that was implanted with As^+ ions in order to reduce the relaxation time[4-5]. The *quasi-soliton* propagation regime was explained and an estimation of the nonlinear refractive indices was provided. The measurement of the pulse duration was performed with an IAC that was custom-built for 2 µm wavelength. The two laser elements Tm^{3+}:GPNG and $Tm_{2.0}$-$Ho_{0.1}$:TZN were tested and produced transform-limited pulses with a duration of 410 and 630 fs respectively around 2 µm with intracavity peak powers from 47 kW to 75 kW and the best pulse characteristics obtained are reported in table 6.2.

Sample codes	Dopants conc.		τ_P	λ	$\Delta\lambda$	TBP
	Tm^{3+}	Ho^{3+}	[fs]	[nm]	[nm]	[nm]
Tm^{3+}:GPNG	2 wt%	-	410	1997	10.4	0.320
$Tm_{2.0}$-$Ho_{0.1}$:TZN	2 wt%	0.1 wt%	630	2012	6.8	0.320

Tab 6.2 The pulse characteristics for the shortest pulse durations obtained with the Tm^{3+}:GPNG and the $Tm_{2.0}$-$Ho_{0.1}$:TZN during CWML regimes.

Both laser systems operated in the negative second order dispersion regime with values of total D of -2300 fs^2/mm and of -3300 fs^2/mm for the Tm^{3+}:GPNG and $Tm_{2.0}$-$Ho_{0.1}$:TZN respectively and thus met the necessary condition for soliton creation[6]. Trains of pulses were propagating at 222 MHz in the case of Tm^{3+}:Fluorogermanate glass with a maximum average output power of 84 mW. Tm^{3+}-Ho^{3+}:TZN Tellurite compounds gave trains with a repetition rate of 143 MHz and a maximum averaged output power of 43 mW. The regime of propagation obtained was soliton-like and the

modelocking was self-starting. Fig 6.3 reports the two autocorrelation traces of the shortest pulses produced in the two cases.
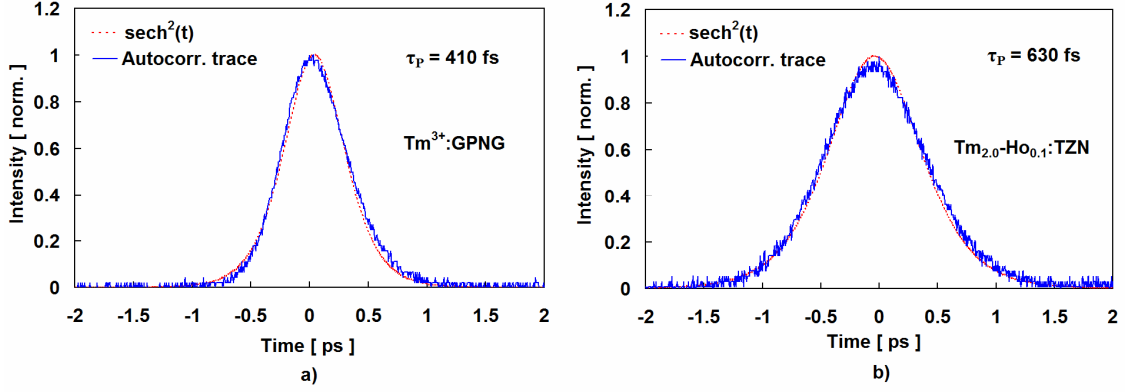

Fig 6.3 The autocorrelation traces recorded in the case of the a) Tm^{3+}:GPNG and b) $Tm_{2.0}$-$Ho_{0.1}$:TZN lasers tested with the SESAM implanted with As^+ ions.

No modelocking was observed in the Tm^{3+}:ZBLAN fluoride active material, the reason being mainly due to two parameters, the lifetime of the lasing level in our fluoride compound was nearly twice the one in the other materials posing Q-switching instabilities problems[6] and also the n_2 was found of one order of magnitude smaller than the one of fluorogermanate and tellurite networks.

This work showed that continuous wave modelocking and femtosecond-short trains of pulses in bulk glasses could be realised. These promising results open new ideas in the field of modelocked glass based lasers that will be briefly explored in the next section.

6.2 Future outlook

The results obtained demonstrated for the first time the successful use of bulk glasses as gain materials for laser generation at infrared wavelengths beyond the classic telecommunications wavelength of 1.5 µm. The relative advantage of working in such a range of wavelengths is the spectroscopical distance with the Rayleigh scattering. Emission and absorptions happen far from the UV cut off region of the glass and active materials tend to be very transparent. Among the current compositions the fluorogermanate glass proved to perform best however the first improvement that needs to be made is the substitution of the Lead fluoride with a less toxic and more environmentally friendly heavy ion fluoride such as LaF_3[7]. The composition and the

process obtained would then be at a stage where it could be commercialised. The system combined with diode pumps at 793 nm, could then be placed in the market as the first femtosecond laser source at 2 µm.

Another interesting research path is opened by the relative good saturated gain of the fluorogermanate glass and its mechanical properties. The material is in fact durable enough to be machined and to be used as a test bed for novel optical circuits and integrated optical amplifiers. Technology is moving fast towards optical memories and optical signal processing and there is the need of creating ultrafast compact switching devices. An attractive approach to this problem is the creation of waveguides in optical materials via a technique known as Ultrafast Laser Inscription (ULI). Trains of high energy ultrashort pulses are focused within the material causing local stresses and permanent modifications of the refractive index[8]. This can be exploited in the creation of waveguides and waveguide lasers in three dimensional inscribed structures. ULI capacity was present at the nonlinear research group of Prof Ajoy K Kar in Heriot Watt University in Edinburgh and with the aid of Dr Robert Thomson some waveguides were inscribed in the Tm^{3+} doped fluorogermanate glass.

ULI fabricated waveguide lasers were only demonstrated using Yb^{3+}, Nd^{3+} and Er^{3+} doped glass and crystal substrate materials[9] which provided lasing at centre wavelengths of 1.047 µm, 1.064 µm and 1.55 µm respectively[10], however the longest wavelength that had been demonstrated to have been successfully guided by a ULI fabricated waveguide was around 1.65 µm. As a final part of the work conducted then, tt was therefore interesting and challenging to see whether 2 µm light could be guided and amplified in such structures providing a proof or principal of their feasibility.

The fluorogermanate glass was cut to a length of 7 mm and polished to a plane-parallel finish as shown in Figure 6.4. 32 different waveguides were written on the material at different speeds and with different pulse energies through the multi-scan fabrication technique[11] in Heriot Watt University. 1.985 µm light generated by the Tm^{3+} fluorogermanate glass was observed to guide inside the laser modified regions and it took place in all written structures. In order to conduct the waveguide laser experiments, the sample was placed in a monolithic plane-plane laser cavity which consisted of dielectric mirrors that were directly butt-coupled against the polished waveguide facets. The input mirror had high transmission (> 98 %) at the pump

wavelength and high reflectivity (> 99.99 %) in the 1800-2100 nm range. Different output couplers were used with transmissions of 0.8 %, 2.0 %, 4.1 % and 10 % around 1.95 μm.
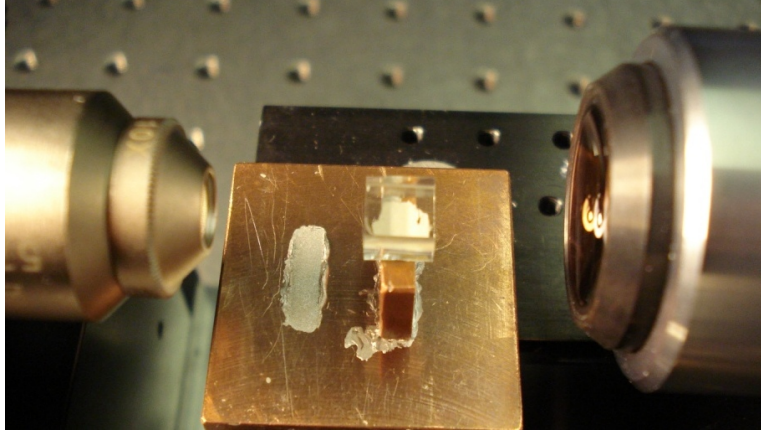

Fig 6.4 The plane-plane polished sample where the waveguides were inscribed via ULI technique. The left objective is inserting the 2 μm radiation during the waveguiding tests and the right one is imaging the structure.

The waveguides were pumped with a Ti:sapphire laser tuned to 791 nm and Figure 6.5 shows the measured waveguide laser output power as a function of pump power for the optimum waveguide. The emission was centered at 1.93μm and proved that lasing could be obtained from such a structure.
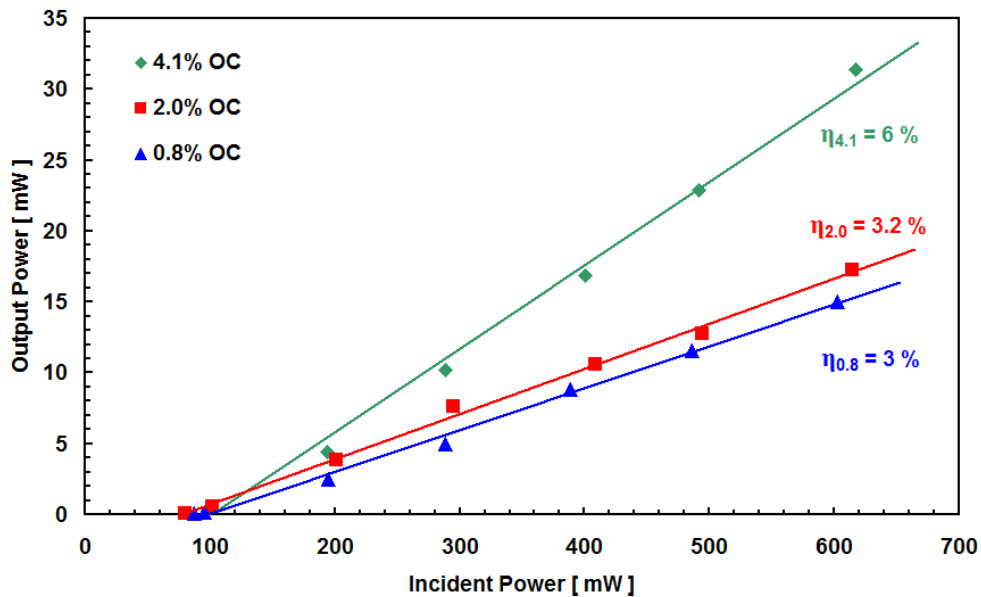

Fig 6.5 Waveguide laser output power at 1.93 μm as a function of the incident pump power for three different output couplers (OC).

Many other interesting ideas could derive from the research carried out during this project. Examples are also the generation of blue upconversion light in Tm^{3+} doped materials with 793 nm pumping[12] and the refinement and development of the glasses in the remarkable glass-ceramics[13]. Glass ceramics have very low thermal expansion coefficients and are extremely durable, the results that could be obtained in the area of femtosecond NIR solid state lasers with the techniques presented in this work have great potentialities and could generate extremely advantageous materials from the industrial point of view.

6.3 Conclusions

In conclusion then, the research carried out through the course of this thesis has shown that glasses belonging to Tellurite and Fluorogermanate ones are suitable for operation as bulk fs lasers in the 2 μm spectral region. Lasers setup in free space cavities were relatively big but the materials offer the necessary durability to be machined and to be used in more compact systems in the future. This work intended also to offer an economic and reliable solution to speed up the development cycle of active materials for laser industry. It was shown that the manufacturing and testing of the active samples could be carried out in time frames of few days and this is extremely advantageous compared to the few months of the crystalline counterparts. Further optimisation of the glasses into glass-ceramics could also allow for very hard materials with the potential of new customisable parameters such as thermal expansion coefficient and emission cross sections. The glasses tested in this work enable the development of a range of cheap and potentially compact lasers that will have the capacity to open up new applications and underpin future developments in non-linear optics.

6.4 References

[1]   X. Han, *et al.*, "*Continuous-wave laser operation of Tm and Ho co-doped NaY(WO4)(2) and NaLu(WO4)(2) crystals*", Optics Express, **18**, pp. 5413-5419, (2010).

[2]   A. A. Lagatsky, *et al.*, "*Optical spectroscopy and efficient continuous-wave operation near 2 μm for a Tm, Ho:KYW laser crystal*", Applied Physics B-Lasers and Optics, **97**, pp. 321-326, (2009).

[3]   F. Fusari, *et al.*, "*Tunable laser operation of a Tm^{3+}-doped tellurite glass laser near 2 μm pumped by a 1211 nm semiconductor disk laser*", Optical Materials, **32**, pp. 1007-1010, (2010).

[4]   A. A. Lagatsky, *et al.*, "*Passive mode locking of a Tm,Ho:KY(WO$_4$)($_2$) laser around 2 μm*", Optics Letters, **34**, pp. 2587-2589, (2009).

[5]   J. W. Tomm, *et al.*, "*Properties of As$^+$-implanted and annealed GaAs and InGaAs quantum wells: Structural and band-structure modifications*", Journal of Applied Physics, **95**, pp. 1122-1126, (2004).

[6]   U. Keller, *et al.*, "*Semiconductor saturable absorber mirrors (SESAM's) for femtosecond to nanosecond pulse generation in solid-state lasers*", IEEE Journal of Selected Topics in Quantum Electronics, **2**, pp. 435-453, (1996).

[7]   R. Lebullenger, *et al.*, "*Systematic substitutions in ZBLA and ZBLAN glasses*", Journal of Non-Crystalline Solids, **161**, pp. 217-221, (1993).

[8]   C. B. Schaffer, *et al.*, "*Micromachining bulk glass by use of femtosecond laser pulses with nanojoule energy*", Optics Letters, **26**, pp. 93-95, (2001).

[9]   F. M. Bain, *et al.*, "*Ultrafast laser inscribed Yb:KGd(WO$_4$)($_2$) and Yb:KY(WO$_4$)($_2$) channel waveguide lasers*", Optics Express, **17**, pp. 22417-22422, (2009).

[10]   G. Della Valle, *et al.*, "*1.5 μm single longitudinal mode waveguide laser fabricated by femtosecond laser writing*", Optics Express, **15**, pp. 3190-3194, (2007).

[11]   Y. Nasu, *et al.*, "*Low-loss waveguides written with a femtosecond laser for flexible interconnection in a planar light-wave circuit*", Optics Letters, **30**, pp. 723-725, (2005).

[12]   R. Paschotta, *et al.*, "*230 mW of blue light from a thulium-doped upconversion fiber laser*", IEEE Journal of Selected Topics in Quantum Electronics, **3**, pp. 1100-1102, (1997).

[13]   V. K. Tikhomirov, *et al.*, "*Gain cross-sections of transparent oxyfluoride glass-ceramics single-doped with Ho3+ (at 2.0 [mu]m) and with Tm3+ (at 1.8 [mu]m)*", Journal of Alloys and Compounds, **436**, pp. 216-220, (2007).